To the Graduate Council:

I am submitting herewith a thesis written by Allen Crabtree entitled "The Effect of Inlet Blockage Configuration on Flow Behavior in Rectangular Channels." I have examined the final copy of this thesis for form and content and recommend that it be accepted in partial fulfillment of the requirements for the degree of Master's of Science, with a major in Engineering Science.

Giuseppe Iannelli, Major Professor

We have read this thesis
and recommend its acceptance:

Accepted for the Council:

Associate Vice Chancellor and
Dean of The Graduate School

The Effect of Inlet Blockage Configuration on Flow Behavior in Rectangular Channels

A Thesis
Presented for the
Master of Science Degree
The University of Tennessee

Jerry Allen Crabtree
August 1997

Copyright © 1997 by Jerry Allen Crabtree.

All rights reserved.

DEDICATION

This thesis is dedicated to the memory of my father,

Cecil Allen Crabtree.

ACKNOWLEDGMENTS

I would like to express my appreciation to Dr. G. S. Iannelli, for the support, encouragement, and guidance he afforded me as my major professor. I would also like to thank Dr. A. J. Baker and Dr. A. E. Ruggles for their willingness to serve on the thesis committee. I am particularly grateful to Dr. G. L. Yoder who not only served on the thesis committee, but has also unknowingly served as my mentor for the past eight years at the Oak Ridge National Laboratory. I would also like to acknowledge Dr. David Sulfredge whose suggestions and comments were invaluable.

Lastly, my greatest debt is owed to the two women in my life: my mother whose love and encouragement distilled in me the confidence I needed to strive for my goals and my loving wife, Lisa, whose support and enduring patience has seen me through times of despair and without whom this accomplishment would be without meaning.

ABSTRACT

Experience with previous reactors has shown that inadequate cooling caused by partially blocked coolant channels can lead to fuel damage. This danger was of particular interest in the design of the Advanced Neutron Source (ANS) reactor. Preliminary designs addressed the issue of potential flow blockages by providing an unheated entrance length over which the flow disturbances would adequately recover. The Flow Blockage Test Facility (FBTF) was designed and built to conduct experiments in an environment closely matching the ANS channel geometry. In previous work the adequacy of this unheated entrance length was evaluated by testing various blockage widths at the edge and center of the channel entrance. This thesis is an extension of the initial study into the effect of blockage shape and position on downstream flow behavior. A series of non-standard blockage shapes and positions were designed, fabricated, and tested in the FBTF where flow field measurements were made using a Laser Doppler Velocimeter. Comparisons were made to corresponding standard square blockages to determine what effect, if any, a particular shape or position would have on downstream fluid flow. Using the computational fluid dynamics code *Fluent*, one blockage configuration was modeled and the use of various turbulence models and near-wall treatments evaluated.

TABLE OF CONTENTS

1. INTRODUCTION 1

2. REVIEW OF LITERATURE 3

3. EXPERIMENTAL PROCEDURE 6
   - 3.1 EXPERIMENTAL FACILITY 6
   - 3.2 LASER DOPPLER VELOCIMETRY 10

4. FLOW FIELD MEASUREMENTS 13
   - 4.1 STANDARD SQUARE BLOCKAGES 15
   - 4.2 SHAPE DEPENDENCE 26
   - 4.3 POSITION DEPENDENCE 43

5. INTERPRETATIONS AND CORRELATIONS 57
   - 5.1 STANDARD CORRELATIONS 57
   - 5.2 SHAPE ADJUSTMENT 63
   - 5.3 REYNOLDS NUMBER ADJUSTMENT 66

6. CFD MODELING ISSUES 73
   - 6.1 WALL FUNCTIONS 76
   - 6.2 BOUNDARY LAYER RESOLUTION 86
   - 6.3 LDV COMPARISONS 92

7. CONCLUSIONS 101

REFERENCES 103

VITA 106

LIST OF FIGURES

Figure		Page
1	Flow Blockage Test Facility schematic	6
2	Inlet plenum and blockage assembly	8
3	Inlet blockage configuration	9
4	Standard blockage dimensions	15
5	Curve fit of minimum axial velocity as a function of downstream distance for use in predicting reattachment length	16
6	Axial velocity profiles downstream of a 15% inlet blockage	18
7	Axial velocity profiles downstream of a 25% inlet blockage	19
8	Axial velocity profiles downstream of a 30% inlet blockage	20
9	Axial velocity profiles downstream of a 35% inlet blockage	21
10	Axial velocity profiles downstream of a 40% inlet blockage	22
11	Spanwise velocity profiles downstream of a 30% inlet blockage	23
12	Axial turbulent kinetic energy downstream of a 30% inlet blockage	24
13	Spanwise turbulent kinetic energy downstream of a 30% inlet blockage	25
14	Recovery characteristics for standard blockages	26
15	Alternate inlet blockage shapes and dimensions	27
16	Axial velocity profiles downstream of a 40% smooth inlet blockage	28
17	Comparison of axial velocity profiles 10.8 d_h downstream of 40% smooth and 40 and 30% standard center inlet blockages	29
18	Axial velocity profiles downstream of a 25% converging triangular inlet blockage	30
19	Axial velocity profiles downstream of a 25% diverging triangular inlet blockage	31

20 Comparison of axial velocity profiles 10.8 d_h downstream of 25% standard, 25% diverging, and 25% converging center inlet blockages 33
21 Comparison of spanwise velocity profiles 10.8 d_h downstream of 25% standard and 25% converging center inlet blockages 34
22 Axial velocity profiles downstream of a 20/40% diverging trapezoidal inlet blockage 36
23 Axial velocity profiles downstream of a 40/20% converging trapezoidal inlet blockage 37
24 Comparison of axial velocity profiles 10.8 d_h downstream of 40% standard, 20/40% diverging, and 40/20% converging center inlet blockages 38
25 Axial velocity profiles downstream of a 30% parallelogram inlet blockage 40
26 Comparison of axial velocity profiles 10.8 d_h downstream of 30% standard, 30% parallelogram, and 40% standard center inlet blockages 41
27 Off-center 15% blockage positions 44
28 Dual 15% center blockage positions 44
29 Axial velocity profiles downstream of a 15% square inlet blockage positioned 35% off center 45
30 Axial velocity profiles downstream of a 15% square inlet blockage positioned 65% off center 46
31 Axial velocity profiles downstream of a 15% square inlet blockage positioned 82% off center 47
32 Axial velocity profiles downstream of a 15% square inlet blockage positioned at the edge 48
33 Comparison of axial velocity profiles 10.8 d_h downstream of 15% blockages positioned 0, 35, 65, and 82% off center 51

34 Axial velocity profiles downstream of dual 15% blockages positioned with a 5% separation gap 53
35 Axial velocity profiles downstream of dual 15% blockages positioned with a 20% separation gap 54
36 Comparison of axial velocity profiles 61.3 d_h downstream of 15-5-15 and 30, 35, and 40% standard blockages 56
37 Gapwise non-dimensionalized reattachment length dependence on blockage size 58
38 Blockage width non-dimensionalized reattachment length dependence on blockage size 58
39 Exponential curve-fit of gapwise non-dimensionalized reattachment length dependence on average mid-gap velocity 60
40 Unblocked velocity non-dimensionalized average velocity dependence on blockage size 61
41 Unblocked velocity non-dimensionalized average velocity dependence on effective hydraulic diameter 61
42 Curve-fit comparison for unblocked velocity non-dimensionalized average velocity dependence on effective hydraulic diameter 63
43 Curve-fits for the adjustment/angle slope as a function of blockage size 65
44 Unblocked velocity non-dimensionalized average velocity dependence on effective hydraulic diameter and Reynolds number 67
45 Required correlation coefficient to account for average mid-gap velocity dependence upon Reynolds number 68
46 Gapwise non-dimensionalized reattachment length dependence on average mid-gap velocity and Reynolds number 70
47 Required correlation coefficient to account for reattachment length dependence upon Reynolds number 71
48 CFD model geometry at channel inlet 75

49 Inlet plenum and channel mesh 76
50 Contours of velocity magnitude for standard k-ε case 77
51 Path lines colored by velocity magnitude for standard k-ε case 78
52 Contours of static pressure for standard k-ε case 78
53 Axial pressure distribution along the centerline on the plane of symmetry for standard k-ε case 79
54 Contours of turbulent kinetic energy for standard k-ε case 80
55 Contours of surface y^+ for standard k-ε case 81
56 Path lines colored by velocity magnitude for RSM case 84
57 Contours of VV Reynolds stress for RSM case 84
58 Contours of WW Reynolds stress for RSM case 85
59 Contours of UU Reynolds stress for RSM case 85
60 Inlet plenum and shortened channel mesh 86
61 Contours of turbulent kinetic energy for 9 gap cells 87
62 Contours of turbulent Reynolds number for 9 gap cells 88
63 Contours of turbulent kinetic energy for 14 gap cells 89
64 Contours of turbulent Reynolds number for 14 gap cells 89
65 Contours of turbulent kinetic energy for 17 gap cells 91
66 Contours of turbulent Reynolds number for 17 gap cells 91
67 Comparison of measured axial velocity profiles to CFD calculations using the RSM turbulence model 94
68 Comparison of measured spanwise velocity profiles to CFD calculations using the RSM turbulence model 95
69 Comparison of measured axial velocity profiles to CFD calculations using the k-ε turbulence model with boundary layer resolution 96

70 Comparison of measured spanwise velocity profiles to CFD calculations using the k-ε turbulence model with boundary layer resolution 97
71 Comparison of measured axial velocity profiles to CFD calculations using the RNG k-ε turbulence model with boundary layer resolution 98
72 Comparison of measured spanwise velocity profiles to CFD calculations using the RNG k-ε turbulence model with boundary layer resolution 99

NOMENCLATURE

d_h	hydraulic diameter
$d_{h(nom)}$	hydraulic diameter of an unblocked channel
gap	channel gap, 1.27 mm
k	turbulent kinetic energy
l_r	reattachment length
Re	Reynolds number
Re_{nom}	unblocked Reynolds number
span	channel span, 84 mm
t_b	blockage thickness
u	LDV measured axial component of velocity
$\bar{u}$	average mid-gap velocity across the channel span
$\overline{u_c}$	average mid-gap velocity across the channel span for a converging non-standard blockage
$\overline{u_d}$	average mid-gap velocity across the channel span for a diverging non-standard blockage
$\overline{u_{std}}$	average mid-gap velocity across the channel span for a standard blockage
U_{max}	maximum axial velocity at the mid-gap for an unblocked case
u_i	velocity vector
$\bar{u}_i$	time averaged velocity vector

u_i'	velocity perturbation
v	LDV measured spanwise component of velocity
w_b	blockage width
x	axial position
y	span position
y^+	position relative to boundary layer thickness

1. INTRODUCTION

Both research and commercial reactor cores have a large number of parallel channels that are necessary to remove the heat produced by the fuel rods, pins, or plates of which the cooling channels are comprised. If a single channel were to become partially blocked, its cooling capacity would be greatly reduced thus allowing the fuel plate to overheat locally. Experience with previous reactors has shown that inadequate cooling caused by partially blocked coolant channels can lead to fuel damage. Such occurrences have been documented for the Hanford KW Reactor in 1955, the Sodium Reactor Experiment in 1959, the Oak Ridge Research Reactor in 1963, and the Fermi Reactor in 1966 (Bertini, 1980). Other occurrences include the Engineering Test Reactor in 1961 and the Material Testing Reactor in 1962, both at the National Reactor Testing Station in Idaho (Thompson and Beckenley, 1964). The danger in these configurations lies in the potential for one or several channels to become partially blocked and escape detection by temperature and flow meters. The first indication of a problem is often too late and is the result of contamination of the cooling water caused by a breach in the fuel plate cladding.

This danger was of particular interest in the design of the Advanced Neutron Source (ANS) reactor. The ANS reactor was to be the world's most powerful research reactor. Its state-of-the-art design would require 25 m/s flow

through a large number of parallel cooling channels to remove the 6 MW/m^2 average heat flux across each fuel plate. Each channel was to have a gap of 1.27 mm, span of 84 mm, and a length of 500 mm resulting in a high aspect ratio (span/gap) of 66.1. Preliminary ANS designs addressed the issue of potential flow blockages by providing an unheated entrance length over which the flow disturbance would adequately recover. The Flow Blockage Test Facility (FBTF) was designed and built to conduct experiments in an environment closely matching the ANS channel geometry. The initial scope of previous work was to evaluate the adequacy of this unheated entrance length through a review of the available data, CFD modeling of the ANS fuel plate geometry, and experimental efforts to simulate ANS conditions (Stovall et al., 1995). This work involved the testing of various blockage widths at the edge and center of the channel entrance.

This thesis is an extension of the initial study into the effect of blockage shape and position on downstream flow behavior. A series of non-standard blockage shapes and positions were designed, fabricated, and tested in the FBTF where flow field measurements were made using a Laser Doppler Velocimeter. Comparisons were made to corresponding standard square blockages to determined what effect, if any, a particular shape or position would have on downstream fluid flow. Using the computational fluid dynamics code *Fluent*, one blockage configuration was modeled and the use of various turbulence models and near-wall treatments evaluated.

2. REVIEW OF LITERATURE

An extensive literature search uncovered several publications describing the fluid flow behavior downstream of a blockage. Of these publications, few were actually applicable to high Reynolds number (≈59,000) flow through a narrow (aspect ratio = 66.1) rectangular channel, and even fewer addressed blockages which spanned the entire gap. Kirsch and Schleisiek (1973), for example, made flow and temperature measurements around coolant blockages in a fast sodium-cooled reactor fuel assembly which, unlike the ANSR, consisted of an array of fuel pins. Similar experiments were performed at Oak Ridge National Laboratory in which heat transfer coefficients were measured downstream of partial blockages in a 19-rod sodium-cooled electrically heated rod bundle (Fontana et al., 1973). Koram and Sparrow (1978) performed a number of heat transfer and fluid flow experiments to determine mass transfer coefficients and pressure drops resulting from segmental (edge) blockages in fully turbulent flows. This work was later expanded in scope to include slat (center) blockages as well (Sparrow et al., 1980). Although these experiments were performed for turbulent flows with Reynolds numbers ranging from 10,000 to 60,000, the measurements were made in a circular tube as opposed to a rectangular channel.

Due to the increasing amount of work being performed in the area of electronic component cooling, there were a number of publications discussing

the heat transfer and fluid flow around surface-mounted obstacles. Unfortunately most of these publications were limited to the investigation of three-dimensional blockage arrangements. In three-dimensional blockage arrangements, the blockage does not span across the entire gap thus is exposed to flow not only along the sides but also above. In two-dimensional blockage arrangements, however, the blockage does span across the entire gap thus the flow is constrained along the sides. Experiments which involved high Reynolds number flows and spanwise variation, however, resulted in some limited two-dimensional observations (Martinuzzi and Tropea, 1993). Although Roeller and Webb (1991) performed similar experiments using two-dimensional protrusions while varying the gap, their study was limited to $1{,}500 \leq Re \leq 10{,}000$.

Of the publications found to be most closely relevant to the current work, there were three publications by Sparrow with various co-authors, on the subject of turbulent duct flow with inlet blockages. In these experiments, mass transfer was measured using a naphthalene sublimation technique with air as the working fluid. Unfortunately, these experiments spanned Reynolds numbers of only 5,000 to 30,000. Sparrow and Wachtler (1978) studied the effects on heat and mass transfer downstream of an edge blockage in the first series of experiments. In a later publication, this work was expanded to include center blockages as well as some comparisons to the earlier edge-positioned blockage data (Sparrow et al., 1981). Although both series of experiments were performed using square ducts (aspect ratio = 1), a later work documented

experiments performed using rectangular ducts with a "high" aspect ratio of 18.3 (Cur, 1982, and Sparrow and Cur, 1983). A comparatively recent publication investigated fluid flow behavior in rectangular ducts downstream of two-dimensional blockages in both the laminar and turbulent regions (Popiel and Turner, 1991). The working fluid in these experiments was water and the Reynolds numbers ranged from 377 to 36,900. The aspect ratio in these experiments, however, was even lower than in the Sparrow studies at 3.4. In short, there were no publications found in which inlet blockages were investigated for turbulent flows with Re $\approx$ 59,000 in narrow rectangular channels with aspect ratios near 66.1.

3. EXPERIMENTAL PROCEDURES

3.1 EXPERIMENTAL FACILITY

The Flow Blockage Test Facility (FBTF) at the Oak Ridge National Laboratory (ORNL) was designed to simulate the hydraulic conditions found in a prototypical ANSR cooling channel. The experimental test loop shown in Fig. 1, consists of a pump capable of providing 25 m/s flow through an unblocked channel, a test section simulating the full gap, span, and length of an ANSR cooling channel, and a heat exchanger to remove any heat added to the water by the pump. A laser Doppler velocimeter (LDV) was used in this work to

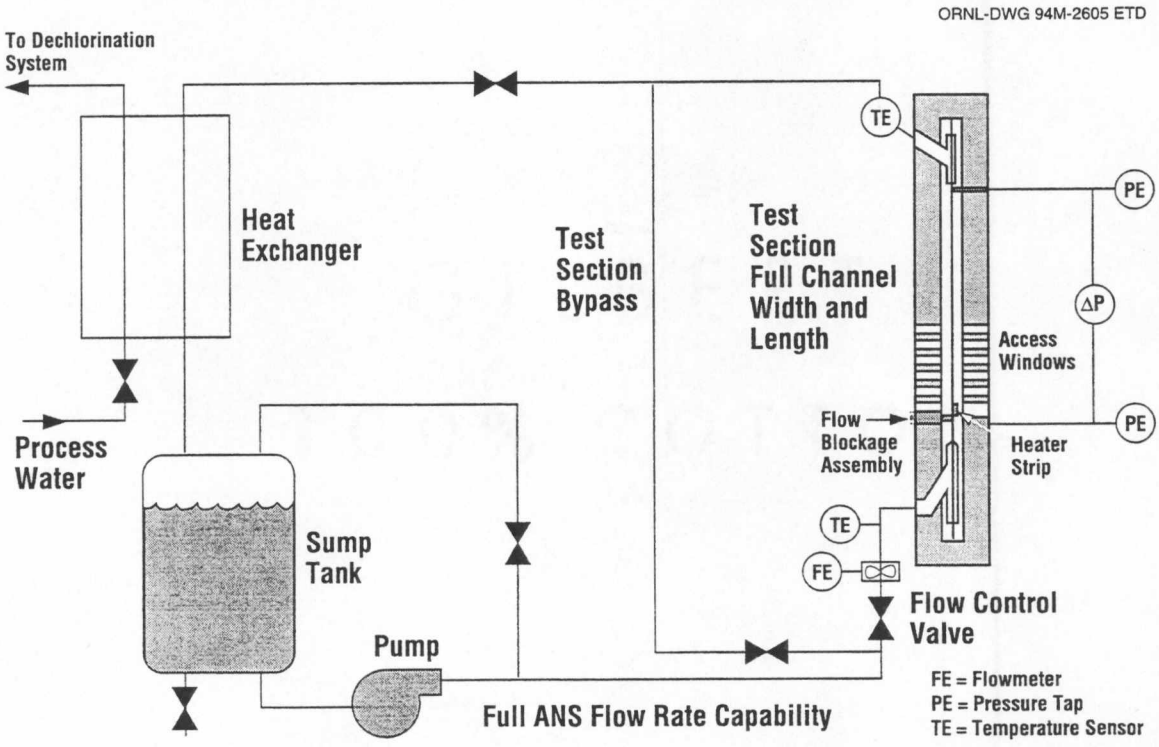


Figure 1. Flow Blockage Test Facility schematic

measure the flow field downstream of the inlet blockages. Due to this measurement technique, it was necessary to have transparent channel walls through which the laser beams could cross. The channel walls are thus constructed of 50 mm thick machined Lexan and a steel shim is "sandwiched" between the two Lexan pieces to ensure the correct gap dimension of 1.27 mm. In order to maintain the channel dimensions under pressure, the Lexan pieces with the shim installed are bolted together at the periphery and placed into a thick stainless steel casing with six access windows. The loop is instrumented with one differential and two static pressure transducers to quantify the pressure drop through the channel with instrument accuracies of ±1%. A flow meter provides a measure of the average volumetric flow rate to the test section with an instrument accuracy of ±1% while two temperature sensors monitor the water temperature through the test section with instrument accuracies of ±1.2°C.

A side view of the inlet plenum and blockage assembly can be found in Fig 2. Water enters near the bottom of the test section in the center (spanwise) of an inlet plenum at an angle of 30°. The inlet plenum is 180 mm long, 84 mm wide, and has a gap of 25 mm. The top of the inlet plenum narrows at a 45° angle so that the gap is reduced from 25 mm to 2.54 mm. 35 mm downstream from the inlet, the channel entrance is defined by an abrupt 90° symmetric step down from a gap of 2.54 mm to 1.27 mm. Numerical models in previous work indicate that this flow conditioning produces uniform flow at the channel inlet in

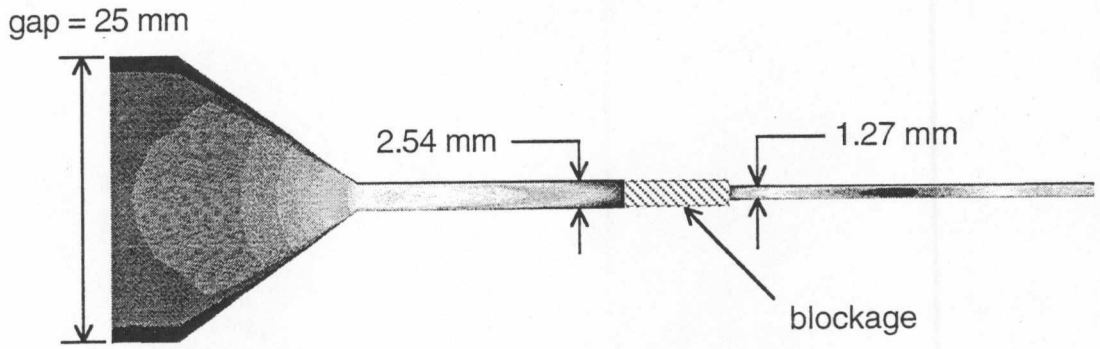


Figure 2. Inlet plenum and blockage assembly

the absence of any blockage (Stovall et al., 1995). Approximately 200 hydraulic diameters downstream, the exit plenum is marked by an abrupt expansion from the 1.27 mm gap to 25 mm.

The inlet flow blockage assembly (Fig. 3) was designed so that various blockage widths (w_b) and positions could be easily tested. The thickness of the blockage (t_b) in the flow direction, however, is fixed at 10 mm. As the FBTF was designed to examine the effect of potential inlet blockages, the blockage assembly is positioned so that a tight fit exists between the blockage element and the 0.635 mm lip between the inlet region and the channel. For purposes of this work, several additional blockages were designed to investigate the effect of blockage shape and position on the fluid dynamics downstream.

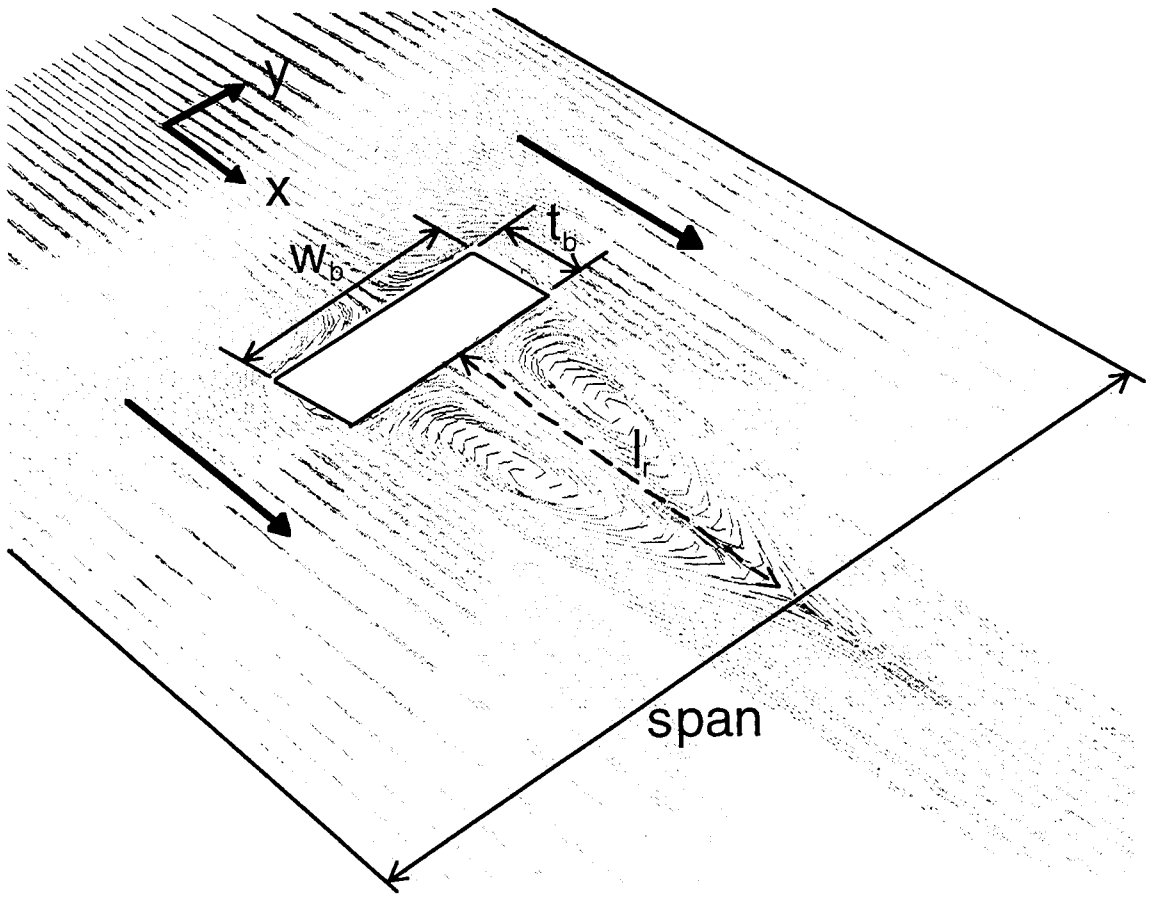


Figure 3. Inlet blockage configuration

For each blockage, a general procedure was followed to ensure consistency for future analysis and comparisons. Once the blockage was securely placed in the assembly, the pump was started. The flow control valve and the test section bypass were adjusted so as to impose a 0.7 MPa pressure drop across the channel regardless of the blockage that was in place, thus appropriately simulating the conditions expected in an actual reactor with a nearly infinite bypass ratio. Using the traversing system, the LDV control volume was then placed in the middle of the channel gap. Data was then taken

along the span for the first five measurement windows. To ensure that a good comparison could be made between flows resulting from different blockage configurations, physical property variations were minimized by adjusting the heat exchanger so as to maintain a water temperature of 31°C.

3.2 LASER DOPPLER VELOCIMETRY

Laser Doppler velocimetry (LDV) technology utilizes intersecting laser beams and optical data processing equipment to measure the motion of minute particles in flow systems. A pair of beams are required for each component of velocity to be measured. Optical equipment is used to impose a fringe pattern at the intersection of the two beams. This pattern has a known fringe spacing and as a particle passes through the measurement volume, the receiving fiber measures the frequency of the resulting pulses of light. The next problem arises in discriminating between the direction (up or down) of the particle as the frequency response would be the same in each case. This issue is addressed by imposing a known frequency shift on the fringe pattern in the measurement volume. Ideally, one would apply this frequency shift in the direction opposite of the main flow so as to capture any flow reversals in the flow field. The post-processing software accounts for this frequency shift and corrects the velocity measurement. When utilizing frequency shifting, even stationary particles in stagnation regions can be detected as they would appear to have a frequency response equal to that of the frequency shift.

LDV's not only measure the mean directional components of velocity, but as it is a statistical method of measurement it provides such useful information as standard deviation, turbulence, skewness, flatness, vector magnitude, and directional cosines. For a multiple-component LDV system, velocity projection, angle mean, Reynolds stress, and correlation coefficient are also calculated by the data processing software.

The LDV system used in the FBTF was manufactured by TSI, Inc. and a version of their *FIND* software was used in the data processing of the LDV measurements (TSI, Inc., 1993). Two processors were used to provide velocity measurements in the axial and spanwise directions. The LDV probe and fiber optics were mounted on a highly accurate (0.01 mm) three dimensional traversing system. The lenses and other optical components were selected so as to ensure that the resulting measurement volume would indeed fit into the gap of the channel. The measurement volume width in the gap direction was 0.27 mm and was positioned in the center of the 1.27 mm gap for the experimental velocity measurements. The center was located by adjusting the traversing system until the measurement volume included the channel wall, which was indicated by a sharp spike in the zero velocity measurements and by the decreased data collection rate. After the position of both bounding walls was identified in this manner, the traversing system was adjusted to place the measurement volume at the midpoint.

Approximately 42 velocity measurements were made across the 84 mm span for each of the first five observation windows. Each data point is the result of statistical operations upon a total of 1024 data points taken at each position. In a detailed error analysis, the total uncertainty was calculated to be -2% to +3% for highly turbulent separated flow with a well-designed LDV system incorporating frequency shift (Patrick, 1985).

4. FLOW FIELD MEASUREMENTS

Flow field measurements were made using a two-component LDV system for a series of standard and non-standard blockage shapes and positions. The two components of velocity measured were oriented in the axial and span directions. Measurements were made at 11, 23, 36, 49, and 61 hydraulic diameters downstream of the flow blockage. At each window, data were taken across the span at an approximate data density of 1 point for every 2 mm. It is important to note that for all of the blockages tested, the average flow rate through the test section was adjusted so as to assure that the total pressure drop was maintained at 0.7 MPa. This was important so as to duplicate adequately the conditions expected in a reactor core with a nearly infinite bypass ratio.

Since the LDV measurement volume was positioned in the center of the channel gap, the velocity measurements were non-dimensionalized by the average mid-gap velocity for an unblocked channel at 0.7 MPa pressure drop (18.6 m/s). Since the unblocked channel velocity is known for nominal conditions, it was considered an appropriate non-dimensionalization parameter. The resulting non-dimensionalized velocity provides a measure of how the resulting flow compares to an unblocked case. The spanwise positions and axial positions were non-dimensionalized by the 84 mm channel span and the 2.5 mm hydraulic diameter respectively. As a secondary check on the

velocity measurement, an average mid-gap velocity across the channel span was calculated, using Simpson's rule, at a position 61 hydraulic diameters downstream (Burden and Faires, 1993). In order to appropriately compare this average mid-gap velocity to the average velocity reported by the flow meter, two corrections were applied. Initially the average mid-gap velocity was multiplied by 1.012. This correction factor was determined by integrating the 1/10 power law approximation for a fully developed turbulent velocity profile across the width of the measurement volume from 0.5 to 0.635 mm and solving for the true mid-gap velocity. This mid-gap velocity was then further corrected by multiplying by 0.909. This correction factor reflects the average-to-peak ratio determined by integrating the same approximation throughout the entire boundary layer. This integration was also performed for application of the 1/7 power profile and resulted in corresponding correction factors of 1.016 and 0.875. CFD analysis, however, corroborate the 0.909 correction factor by numerically integrating the resulting velocity profile.

Initially this corrected average velocity did not compare well to the actual flow meter readings. The bulk fluid velocity as reported by the flow meter was consistently 10 to 11% higher than the corrected average LDV velocity. To verify its accuracy, the flow meter was retested and found to be well within calibration. Since the flow meter actually measures the volumetric rate of the flow, the reported bulk fluid velocity is based upon ideal channel dimensions. In an attempt to verify the actual channel dimensions, various combinations of

shim stock were then inserted into the Lexan channel to gauge the gap. The gap was found to be as high as 1.37 mm, which would result in an overestimation of the bulk fluid velocity by approximately 8%. Once the flow meter fluid velocity readings were adjusted to correct for actual channel dimensions, the two measures of average velocity agreed to within 2 to 3%.

4.1 STANDARD BLOCKAGES

In order to determine the effects of blockage shape on the downstream fluid flow behavior, a series of standard square-edge blockages were tested and analyzed for future comparison. Dimensions for these blockages can be found in Fig. 4. For each test, the blockage was positioned in the center of the

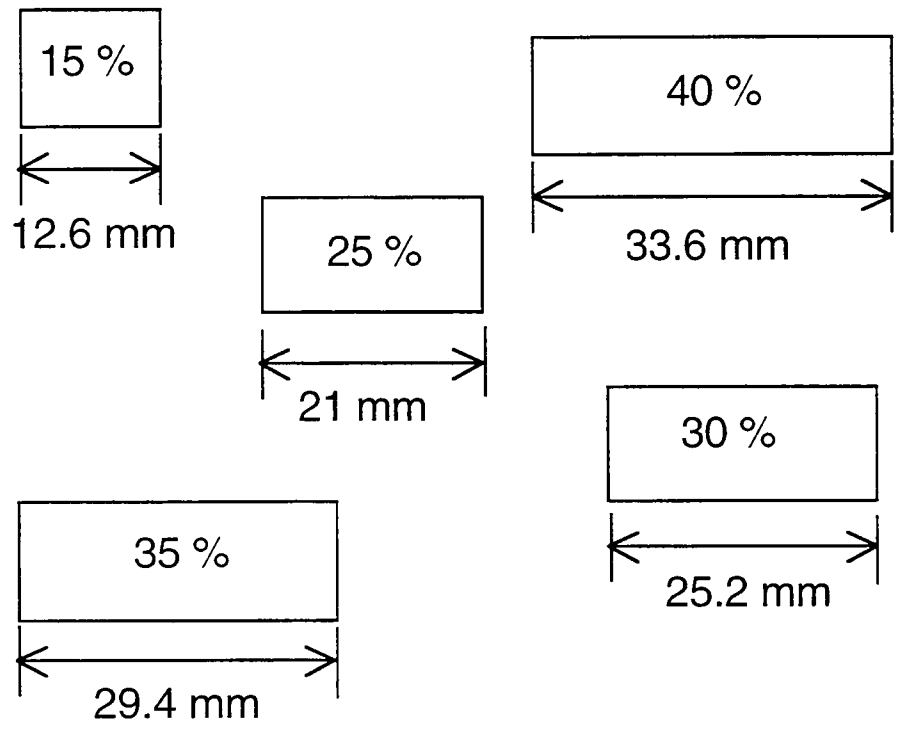


Figure 4. Standard blockage dimensions

channel span. The standard blockages tested were 15, 25, 30, 35, and 40% (w_b/span). For each blockage configuration, the data were analyzed using the *FIND* software and was converted into an Excel spreadsheet. The minimum velocity observed at each axial station was noted and plotted as a function of the downstream distance. This provided a visual representation of the flow recovery characteristics for each blockage tested. For blockage configurations in which negative velocity measurements were observed (>15%), these velocities were curve fit as a function of downstream distance. As can be seen in Fig. 5, a reattachment length can be approximated from the curve fit by

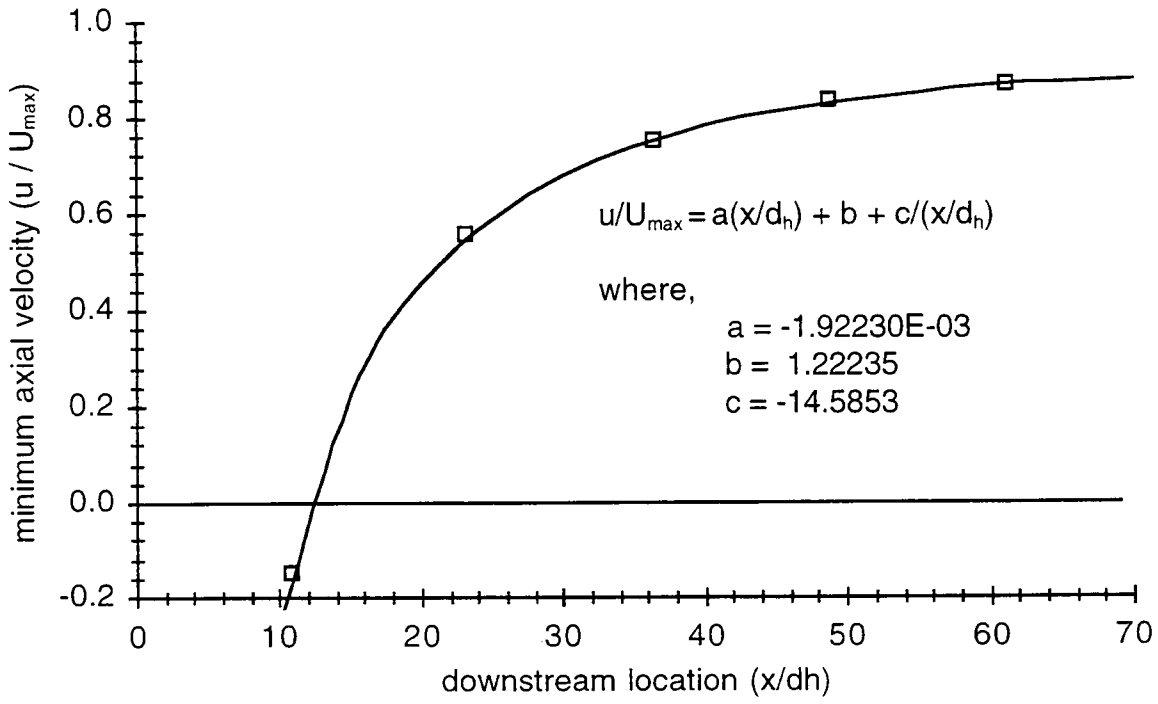


Figure 5. Curve fit of minimum axial velocity as a function of downstream distance for use in predicting reattachment length

setting the equation to 0 and solving for x/d_h. The reattachment length marks the transition to fully forward flow. A reattachment length can be also approximated for the 15% blockage, but the confidence in such an approximation is low due to the necessity to extrapolate as opposed to interpolate.

Additional variables for comparison are the overall velocity defect (u_{od}) and the local velocity defect (u_{ld}). The overall velocity defect (Eq. 1) is a measure of how the average mid-gap velocity across the channel span compares with the maximum velocity observed at the mid-gap for an unblocked case.

$$u_{od} = \frac{\bar{u} - U_{max}}{U_{max}} \qquad (1)$$

where,

$\bar{u}$ = average mid-gap velocity across the channel span
U_{max} = maximum axial velocity at the mid-gap for an unblocked case

The local velocity defect (Eq. 2) is a measure of how the mid-gap velocity at a given location compares with the maximum velocity observed at the mid-gap for an unblocked case.

$$u_{ld} = \frac{u - U_{max}}{U_{max}} \qquad (2)$$

where,

u = LDV measured axial component of velocity
U_{max} = maximum axial velocity at the mid-gap for an unblocked case

As can be seen in Fig. 6, reattachment for a 15% center inlet blockage occurs somewhere before the first measurement window at 10.8 d_h. The resulting average mid-gap velocity of 18.3 m/s reflects only a 1.6% overall velocity defect. The local minimum velocity of 6.5 m/s, however, 10.8 d_h directly downstream of the blockage corresponds to a 65% local velocity defect. The mid-span velocity recovers to 94% by the fifth measurement window at 61.3 d_h.

Reattachment for a 25% center blockage occurs between 10.8 and 23.3 d_h, as shown in Fig. 7. From the curve fit of the minimum velocities, the reattachment length was approximated at 11.5 d_h (28.8 mm) or 1.37 blockage widths downstream. The resulting average mid-gap velocity of 17.9 m/s reflects

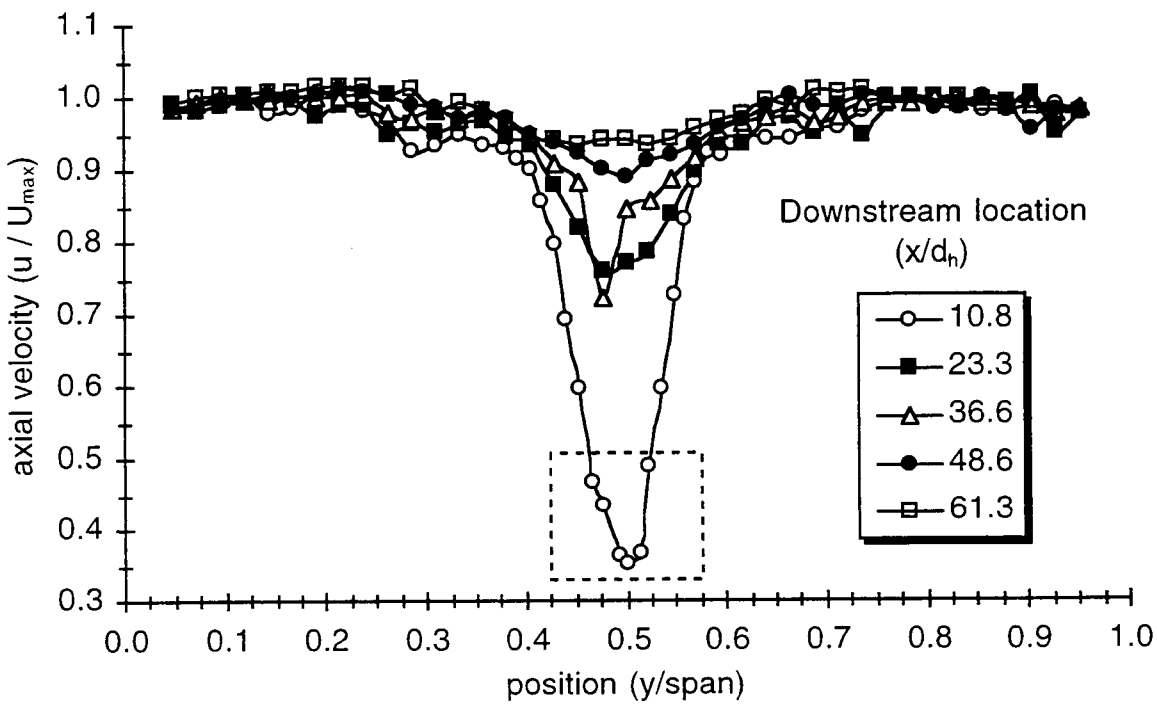


Figure 6. Axial velocity profiles downstream of a 15% inlet blockage

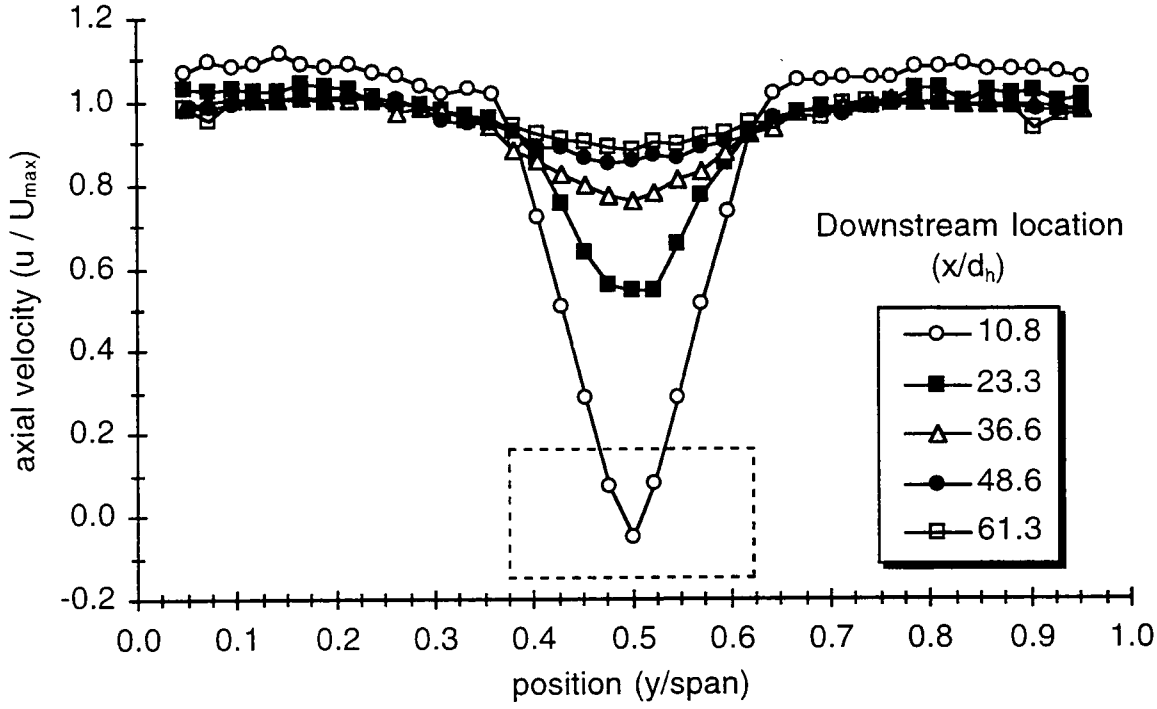


Figure 7. Axial velocity profiles downstream of a 25% inlet blockage

a 3.7% overall velocity defect. The negative velocity magnitude observed in the first measurement window was only 5.4% of the unblocked velocity. By the fifth measurement window at 61.3 d_h, the mid-span velocity has recovered to 88% of the unblocked velocity.

As can be seen in Fig. 8, reattachment for a 30% center inlet blockage occurs between 10.8 and 23.3 d_h. From the curve fit of the minimum velocities, the reattachment length was approximated at 11.9 d_h (29.84 mm) or 1.18 blockage widths downstream. The resulting average mid-gap velocity of 17.7 m/s reflects a 4.8% overall velocity defect. The negative velocity magnitude observed in the first measurement window was only 6.2 % of the unblocked

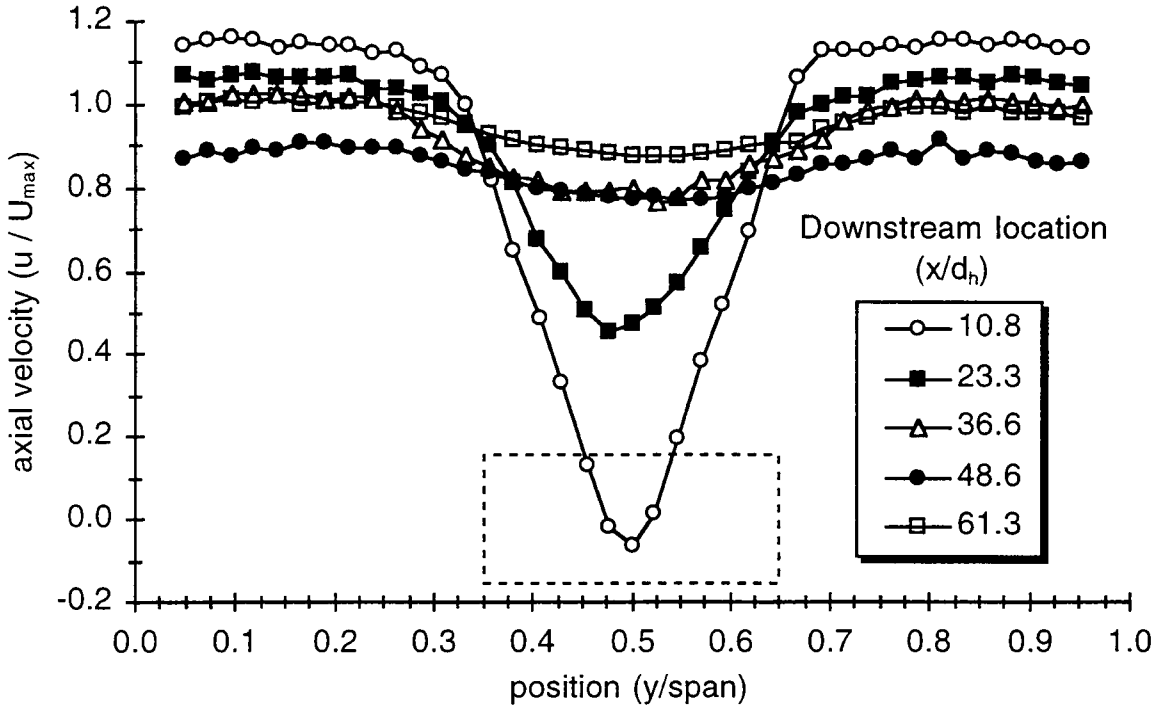


Figure 8. Axial velocity profiles downstream of a 30% inlet blockage

velocity. By the fifth measurement window at 61.3 d_h, the mid-span velocity has recovered to 87% of the unblocked velocity.

Reattachment for a 35% center blockage occurs between 10.8 and 23.3 d_h, as shown in Fig. 9. From the curve fit of the minimum velocities, the reattachment length was approximated at 12.5 d_h (31.3 mm) or 1.06 blockage widths downstream. The resulting average mid-gap velocity of 17.4 m/s reflects a 6.4% overall velocity defect. The negative velocity magnitude observed in the first measurement window was 15% of the unblocked velocity. By the fifth measurement window at 61.3 d_h, the mid-span velocity has recovered to 86% of the unblocked velocity.

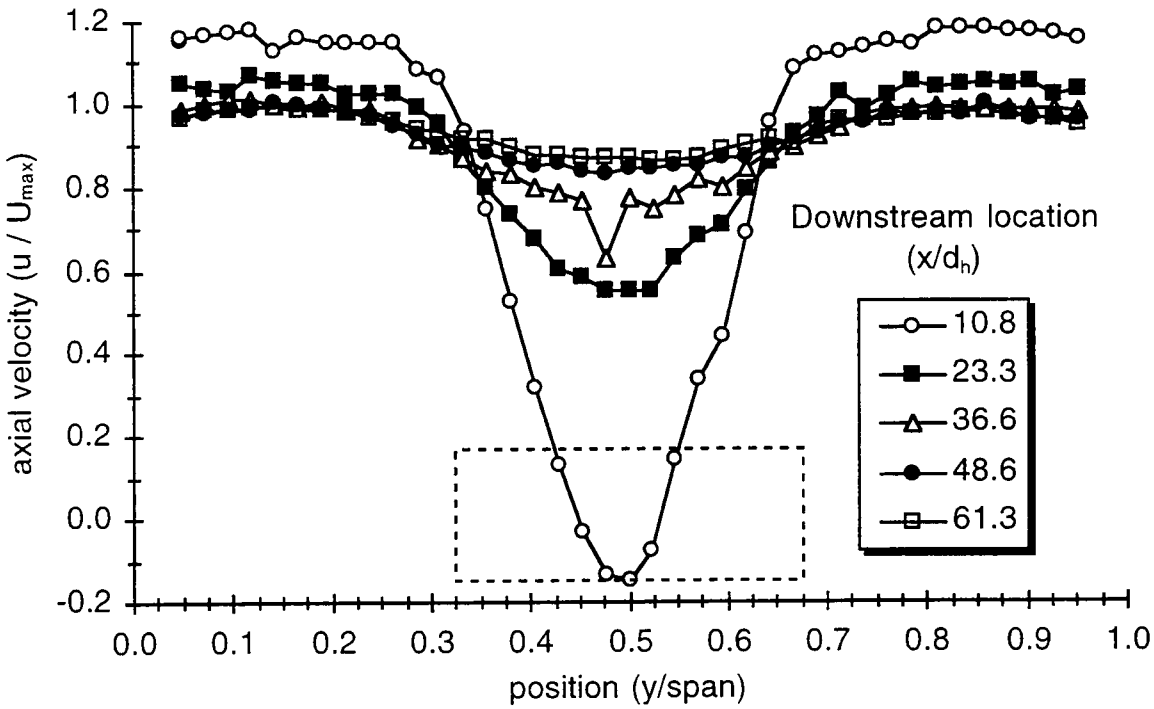


Figure 9. Axial velocity profiles downstream of a 35% inlet blockage

As can be seen in Fig. 10, reattachment for a 40% center inlet blockage occurs between 10.8 and 23.3 d_h. From the curve fit of the minimum velocities, the reattachment length was approximated at 12.7 d_h (31.92 mm) or 0.95 blockage widths downstream. The resulting average mid-gap velocity of 16.8 m/s reflects a 9.7% overall velocity defect. The negative velocity magnitude observed in the first measurement window was 21 % of the unblocked velocity. By the fifth measurement window at 61.3 d_h, the mid-span velocity has recovered to 83% of the unblocked velocity.

Although the majority of plots shown here concentrate on axial velocity profiles, spanwise velocities were also measured. Spanwise velocity profiles

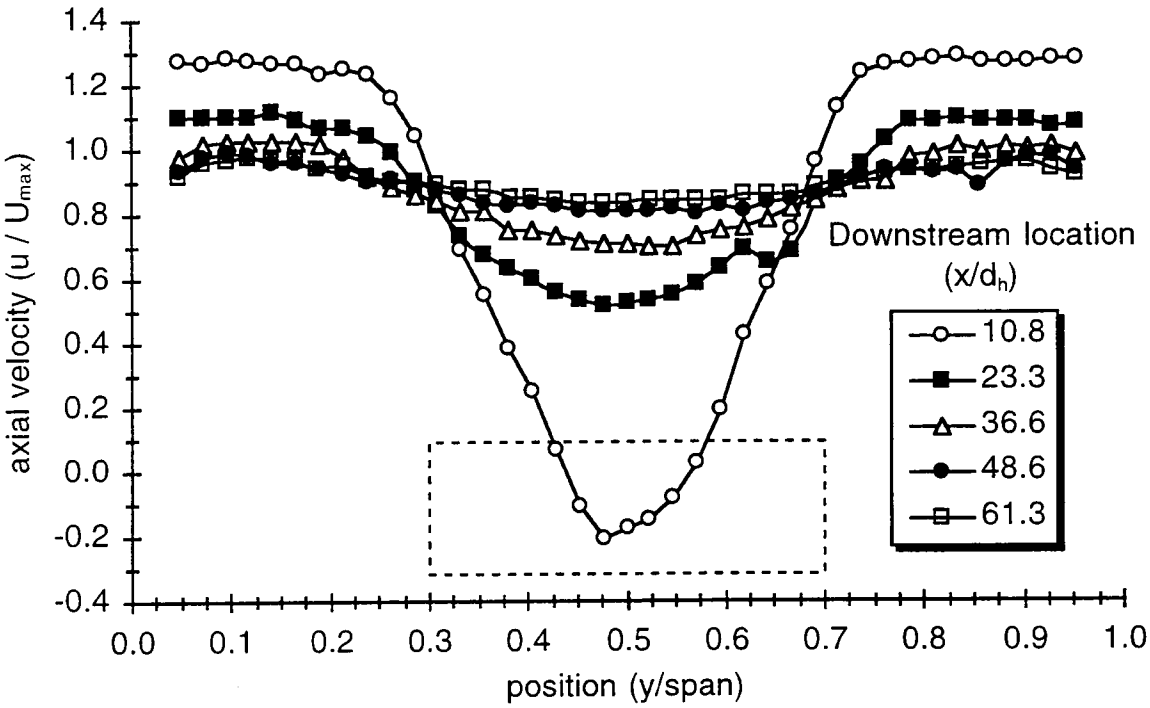


Figure 10. Axial velocity profiles downstream of a 40% inlet blockage

often help one to understand better the flow dynamics occurring downstream of an inlet blockage. In Fig. 11, the positive velocities reflect flow to the right while negative velocities reflect flow to the left. With this sign convention in mind, the spanwise velocity vectors are consistent with flow recovery in the low-pressure wake downstream of the blockage.

Another important flow parameter measured during the experiment was axial and spanwise turbulence. Both the LDV data analysis and the *Fluent* CFD code are based on the turbulent velocity model shown in Eq. (3).

$$u_i = \bar{u}_i + u_i' \tag{3}$$

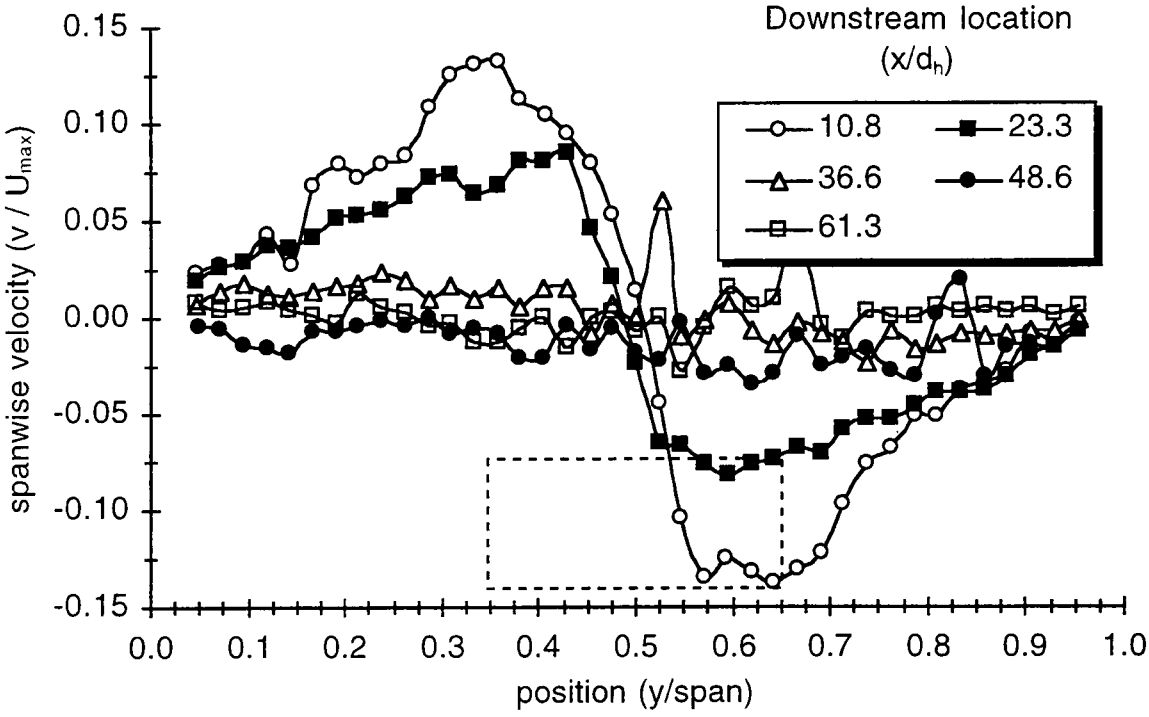


Figure 11. Spanwise velocity profiles downstream of a 30% inlet blockage

where,

u_i = velocity vector at a point

$\bar{u}_i$ = time-averaged velocity

u_i' = fluctuating velocity component (velocity perturbation)

The turbulent kinetic energy is defined from the LDV data by using the absolute value of the flow perturbation for each data point to calculate the average perturbation magnitude. This value was then used as shown in Eq. (4) to determine the turbulent kinetic energy for each velocity component.

$$k_i = \frac{1}{2}\overline{u_i'^2} \qquad (4)$$

where,

k_i = turbulent kinetic energy in the i direction

u_i' = fluctuating velocity component (velocity perturbation)

In Fig. 12 one can see a typical axial turbulent kinetic energy profile resulting from a center blockage at the inlet. A fairly distinct pattern is apparent at the first two measurement locations with the maximum turbulent kinetic energy occurring at 23.3 d_h. The axial component is on average higher in the

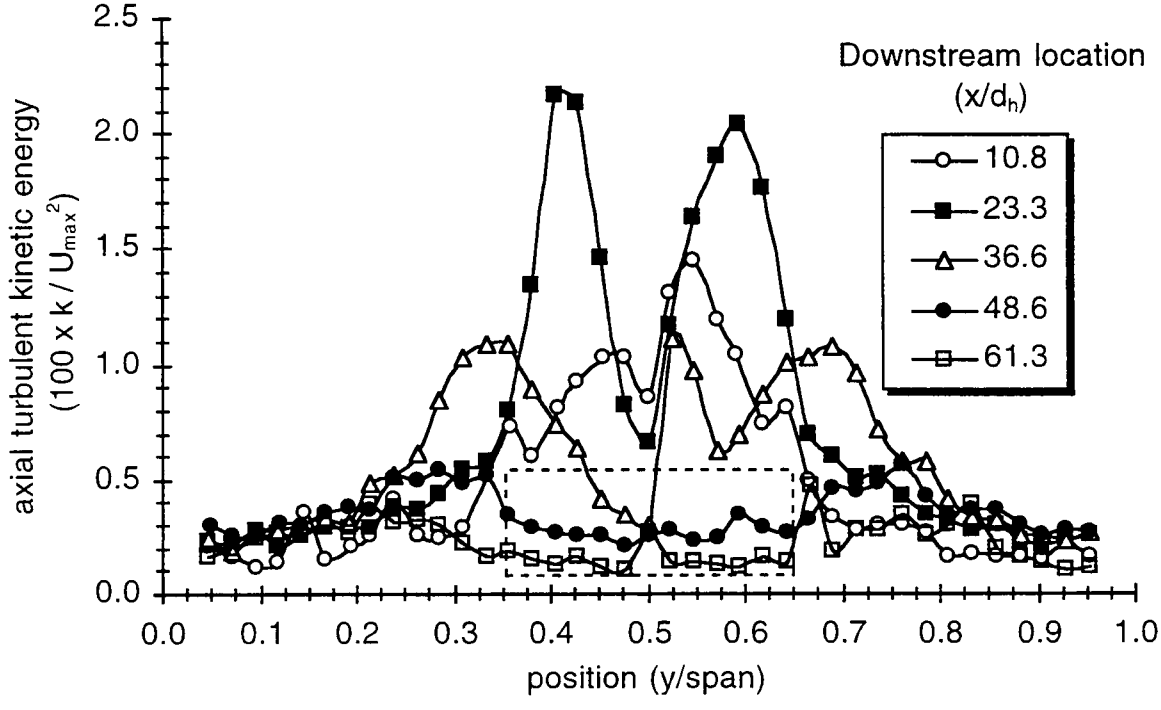


Figure 12. Axial turbulent kinetic energy downstream of a 30% inlet blockage

wake region with two local maximums that outline the edges of the recirculation region. Subsequent measurement locations downstream, however, fail to capture any further distinct turbulence profiles. As can be seen in Fig. 13, the spanwise component peaks at the center of the channel and increases along the length to a maximum at 36.6 d_h.

Figure 14 shows the recovery characteristics for the series of standard blockages. These are the data points at the five measurement locations that are used in the curve fit to estimate reattachment length. A very interesting observation is that the recovery curves are clustered together with the exception of the 15% center blockage case. This unique trend for the 15% blockage, however, diminishes as you go further down the channel.

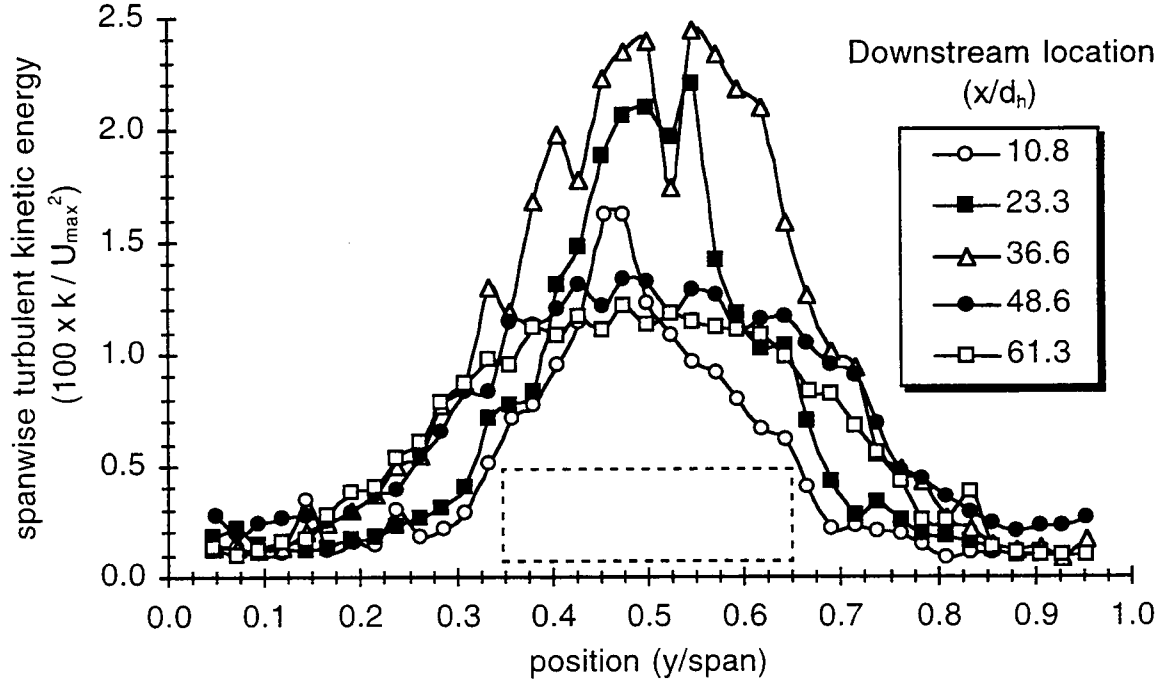


Figure 13. Spanwise turbulent kinetic energy downstream of a 30% inlet blockage

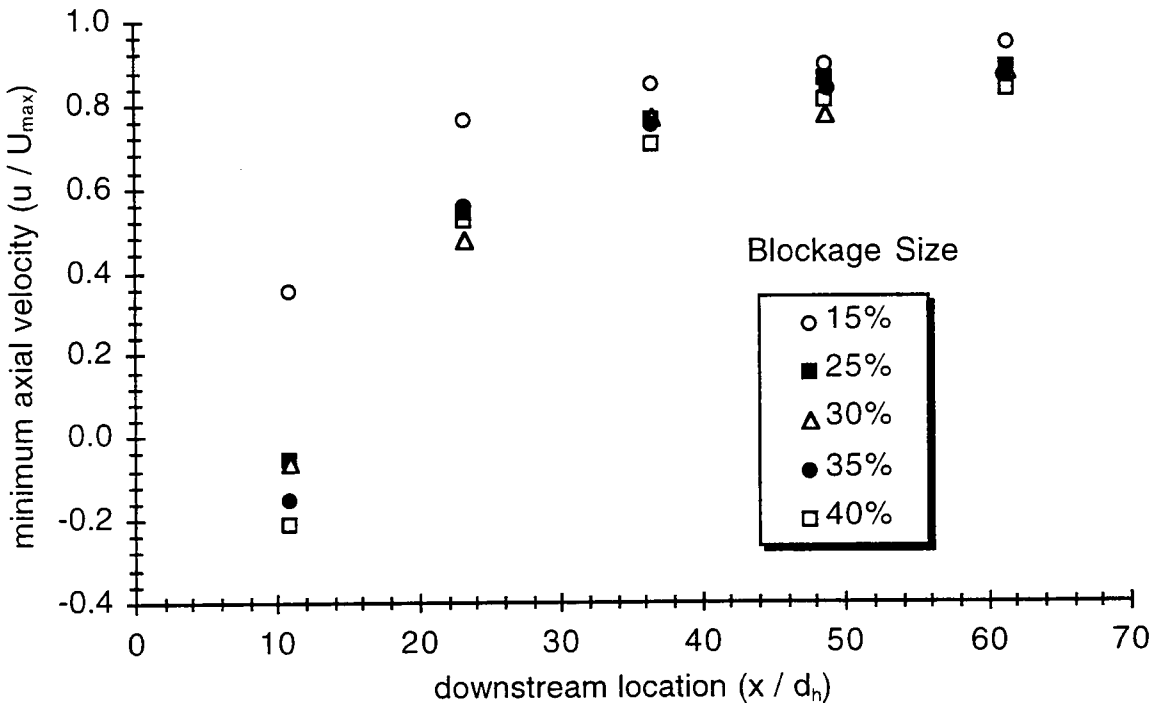


Figure 14. Recovery characteristics for standard blockages

4.2 SHAPE DEPENDENCE

To evaluate the effect of blockage shape on downstream fluid flow behavior, a number of non-standard blockages were designed and fabricated. It is important to note that although these blockages vary in width and shape, all blockages are 10 mm thick and are positioned in the center of the channel span. These blockages include a 40% blockage with rounded edges, a 25% triangular blockage ,20/40% trapezoidal blockage, and a 40% parallelogram blockage. Dimensions for these blockages can be found in Fig. 15.

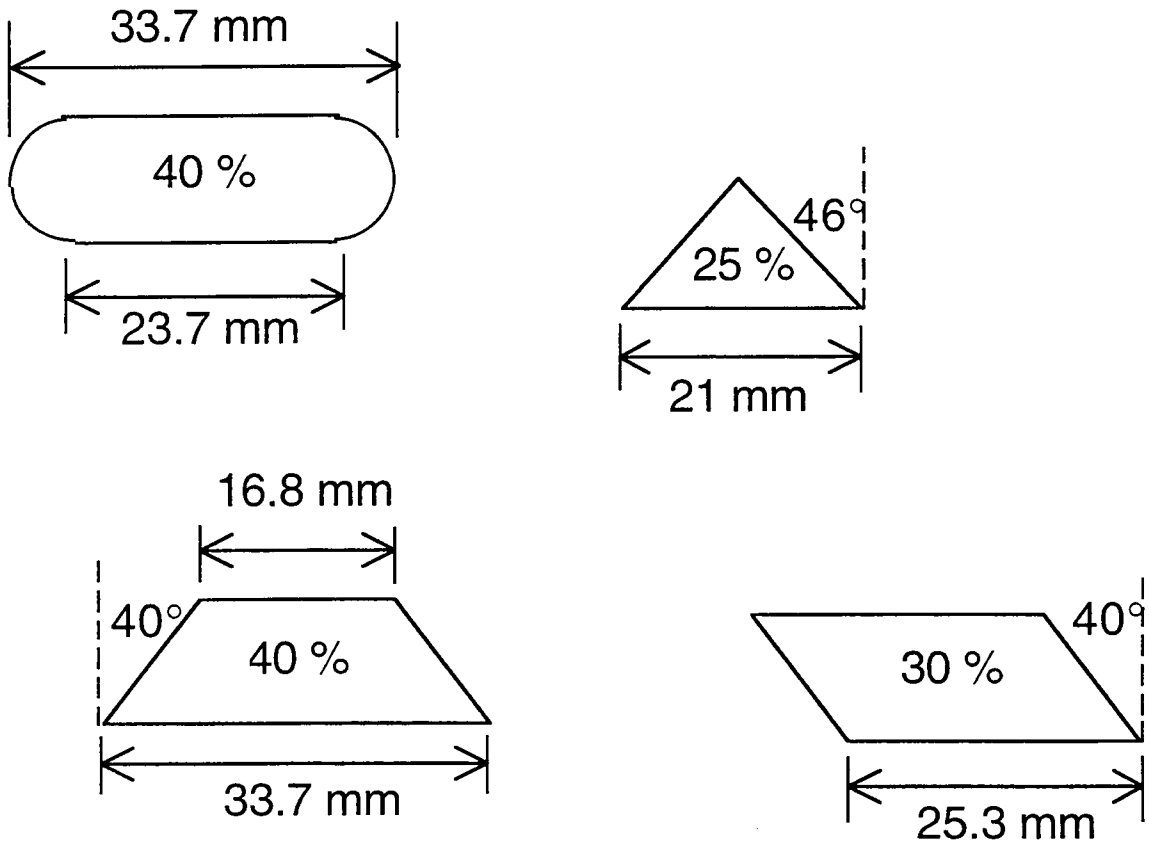


Figure 15. Alternate inlet blockage shapes and dimensions

The 40% smooth blockage is a blockage with a 23.7 mm or 28% facial width that smoothly expands to a maximum width of 33.7 mm or 40% at the center with a 5 mm radius of curvature. Essentially it is a 40% blockage with smooth semicircular ends. As can be seen in Fig. 16, reattachment for a 40% smooth center inlet blockage occurs between 10.8 and 23.3 d_h. From the curve fit of the minimum velocities, the reattachment length was approximated at 11.6 d_h (28.98 mm) or 0.86 blockage widths downstream. The resulting average mid-gap velocity of 17.8 m/s reflects a 4.3% overall velocity defect. The negative velocity magnitude observed in the first measurement window was 7%

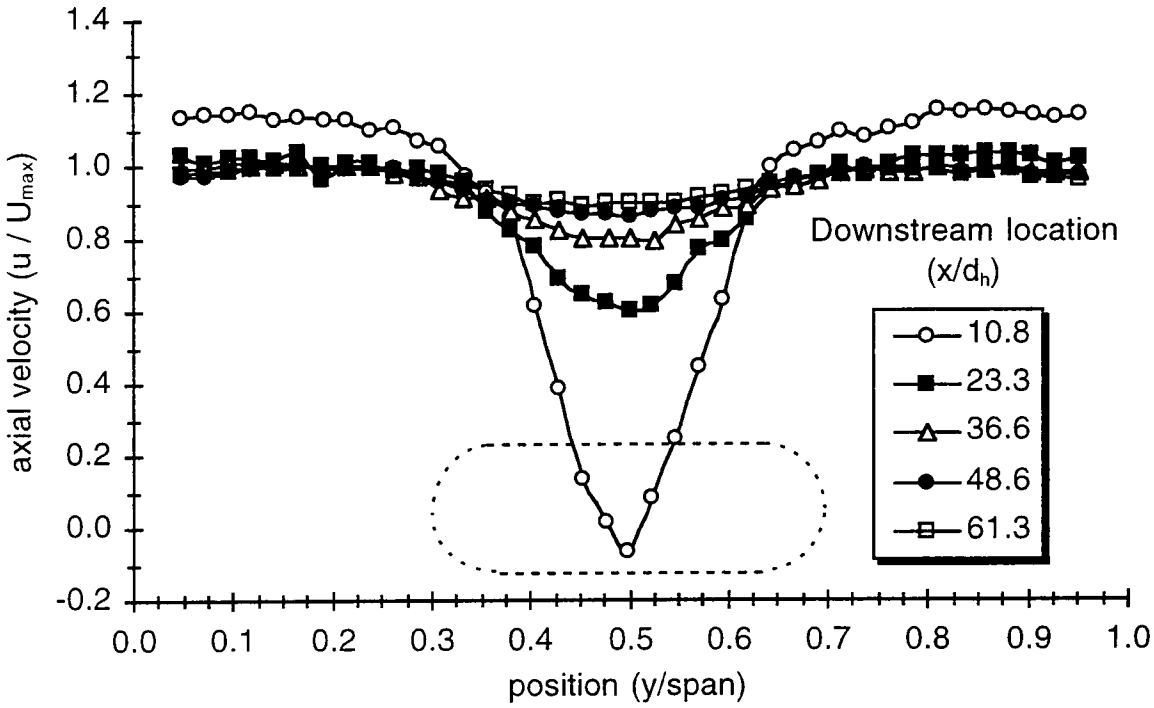


Figure 16. Axial velocity profiles downstream of a 40% smooth inlet blockage

of the unblocked velocity. By the fifth measurement window at 61.3 d_h, the mid-span velocity has recovered to 89% of the unblocked velocity.

The most logical standard blockages with which to compare the 40% smooth blockage are the 40% and 30% standards. As can be seen in Fig. 17, the 40% smooth blockage deflects the flow far less than the 40% standard. A possible explanation for these results would be the fact that the point of separation in each case is different. For the 40% standard blockage, the points of separation undoubtedly occur at the sharp leading and trailing edges of the blockage. For open channel flow past a circular cylinder, it has been shown that while laminar separation occurs around 82°, turbulent separation occurs at

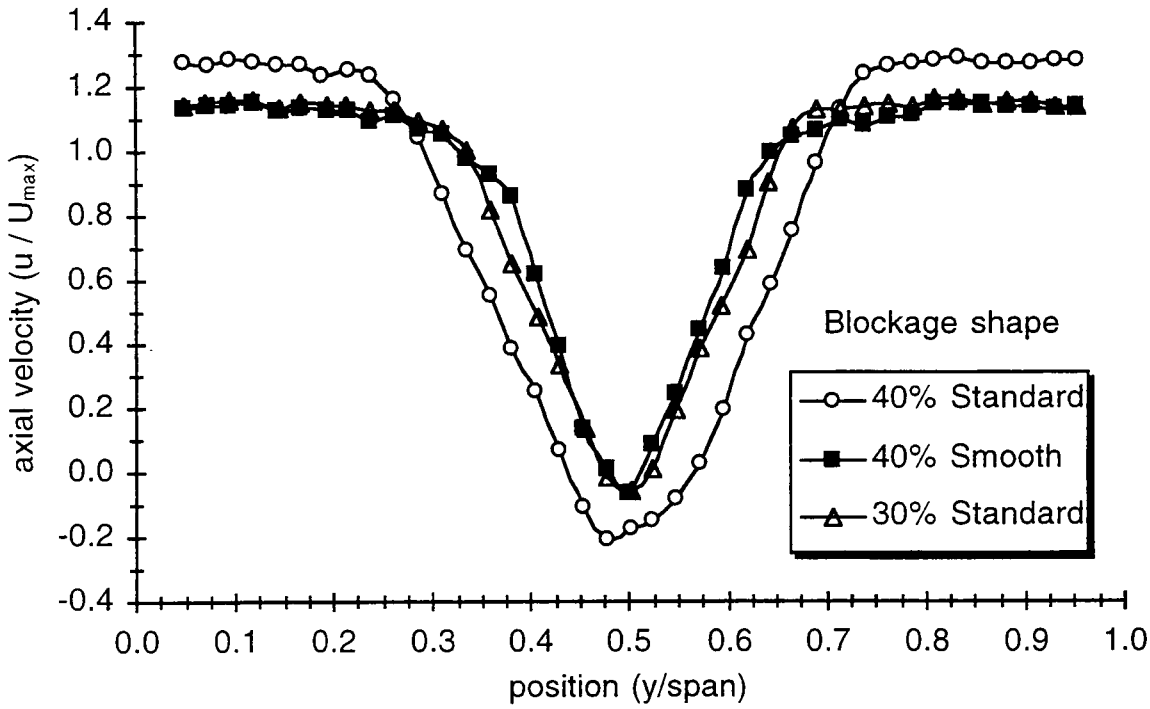


Figure 17. Comparison of axial velocity profiles 10.8 d_h downstream of a 40% smooth and 40 and 30% standard center inlet blockages

approximately 120° (White, 1986). This would imply that the semi-circular edges on the 40% smooth blockage would delay separation to some point beyond 120° resulting in a narrower wake. Assuming that the flow did separate at 120°, this separation point would correspond to the same as for a 38% square edge blockage. When compared to a 30% standard blockage, the 40% smooth blockage appears strikingly similar, with the 40% smooth exhibiting a slightly narrower wake region. When comparing the two cases more closely, the overall velocity defect and reattachment length for the 40% smooth blockage are consistent with the apparent narrower wake in Fig. 17. The

overall velocity defect and reattachment length for the 40% smooth and 30% standard blockages are 4.3%, 4.8%, 11.6 d_h (28.98 mm), 11.9 d_h (29.84 mm) respectively. These measurements along with the apparent wake width imply that the separation point for the 40% smooth blockage lies somewhere beyond 170°. Possible explanations for this additional delay in the onset of separation would include the fact that this flow is wall-bounded as opposed to an external flow, as well as the pressure distribution resulting from the sudden contraction from 2.54 to 1.27 mm at the channel inlet.

The 25% converging triangular blockage is a blockage with a 21 mm or 25% facial width that contracts at an angle of approximately 46° to a point. As can be seen in Fig. 18, reattachment for a 25% converging triangular center

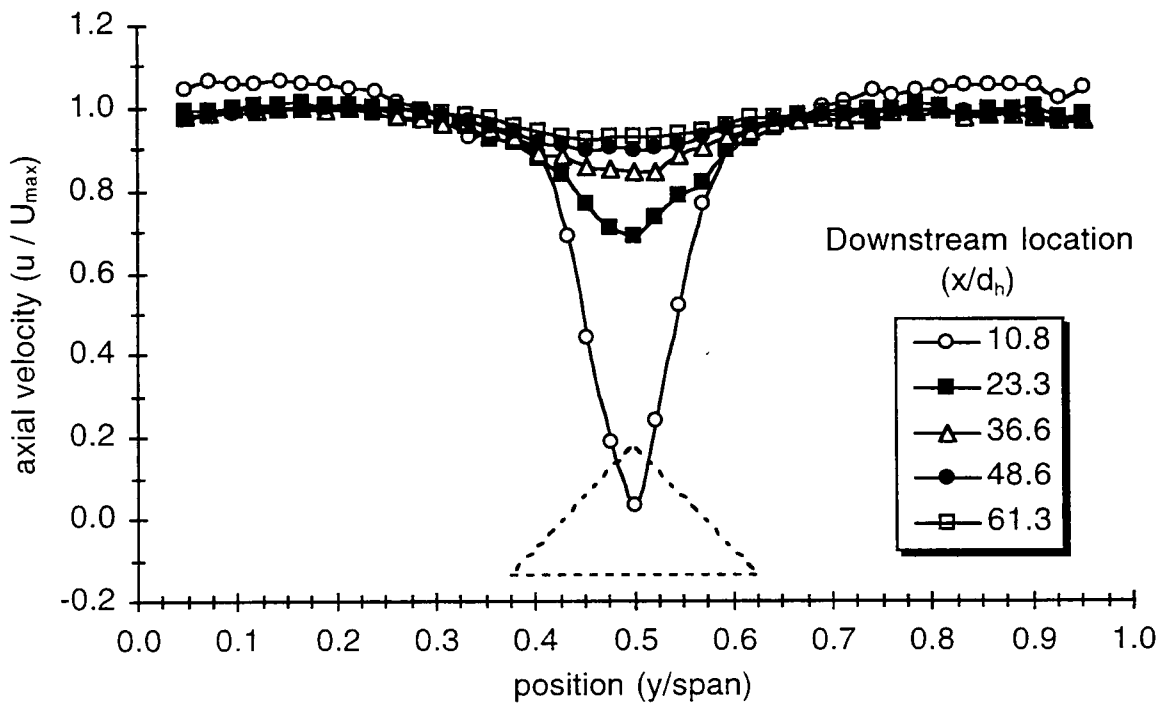


Figure 18. Axial velocity profiles downstream of a 25% converging triangular inlet blockage

inlet blockage occurs somewhere before the first measurement window at 10.8 d_h. From the curve fit of the minimum velocities, the reattachment length was approximated at 10.5 d_h (26.27 mm) or 1.25 blockage widths downstream. The resulting average mid-gap velocity of 18.1 m/s reflects a 2.7% overall velocity defect. The local minimum velocity of 0.64 m/s, however, 10.8 d_h directly downstream of the blockage corresponds to a 96% local velocity defect. By the fifth measurement window at 61.3 d_h, the mid-span velocity has recovered to 89% of the unblocked velocity.

The 25% diverging triangular blockage is a blockage with a sharp pointed face that expands at an angle of approximately 46° to a downstream facial width of 21 mm or 25%. As can be seen in Fig. 19, reattachment for a

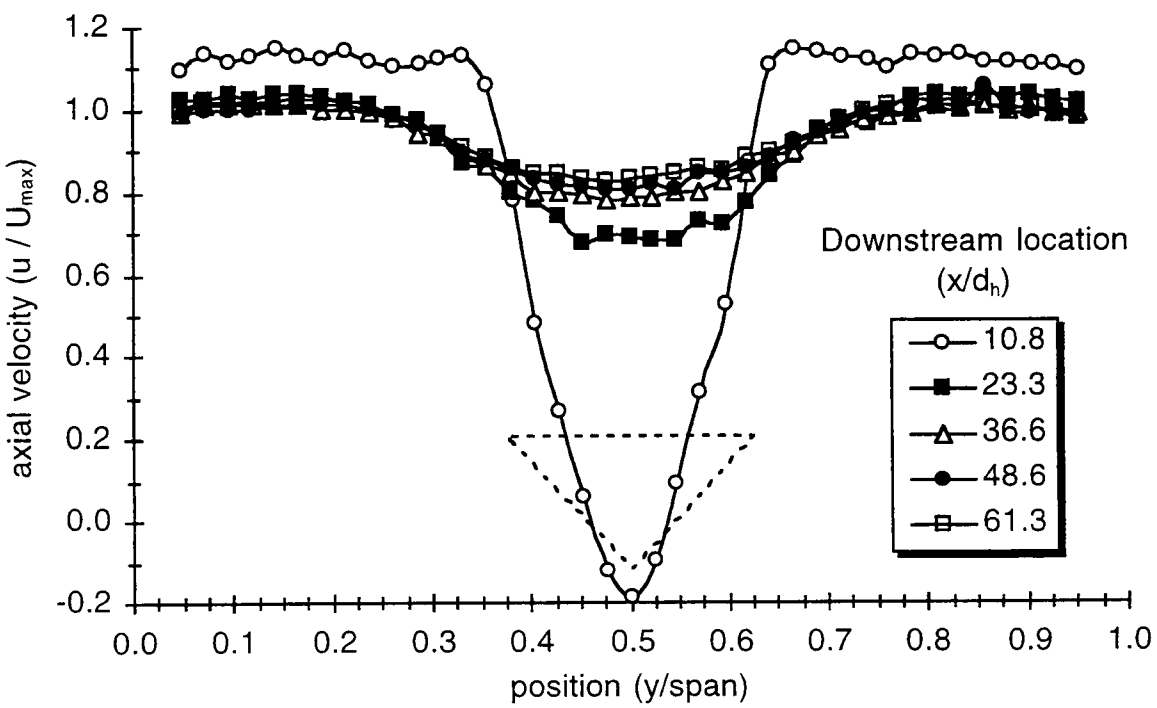


Figure 19. Axial velocity profiles downstream of a 25% diverging triangular inlet blockage

25% diverging triangular center inlet blockage occurs between 10.8 and 23.3 d_h. From the curve fit of the minimum velocities, the reattachment length was approximated at 12.1 d_h (30.39 mm) or 1.45 blockage widths downstream. The resulting average mid-gap velocity of 17.6 m/s reflects a 5.3% overall velocity defect. The negative velocity magnitude observed in the first measurement window was 3% of the unblocked velocity. By the fifth measurement window at 61.3 d_h, the mid-span velocity has recovered to 83% of the unblocked velocity.

The most logical standard blockage with which to compare the 25% diverging and converging triangular blockages is the 25% standard. As anticipated, the diverging triangular blockage (5.3%) deflected the flow more so than the 25% standard square edge blockage (3.7%) while the converging blockage (2.7%) deflected it less. This behavior, however, is counter-intuitive when compared to unbounded external flows. Sparrow and Wachtler (1978) determined that since there were significant differences in the flow fields (no upstream separation region for external flow, wake processes eliminated by walls for internal flow), no particular relationship was expected to exist between bounded and unbounded results. As can be seen in Fig. 20, the diverging triangular blockage apparently causes a slightly wider wake than the 25% standard while the converging blockage has a slightly narrower one.

In all three cases, however, the separation points have the same spanwise location, with only a possible 10 mm shift in their axial positions. From this, it is concluded that the maximum wake width in each of the three cases is the same,

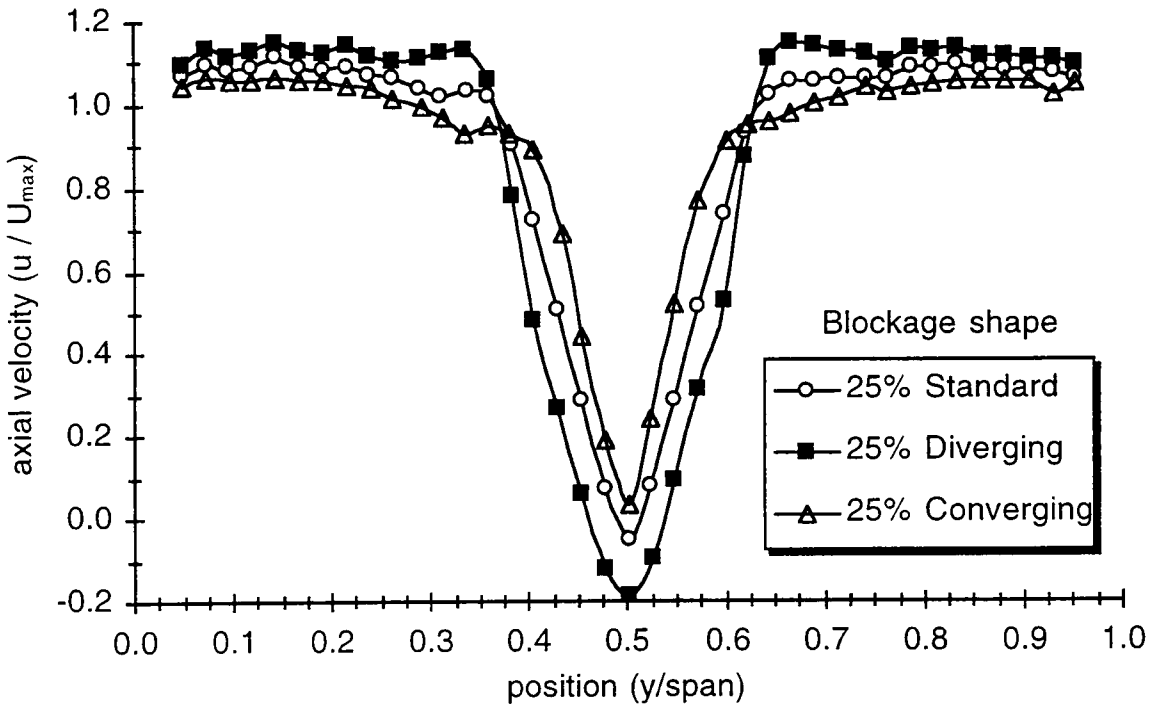


Figure 20. Comparison of axial velocity profiles 10.8 d_h downstream of 25% standard, 25% diverging, and 25% converging center inlet blockages

but the rate of recovery or the decay of the wake is different. With this in mind, the profiles observed in fig ? show that the diverging triangular blockage results in a prolonged recovery as compared to the standard, whereas the converging blockage results in a shortened recovery. These observations are confirmed by the estimated reattachment lengths for the standard as well as the diverging and converging triangular center inlet blockages which are: 11.5, 12.1, and 10.5 d_h respectively.

As can be seen in Fig. 21, the spanwise velocity vectors are directed into the low pressure region directly behind the blockage. When compared to the

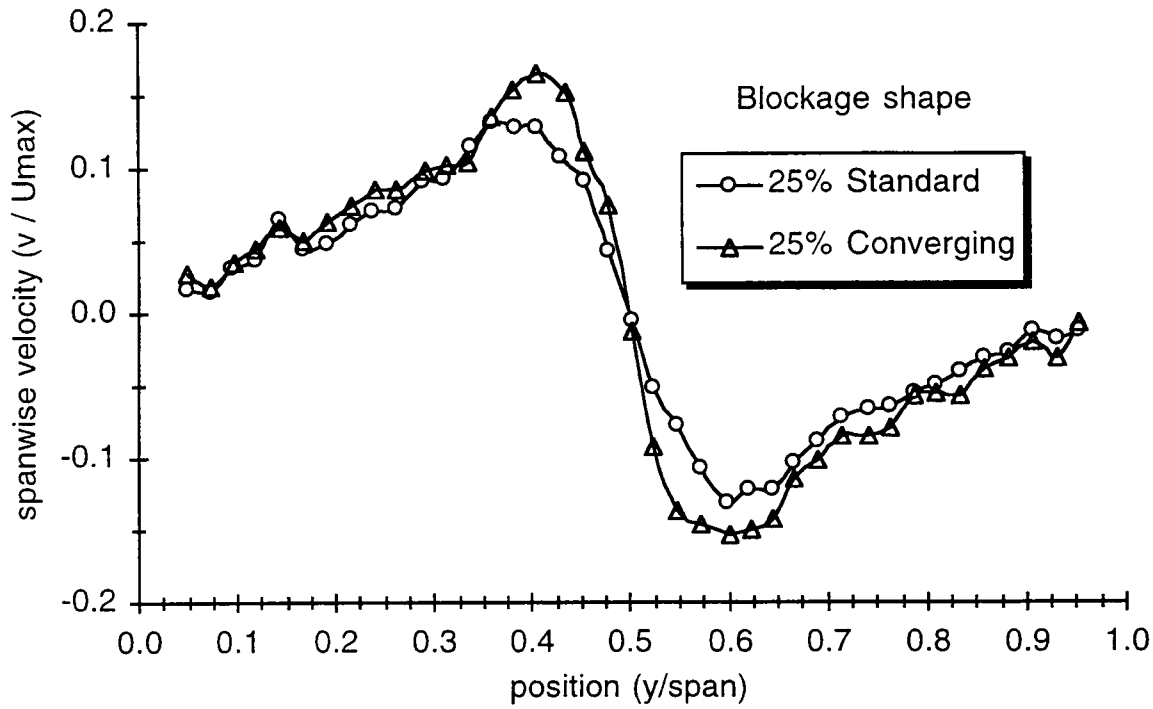


Figure 21. Comparison of spanwise velocity profiles 10.8 d_h downstream of 25% standard and 25% converging center inlet blockages

standard 25% blockage, one can readily see that the converging triangular blockage results in higher spanwise velocities. These higher spanwise velocities are due to the streamlining of the blockage by a favorable trailing edge which helps to "steer" the flow into the low pressure region thus promoting a shorter recovery. The diverging triangular blockage, on the other hand, prolongs the recovery by "steering" the flow away from the low pressure region. Although the fluid will inevitably flow into the low pressure region of the wake, it must first overcome the opposing spanwise momentum imparted by the blockage.

In an attempt to quantify the effect of the blockage shape/orientation, overall velocity defects for each case were compared to the standard. As discussed previously, the average velocities for the standard, diverging, and converging blockages are 17.9, 17.6, and 18.1 m/s respectively. In comparison to the 25% standard blockage, this reflects a 1.68% lower velocity for the diverging triangular blockage while the converging blockage raises the average velocity by 1.12%. An orientation factor serves as a measure of the proportionality by which the diverging configuration of this blockage affects the overall velocity defect as compared to the converging configuration. The resulting diverging/converging orientation factor of 1.5 is calculated, as shown in Eq. (5), by dividing the velocity deviation from the diverging blockage by the deviation from the converging blockage .

$$O_{dc} = \frac{\overline{u_d} - \overline{u_{std}}}{\overline{u_c} - \overline{u_{std}}} \tag{5}$$

where,

$\overline{u_c}$ = average mid-gap velocity across the channel span for a converging non-standard blockage

$\overline{u_d}$ = average mid-gap velocity across the channel span for a diverging non-standard blockage

$\overline{u_{std}}$ = average mid-gap velocity across the channel span for a standard blockage

This form was selected so that a diverging/converging orientation factor of 1.0 would reflect a condition in which the magnitude of the velocity deviation would be the same for both diverging and converging blockage orientations.

The 20/40% diverging trapezoidal blockage is a blockage with a 16.8 mm or 20% facial width that expands to a width of 33.7 mm or 40%. As can be seen in Fig. 22, reattachment for a 20/40% diverging trapezoidal center inlet blockage occurs between 10.8 and 23.3 d_h. From the curve fit of the minimum velocities, the reattachment length was approximated at 12.9 d_h (32.20 mm) or 0.96 blockage widths (maximum width) downstream. The resulting average mid-gap velocity of 16.0 m/s reflects a 14% overall velocity defect. The negative

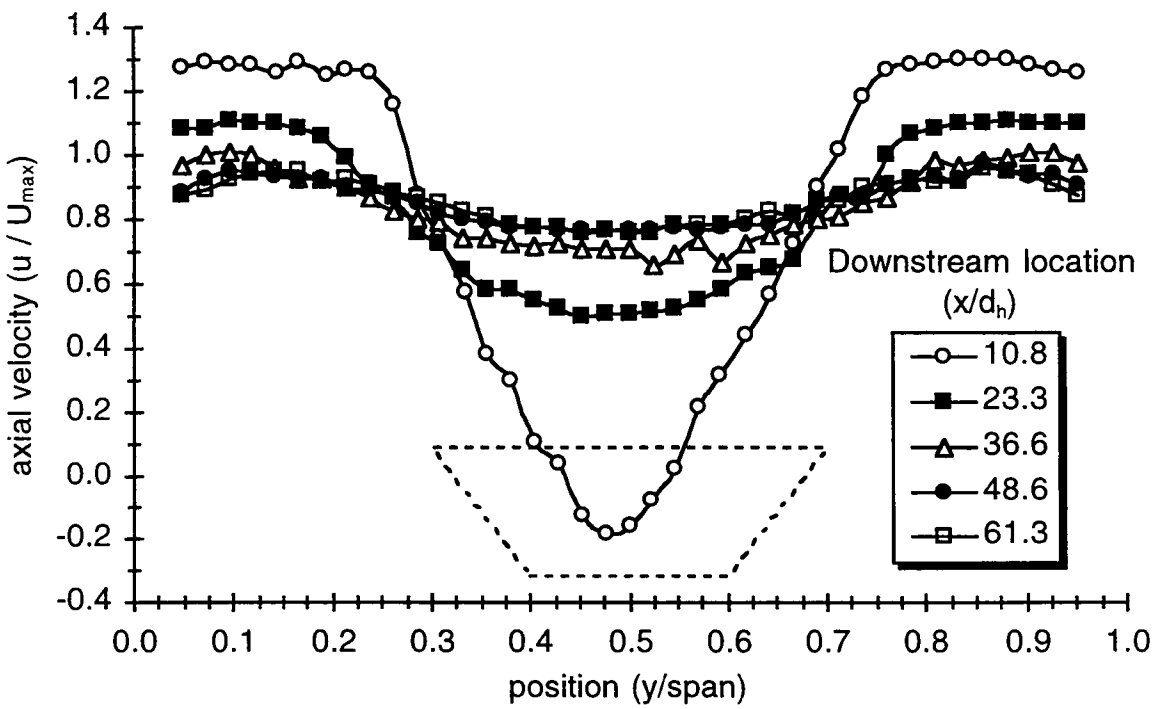


Figure 22. Axial velocity profiles downstream of a 20/40% diverging trapezoidal inlet blockage

velocity magnitude observed in the first measurement window was 18% of the unblocked velocity. By the fifth measurement window at 61.3 d_h, the mid-span velocity has recovered to only 76% of the unblocked velocity.

The 40/20% converging trapezoidal blockage is a blockage with a 33.7 mm or 40% facial width that contracts to a width of 16.8 mm or 20%. As can be seen in Fig. 23, reattachment for a 40/20% converging trapezoidal center inlet blockage occurs between 10.8 and 23.3 d_h. From the curve fit of the minimum velocities, the reattachment length was approximated at 11.3 d_h (28.29 mm) or 0.84 blockage widths (maximum width) downstream. The resulting average mid-gap velocity of 17.3 m/s reflects a 7% overall velocity defect. The negative

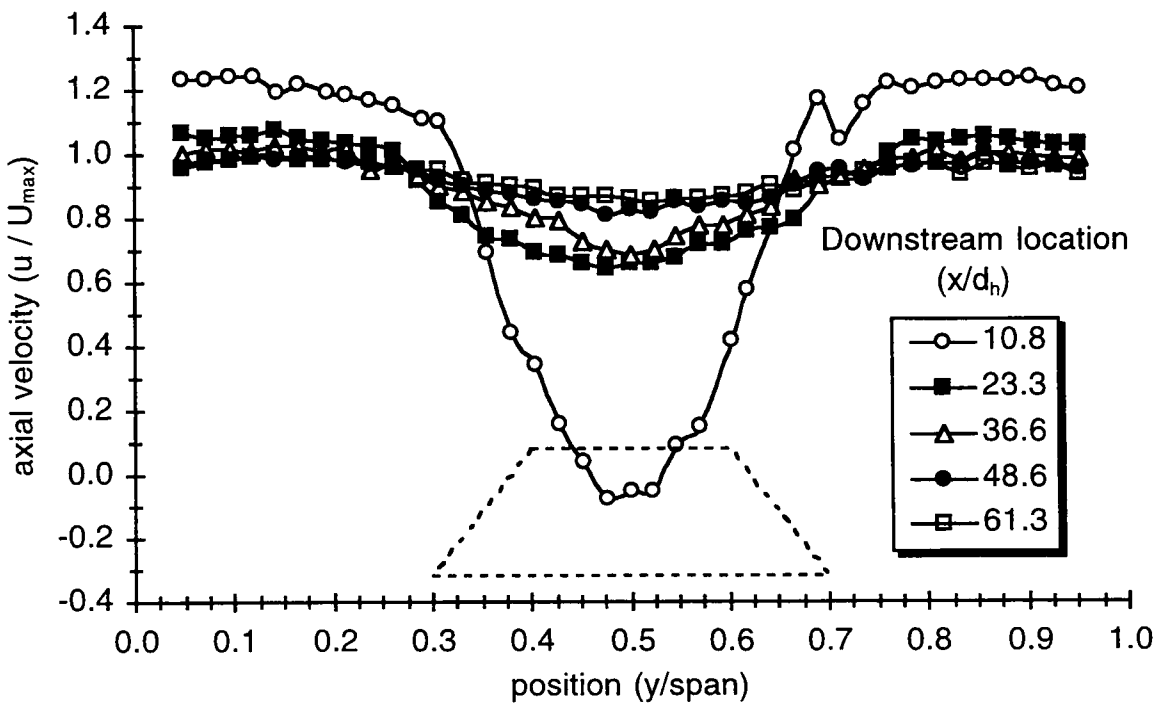


Figure 23. Axial velocity profiles downstream of a 40/20% converging trapezoidal inlet blockage

velocity magnitude observed in the first measurement window was 5% of the unblocked velocity. By the fifth measurement window at 61.3 d_h, the mid-span velocity has recovered to 85% of the unblocked velocity.

The most logical standard blockage with which to compare the 20/40% diverging and 40/20% converging trapezoidal blockages is the 40% standard. The trends are similar to those observed for the converging and diverging triangular blockages. The profiles observed in Fig. 24 show that the diverging trapezoidal blockage results in a prolonged recovery as compared to the standard, whereas the converging blockage results in a shortened recovery.

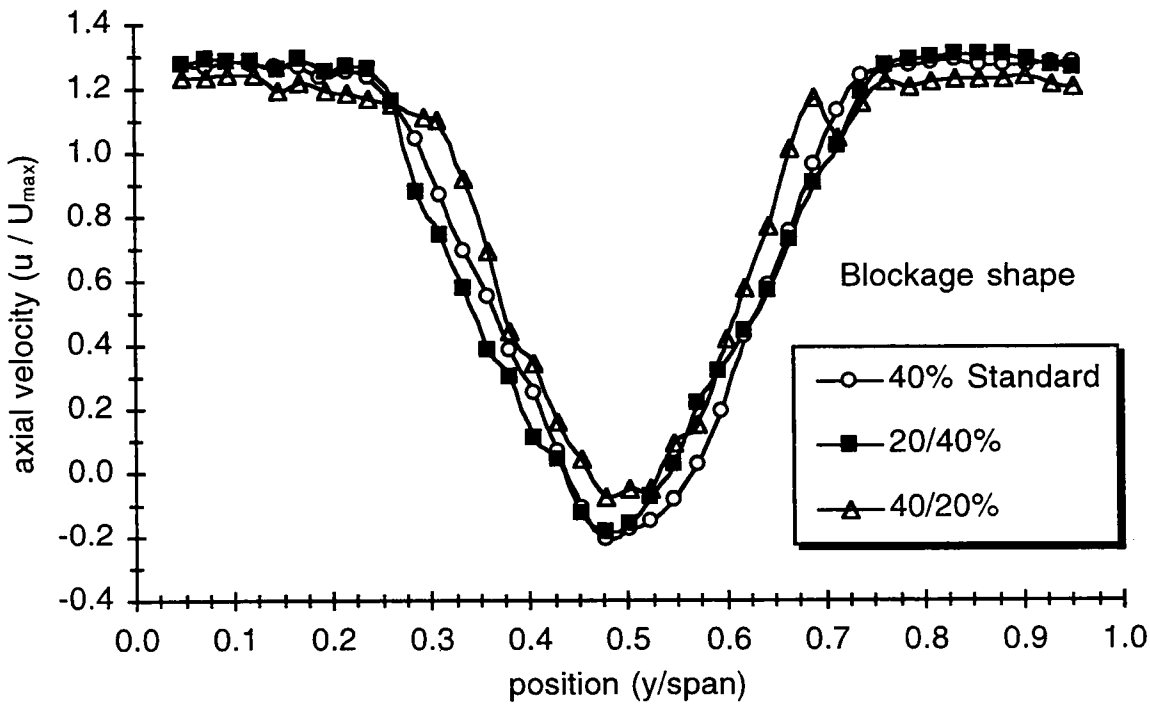


Figure 24. Comparison of axial velocity profiles 10.8 d_h downstream of 40% standard, 20/40% diverging, and 40/20% converging center inlet blockages

These observations are confirmed by the estimated reattachment lengths for the standard, diverging, and converging triangular center inlet blockages which are: 12.7, 12.9, and 11.3 d_h respectively.

In an attempt to quantify the effect of the blockage shape/orientation, overall velocity defects for each case were compared to the standard. As discussed previously, the average velocities for the standard, diverging, and converging blockages are 16.8, 16.0, and 17.3 m/s respectively. In comparison to the 40% standard blockage, this reflects a 4.76% lower velocity for the diverging triangular blockage while the converging blockage raises the average velocity by 2.98%. The resulting diverging/converging orientation factor (O_{dc}) for the trapezoidal blockage configuration is 1.597 as compared to 1.5 for the triangular blockage. This may reflect some dependence of the orientation factor upon total blockage size.

The 30% parallelogram blockage is a blockage with a 25.3 mm or 30% facial width that is skewed at a 40° angle. As can be seen in Fig. 25, reattachment for a 30% parallelogram center inlet blockage occurs between 10.8 and 23.3 d_h. From the curve fit of the minimum velocities, the reattachment length was approximated at 13.0 d_h (32.58 mm) or 1.29 blockage widths (facial width) downstream. The resulting average mid-gap velocity of 16.4 m/s reflects a 11.8% overall velocity defect. The negative velocity magnitude observed in the first measurement window was 20% of the unblocked velocity. By the fifth

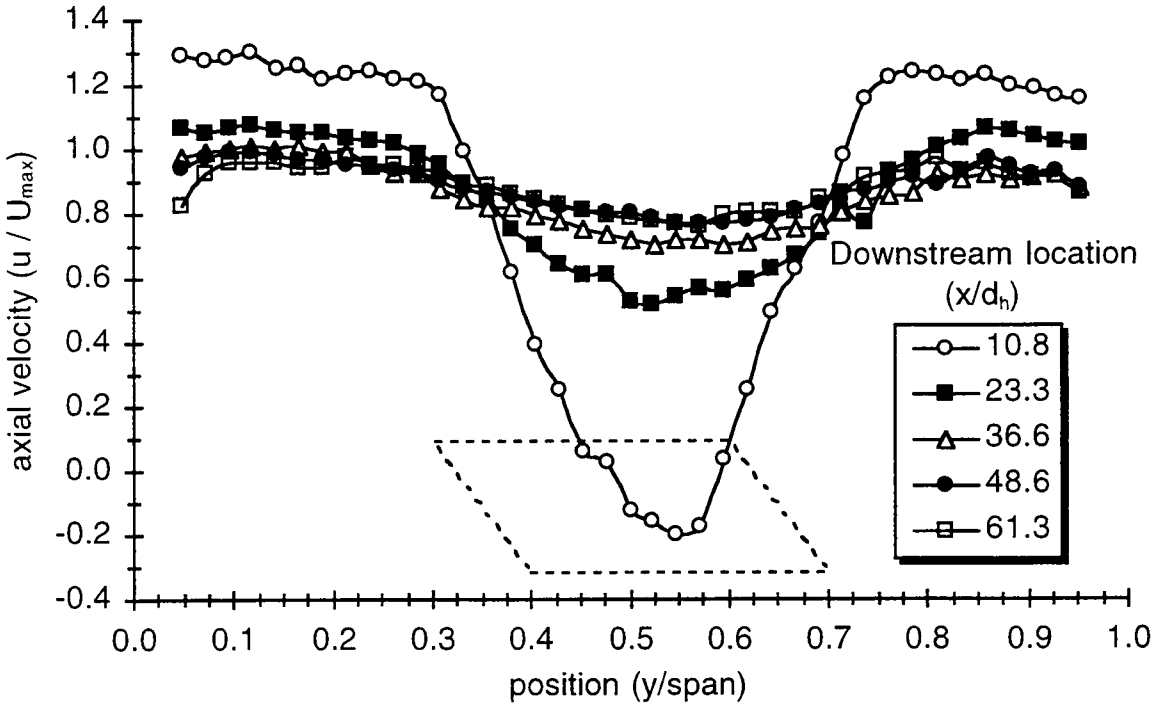


Figure 25. Axial velocity profiles downstream of a 30% parallelogram inlet blockage

measurement window at 61.3 d_h, the mid-span velocity has recovered to 77% of the unblocked velocity.

The most logical standard blockages with which to compare the 30% parallelogram blockage are the 30% and 40% standards. From the velocity profiles in Fig. 26, the 30% parallelogram blockage looks more like a 40% standard blockage shifted slightly to the right. Although the 30% parallelogram blockage restricts only 30% of the flow area, the resulting velocity profiles resemble a 40% blockage due to its effective maximum wake width of 33.6 mm or 40%. Upon closer investigation, the 30% parallelogram blockage actually deflects more of the flow than even the 40% standard blockage. These

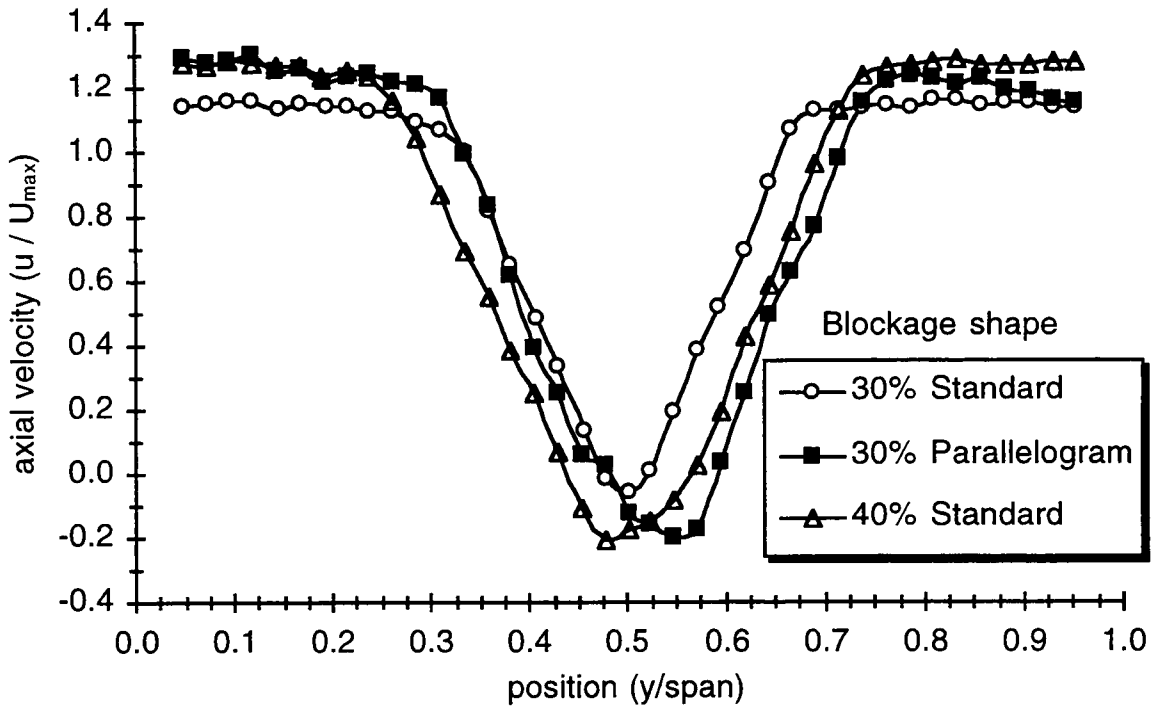


Figure 26. Comparison of axial velocity profiles 10.8 d_h downstream of 30% standard, 30% parallelogram, and 40% standard center inlet blockages

observations are confirmed by the overall velocity defects for the 30% parallelogram, 30%, and 40% standard center inlet blockages which are: 11.8, 4.8, and 9.7% respectively.

Previous experience in determining orientation factors for the trapezoidal and triangular blockages has led to the conclusion that blockage shapes which tend to divert the flow away from the low pressure wake have a greater impact than do complementary shapes that are streamlined with favorable trailing edges. A reason previously postulated for this is that such diverting blockages create a directional momentum that must be overcome before the flow can fully

recover. The benefits of a streamlined blockage, however, are quite obvious in both external and internal flows. In internal flows with thin inlet boundary layers, for example, sudden expansions are much larger sources of losses than are gradual expansions for angles less than 60° (White, 1986). With this in mind, it is not surprising that a converging triangular or trapezoidal blockage would have a shorter reattachment length and higher average velocity than their standard square edge equivalents.

Once it had been established that the 30% parallelogram blockage behaved more like a 40% blockage with one adverse and one favorable trailing edge, it seemed appropriate that applying half of the divergent and convergent adjustments (-4.76% and +2.98% or 0.9524 and 1.0298) observed in the trapezoidal configuration to the 40% standard blockage would yield good agreement with the experimental results. Such a calculation predicted an average velocity of 16.65 m/s after multiplying 0.991 (0.9762 x 1.0149) by the 40% standard average velocity of 16.8 m/s. This did not compare well to the experimental value of 16.4. Closer examination reveals that this may not be the ideal correction factor to use. Unlike the triangular and trapezoidal blockages, the parallelogram blockage has the same upstream and downstream face width. If the replacement of a sudden expansion with a gradual expansion (in the case of the triangular blockage) or a gradual expansion coupled with a smaller sudden expansion (in the case of a trapezoidal blockage) is the primary cause of the reduction in pressure loss, it

may not be appropriate to apply any favorable adjustment to the standard 40% blockage results. If the velocity is corrected simply by applying half of the 4.76% divergent velocity reduction, the predicted average velocity becomes 16.4 m/s. Although this approach seems reasonable fits the parallelogram data well, there is no known theoretical justification for it and may not hold for different blockage configurations.

4.3 POSITION DEPENDENCE

In an attempt to evaluate the effect of blockage position on downstream fluid flow behavior, a series of 15% blockages were designed and fabricated. It is important to note that although these blockages vary in position, all blockages are 10 mm thick and block either 15% of the channel span for single blockages or 30% for dual blockages. These blockages include off-center blockages (Fig. 27) positioned 35 (14.7), 65 (27.3), and 82% (34.4 mm) off-center as well as dual 15% blockages (Fig. 28) with 5 (42) and 20% (16.9 mm) openings.

The 35% off-center 15% blockage is a square blockage positioned 14.7 mm to the left of the center or 20.93 mm from the edge of the channel. As can be seen in Fig. 29, reattachment for a 35% off-center 15% inlet blockage occurs somewhere before the first measurement window at 10.8 d_h. From the curve fit of the minimum velocities, the reattachment length was approximated at 8.6 d_h (21.6 mm) or 1.71 blockage widths downstream. The resulting average mid-gap velocity of 18.3 m/s reflects a 1.6% overall velocity defect. The local

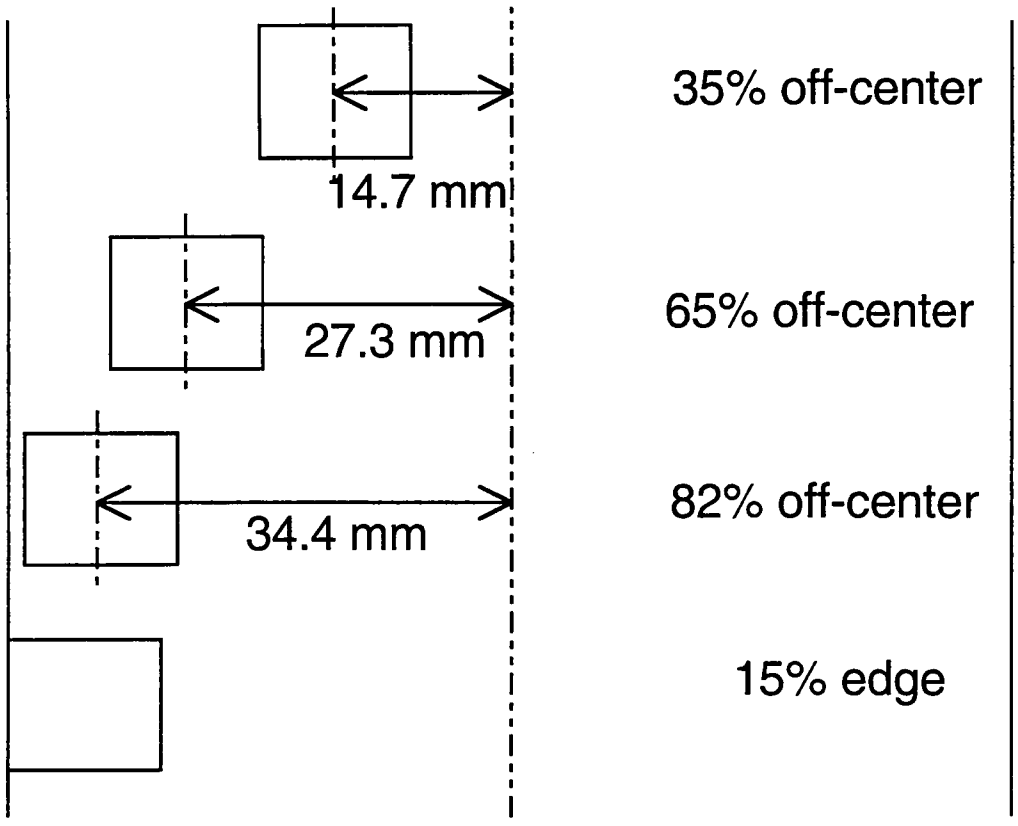


Figure 27. Off-center 15% blockage positions

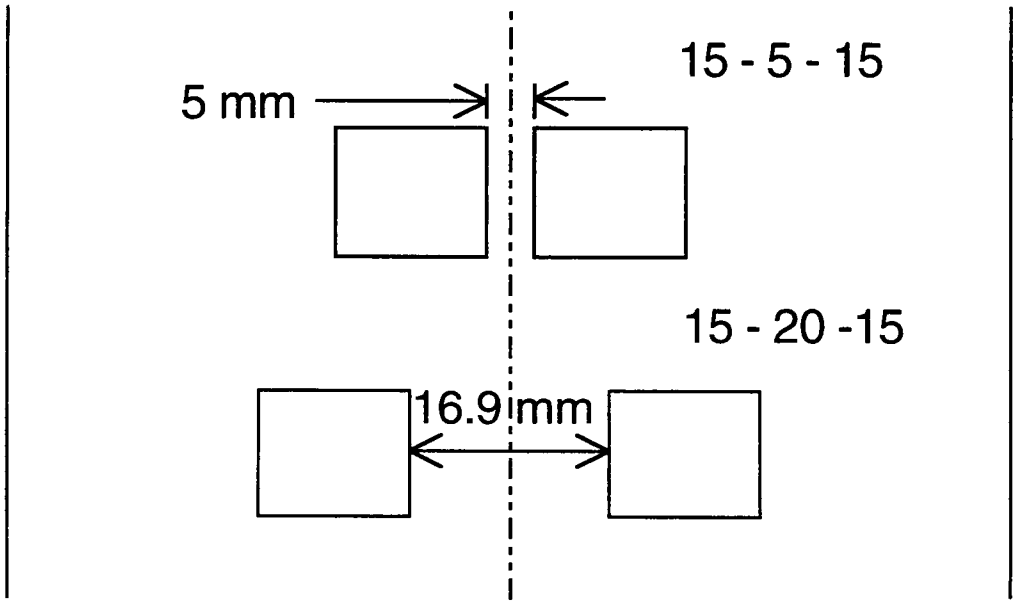


Figure 28. Dual 15% center blockage positions

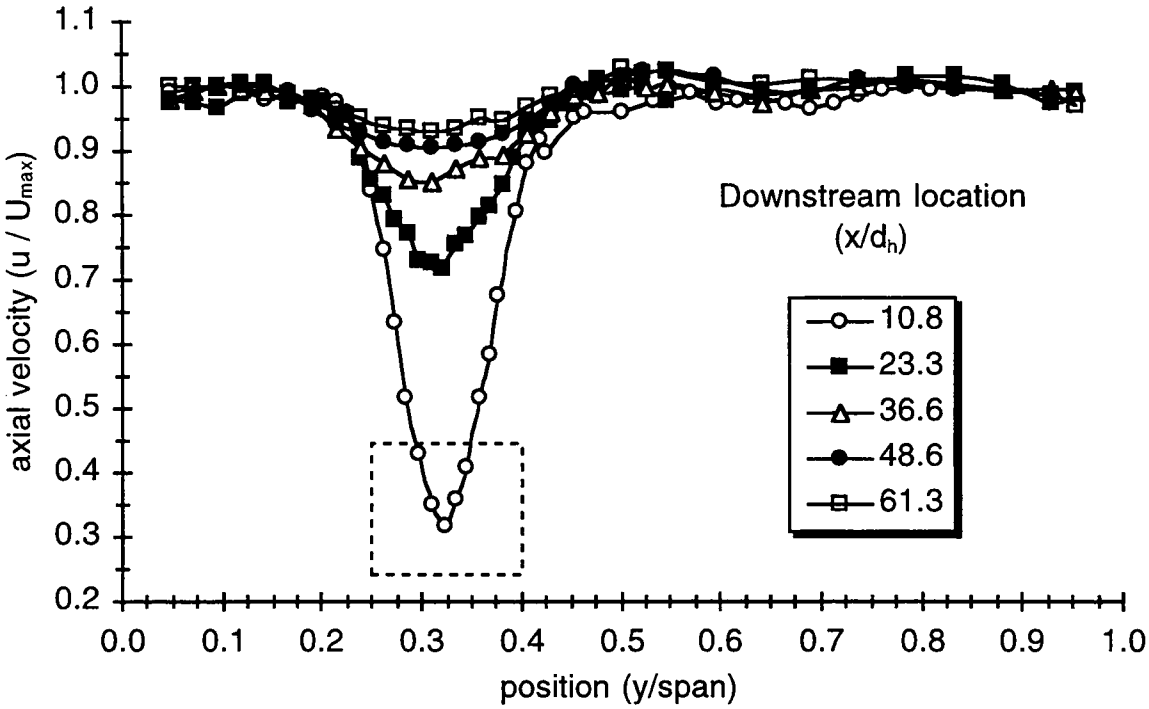


Figure 29. Axial velocity profiles downstream of a 15% square inlet blockage positioned 35% off center

minimum velocity of 5.9 m/s, however, 10.8 d_h directly downstream of the blockage corresponds to a 68% local velocity defect. By the fifth measurement window at 61.3 d_h, the minimum velocity has recovered to 93% of the unblocked velocity.

The 65% off-center 15% blockage is a square blockage positioned 27.3 mm to the left of the center or 8.382 mm from the edge of the channel. As can be seen in Fig. 30, reattachment for a 65% off-center 15% inlet blockage occurs somewhere before the first measurement window at 10.8 d_h. From the curve fit of the minimum velocities, the reattachment length was approximated at 8.9 d_h (22.3 mm) or 1.77 blockage widths downstream. The resulting average mid-

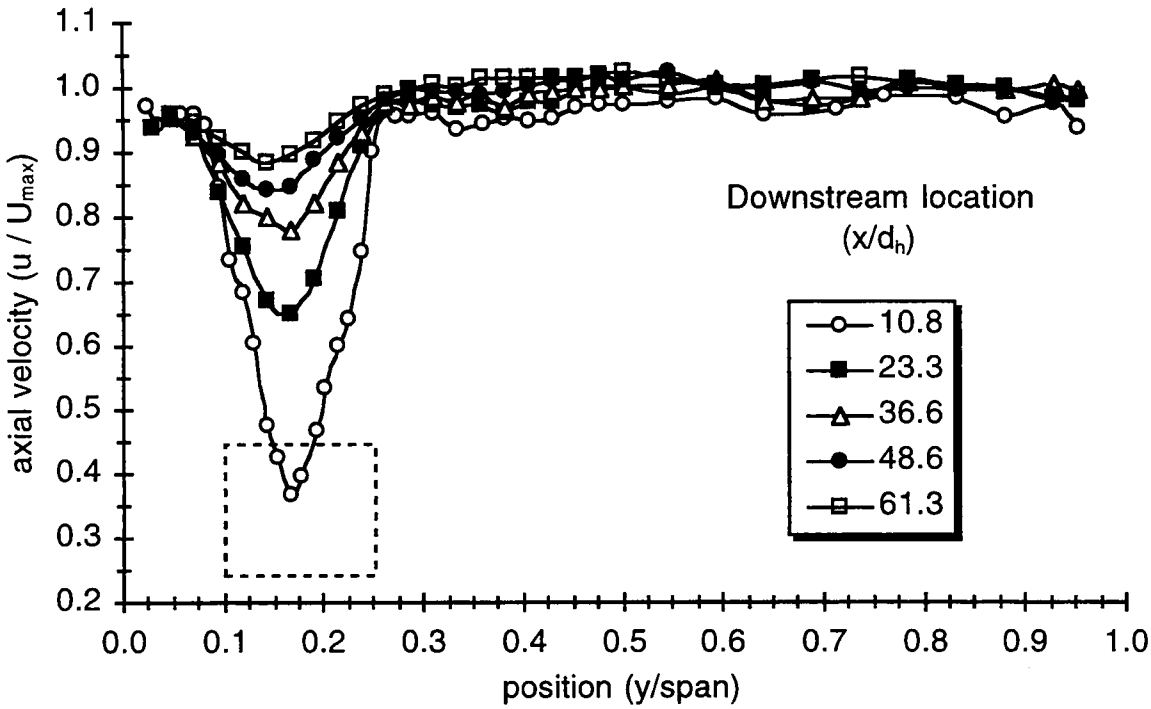


Figure 30. Axial velocity profiles downstream of a 15% square inlet blockage positioned 65% off center

minimum velocity of 6.9 m/s, however, 10.8 d_h directly downstream of the blockage corresponds to a 63% local velocity defect. By the fifth measurement window at 61.3 d_h, the minimum velocity has recovered to 88% of the unblocked velocity.

The 82% off-center 15% blockage is a square blockage positioned 34.4 mm to the left of the center or 1.27 mm from the edge of the channel. As can be seen in Fig. 31, reattachment for an 82% off-center 15% inlet blockage occurs somewhere before the first measurement window at 10.8 d_h. From the curve fit of the minimum velocities, the reattachment length was approximated at 10 d_h (25 mm) or 1.98 blockage widths downstream. The resulting average mid-gap

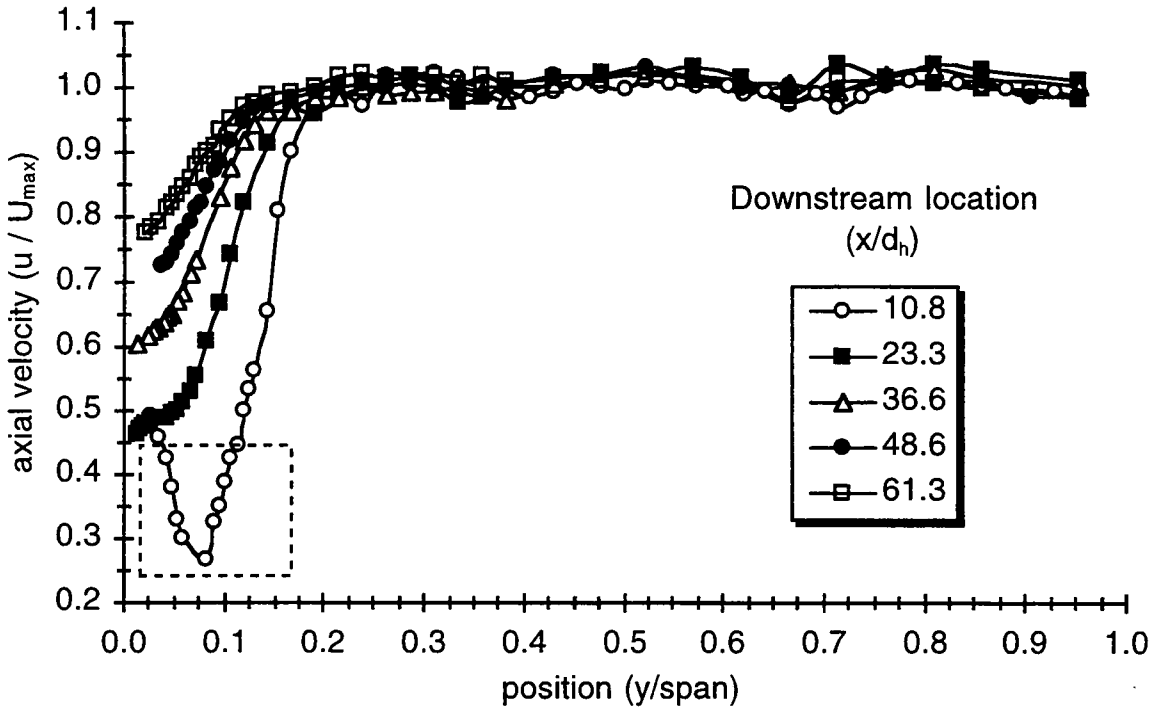


Figure 31. Axial velocity profiles downstream of a 15% square inlet blockage positioned 82% off center

velocity of 17.7 m/s reflects a 4.8% overall velocity defect. The local minimum velocity of 5.0 m/s, however, 10.8 d_h directly downstream of the blockage corresponds to a 73% local velocity defect. By the fifth measurement window at 61.3 d_h, the minimum velocity has recovered to only 78% of the unblocked velocity.

The 15% edge blockage is a square blockage positioned at the edge of the channel. As can be seen in Fig. 32, reattachment for a 15% edge inlet blockage occurs somewhere before the first measurement window at 10.8 d_h. From the curve fit of the minimum velocities, the reattachment length was approximated at 9.4 d_h (24 mm) or 1.88 blockage widths downstream. The

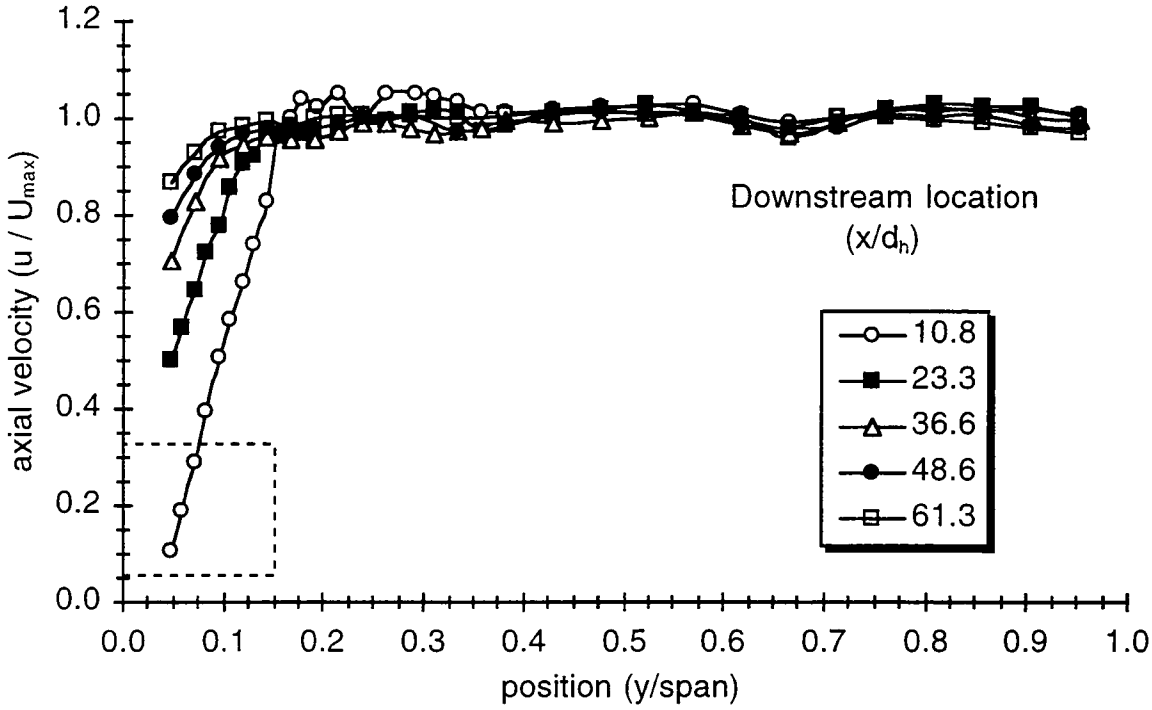


Figure 32. Axial velocity profiles downstream of a 15% square inlet blockage positioned at the edge

resulting average mid-gap velocity of 18.4 m/s reflects only a 1.1% overall velocity defect. The local minimum velocity of 1.9 m/s, however, 10.8 d_h directly downstream of the blockage corresponds to a 90% local velocity defect. By the fifth measurement window at 61.3 d_h, the minimum velocity has recovered to 87% of the unblocked velocity.

The most logical blockage configurations to compare these off-center 15% blockages are the 15% center and 15% edge blockages. Table 1 provides a summary comparison of the 15% blockage at various positions. When comparing a blockage located 35% off-center to the 15% center case, there are no obvious differences. Not only is the average axial velocity the same, but also

the minimum velocities at each measurement location are essentially identical. As can be seen in Fig. 29, the resulting velocity profiles downstream of the 35% off-center 15% blockage are basically the same as for the 15% center but skewed to the left. When comparing the 65% off-center blockage, to the 15% center, there are some minor differences. Although the average velocity is only slightly less at 18.2 m/s, the local minimum velocities confirm this trend.

Initially, there was some concern regarding the local minimum velocities, specifically those measured 10.8 d_h downstream. The minimum velocities for the 0, 35, and 65% off-center blockages were 0.35, 0.32, and 0.37 respectively. Before attempting to derive any meaning from this trend, one must first take note of the corresponding standard deviations. As can be seen by the error bars in Fig. 33 and the tabulated standard deviations in Table 1, any "trends" that could be derived from the local minimum velocities 10.8 d_h downstream are dwarfed by the statistical uncertainties in the measurements. At measurement positions further downstream, however, the standard deviations are lower and such trends can be derived.

The comparison of the 15% blockage positioned 82% off-center to both the 15% center and edge is by far the most interesting. Although the axial velocity profile 10.8 d_h downstream of the 82% off-center blockage in Fig. 31 shows evidence of fluid flow on both sides of the blockage, profiles at subsequent measurement locations appear as if the blockage were positioned at the edge. This is apparently the result of a near-stagnant condition which

Table 1. Summary of 15% positions analysis

Blockage	Measurement Location (d_h)	Minimum Velocity (u / U_{max})	Standard Deviation (σ_u / U_{max})
15% Center (average velocity = 18.3 m/s)	10.8	0.35	0.13
	23.3	0.76	0.09
	36.6	0.84	0.06
	48.6	0.89	0.05
	61.3	0.94	0.05
35% Off-center (average velocity = 18.3 m/s)	10.8	0.32	0.15
	23.3	0.72	0.08
	36.6	0.85	0.06
	48.6	0.90	0.05
	61.3	0.93	0.04
65% Off-center (average velocity = 18.2 m/s)	10.8	0.37	0.12
	23.3	0.65	0.07
	36.6	0.78	0.05
	48.6	0.85	0.05
	61.3	0.88	0.05
82% Off-center (average velocity = 17.7 m/s)	10.8	0.27	0.10
	23.3	0.46	0.06
	36.6	0.61	0.06
	48.6	0.72	0.05
	61.3	0.78	0.04
15% Edge (average velocity = 18.4 m/s)	10.8	0.10	0.07
	23.3	0.50	0.06
	36.6	0.71	0.06
	48.6	0.79	0.06
	61.3	0.87	0.05

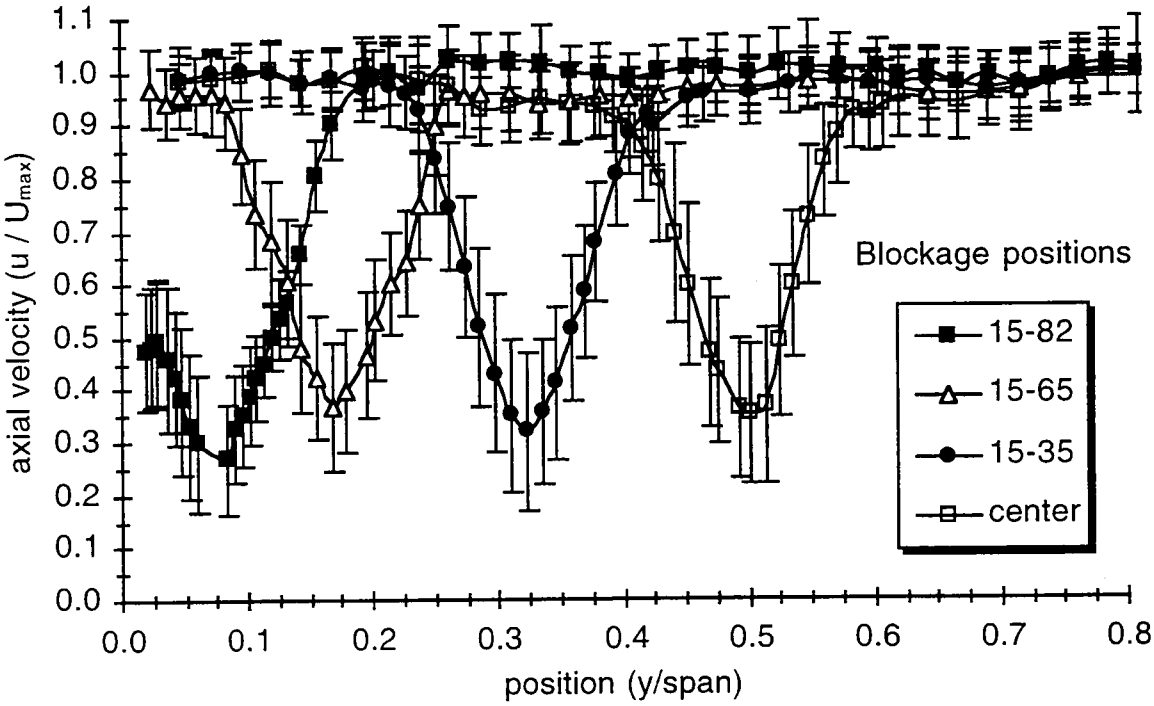


Figure 33. Comparison of axial velocity profiles 10.8 d_h downstream of 15% blockages positioned 0, 35, 65, and 82% off center

exists in the 1.27 mm span between the blockage and the side wall of the channel. Unlike a true central or near-central blockage where the flow rates on either side of the blockage are comparable, the flow rate at the right of this blockage is over twice that through the small 1.27 mm span on the left side. This problem is compounded by the fact that a portion of this small passage is located within the spanwise boundary layer on the channel wall. By the second measurement location 23.3 d_h downstream, the weaker recirculation vortex has completely decayed and the profiles take on the characteristics of a slightly wider edge blockage with a single recirculation vortex. The resulting average velocity for the 82% off-center 15% blockage is slightly less than either the edge

or center 15% blockages. This apparent 3% variation in velocity, however, is well within the experimental uncertainty and, more importantly, is not confirmed by the volumetric flow meter in the loop. The error in the calculation of the average mid-gap velocity is likely introduced as a bias in the numerical integration of the velocity profile. A 10% variation in the minimum velocity at the fifth measurement window, however, provides convincing evidence of a slightly longer recirculation region as compared to the 15% edge. By the fifth measurement window at 61.3 d_h , the mid-span velocity has recovered to only 78% of the unblocked velocity, as opposed to 87% for the edge blockage.

There are also some interesting comparisons between the edge and center 15% blockage. As can be seen in Table 1, the recovery or wake length for a center blockage is shorter than for the corresponding edge. This is not that surprising as center blockages have two strong recirculation vortices to aid recovery, whereas edge blockages have only one. The average velocity, however, for the edge blockage was slightly less than for the center, thus implying higher losses for the edge blocked flow. Although this 0.1 m/s difference is well within the measurement uncertainty, similar observations have been made by previous experimenters (Sparrow et al., 1980).

The 15-5-15 blockage is a pair of 15% square blockages positioned in the center of the channel with a 5% separation gap between. As can be seen in Fig. 34, reattachment for a 15-5-15 inlet blockage occurs somewhere before the

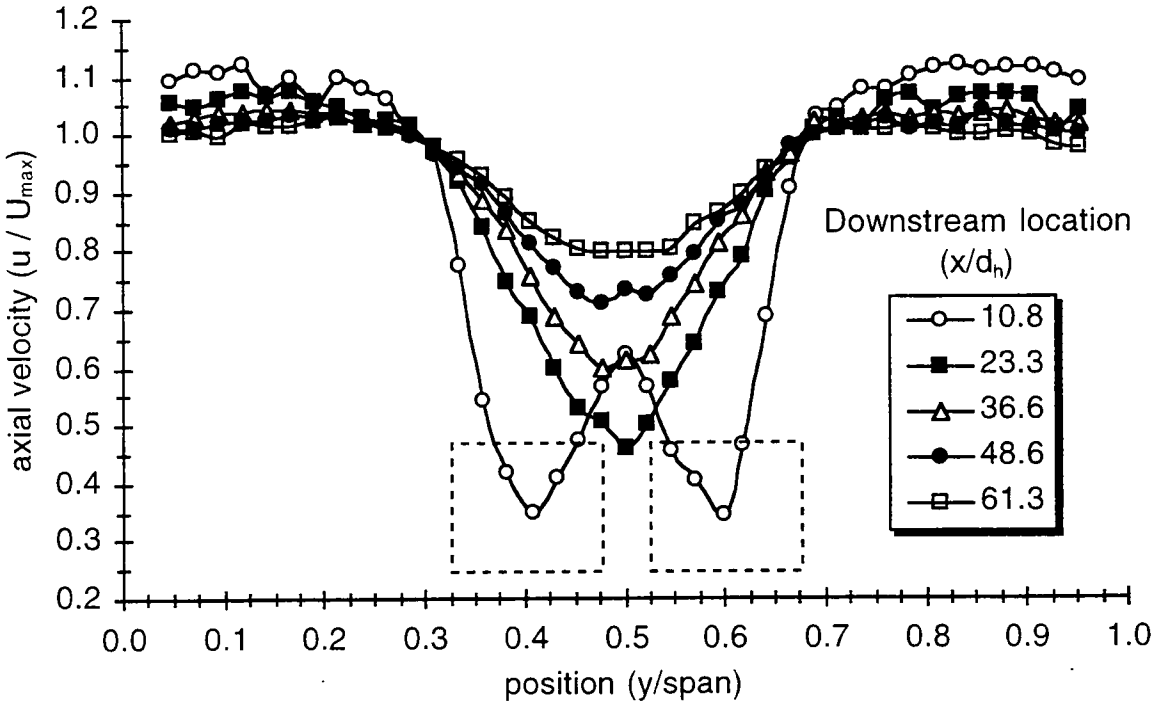


Figure 34. Axial velocity profiles downstream of dual 15% blockages positioned with a 5% separation gap

first measurement window at 10.8 d_h. From the curve fit of the minimum velocities, the reattachment length was approximated at 10 d_h (25 mm) or 1.98 blockage widths downstream. The resulting average mid-gap velocity of 17.7 m/s reflects a 4.8% overall velocity defect. The local minimum velocities of 6.5 and 6.4 m/s, however, 10.8 d_h directly downstream of the blockages correspond to 65 and 66% local velocity defects respectively. By the fifth measurement window at 61.3 d_h, the mid-span velocity has recovered to 80% of the unblocked velocity.

The 15-20-15 blockage is a pair of 15% square blockages positioned in the center of the channel with a 20% separation gap between. As can be seen

in Fig. 35, reattachment for a 15-20-15 inlet blockage occurs somewhere before the first measurement window at 10.8 d_h. From the curve fit of the minimum velocities, the reattachment length was approximated at 10 d_h (25 mm) or 1.98 blockage widths downstream. The resulting average mid-gap velocity of 17.7 m/s reflects a 4.8% overall velocity defect. The local minimum velocities of 5.3 and 5.4 m/s, however, 10.8 d_h directly downstream of the blockages correspond to 72 and 71% local velocity defects respectively. By the fifth measurement window at 61.3 d_h, the minimum velocities have recovered to 91 and 90% of the unblocked velocity.

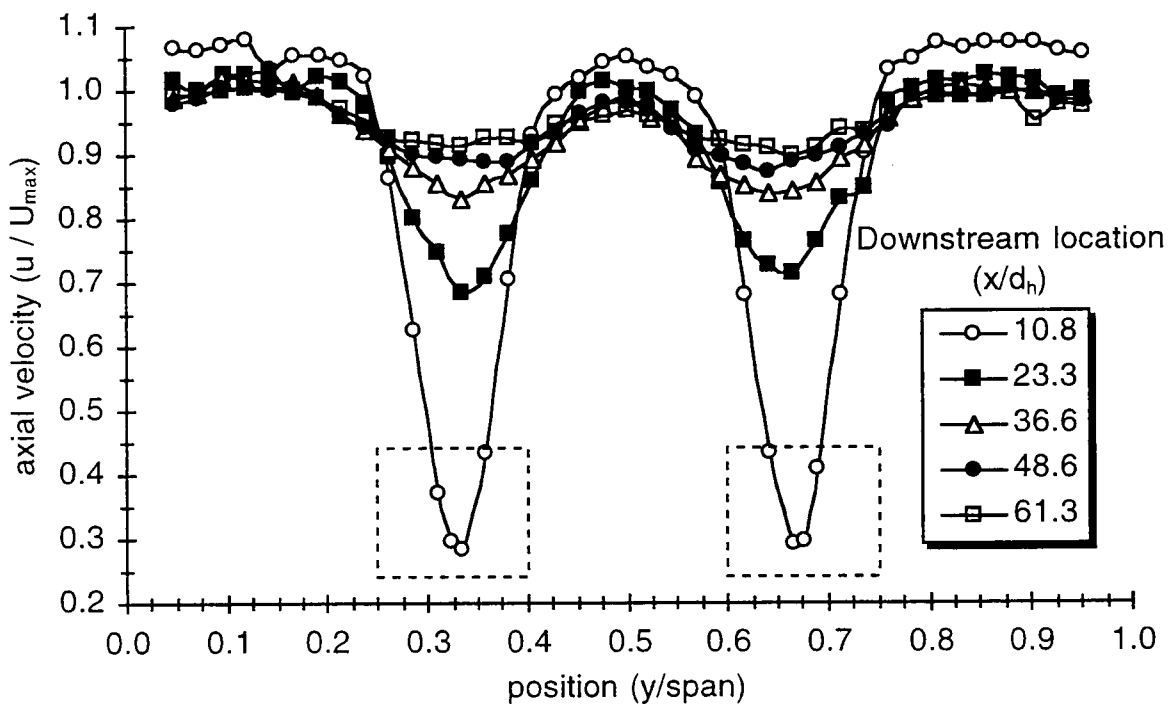


Figure 35. Axial velocity profiles downstream of dual 15% blockages positioned with a 20% separation gap

The most logical blockage configurations to compare these dual 15% blockages are the 30 and 35% center blockages. As can be seen in Fig. 34, the velocity profiles 10.8 d_h downstream of the 15-5-15 blockage appear much as one would expect - two distinct velocity minimums. Subsequent locations further downstream, however, resemble a single center blockage with one velocity minimum. Apparently the flow through the 5% separation gap is not sufficient to maintain the two innermost recirculation vortices. By the second observation point at 23.3 d_h downstream, the innermost recirculation vortices have decayed and only the outer vortices remain. Assuming that this separation gap was not sufficient, it would be expected that the dual 15% blockage with a 5% gap would have similar flow patterns to a 35% blockage. As can be see in Fig. 36, however, the axial velocity profile 61.3 d_h downstream of the 15-5-15 blockage has a much lower velocity minimum than does the 35% center. Further comparisons show that the wake is even slightly longer than a 40% even though the average axial velocity for the 15-5-15 is exactly the same as a 30% center.

One plausible explanation for this behavior is the different pressure gradient downstream of the dual blockage. Whereas a standard 30% blockage has a low pressure region directly behind the blockage, the flow through the 5% gap in the 15-5-15 blockage results in a higher pressure at the mid-gap. There are still two smaller lower pressure regions but these are located some distance from the mid-gap behind their respective blockages. This overall decreased

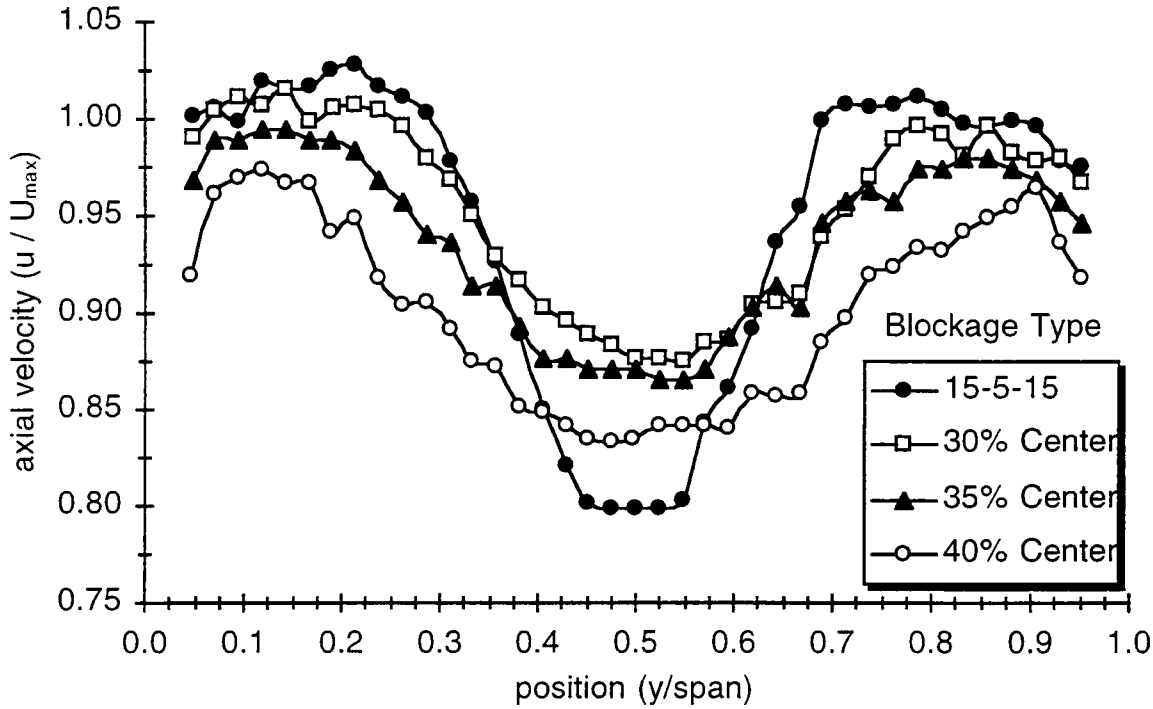


Figure 36. Comparison of axial velocity profiles 61.3 d_h downstream of 15-5-15 and 30, 35, and 40% standard blockages

pressure gradient downstream of the blockage coupled with the spatial distribution of the two pressure minimums may act together to prolong the recovery process further downstream.

5. INTERPRETATIONS AND CORRELATIONS

Based on the LDV results discussed in the previous sections, there are several interpretations and correlations that can be drawn. Initially the standard blockages are analyzed and correlations established to predict both reattachment length as well as average mid-gap velocity. Once these trends are determined, the non-standard blockage shapes are analyzed and the correlations are further modified to predict the effects of shape on the resulting reattachment length and average mid-gap velocity. Due to the limited scope of the positions analyzed, it would be premature to attempt a correlation modification to predict the effects of position.

5.1 STANDARD CORRELATIONS

Figures 37 and 38 show how the reattachment length varies with the width of the blockage. The width of the blockage is non-dimensionalized by the span of the channel. In Fig. 37, the reattachment length is non-dimensionalized by the gap height of 1.27 mm and shows a logical trend of longer reattachment lengths with wider blockages. In Fig. 38, the reattachment length is non-dimensionalized by the width of the blockage and shows quite a different trend. At first glance, the trend would seem to imply that the reattachment length shortens with wider blockages. The graph, however, shows that the effect of blockage width upon reattachment length diminishes as

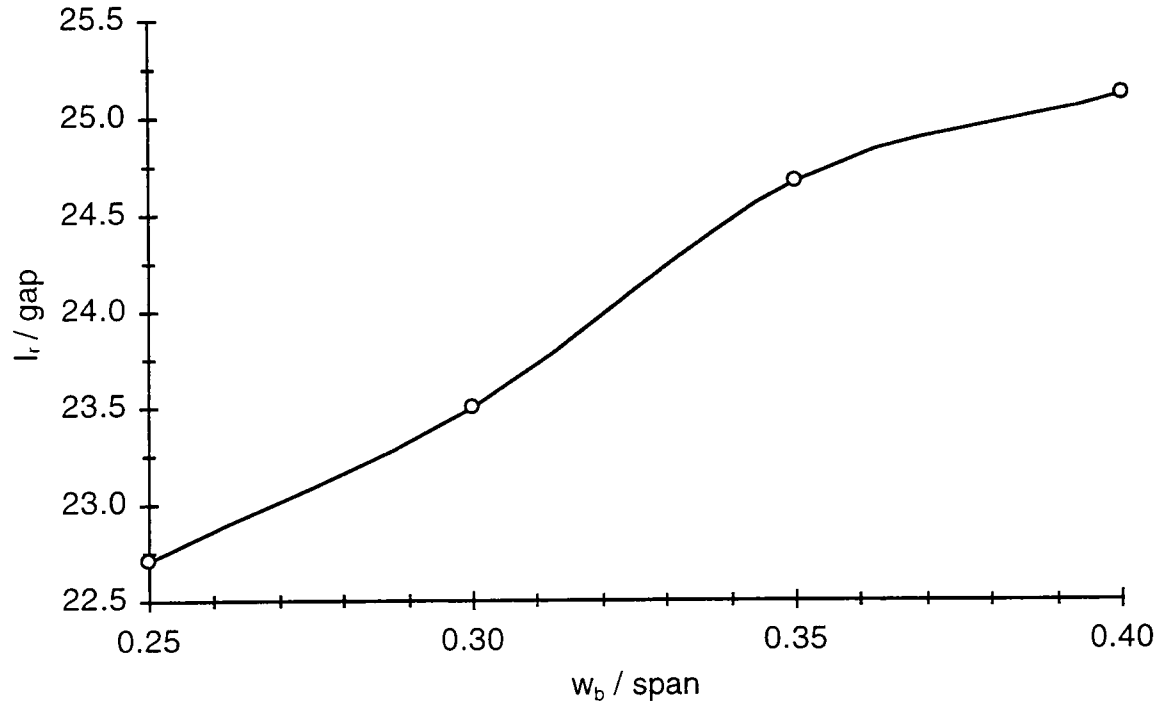


Figure 37. Gapwise non-dimensionalized reattachment length dependence on blockage size

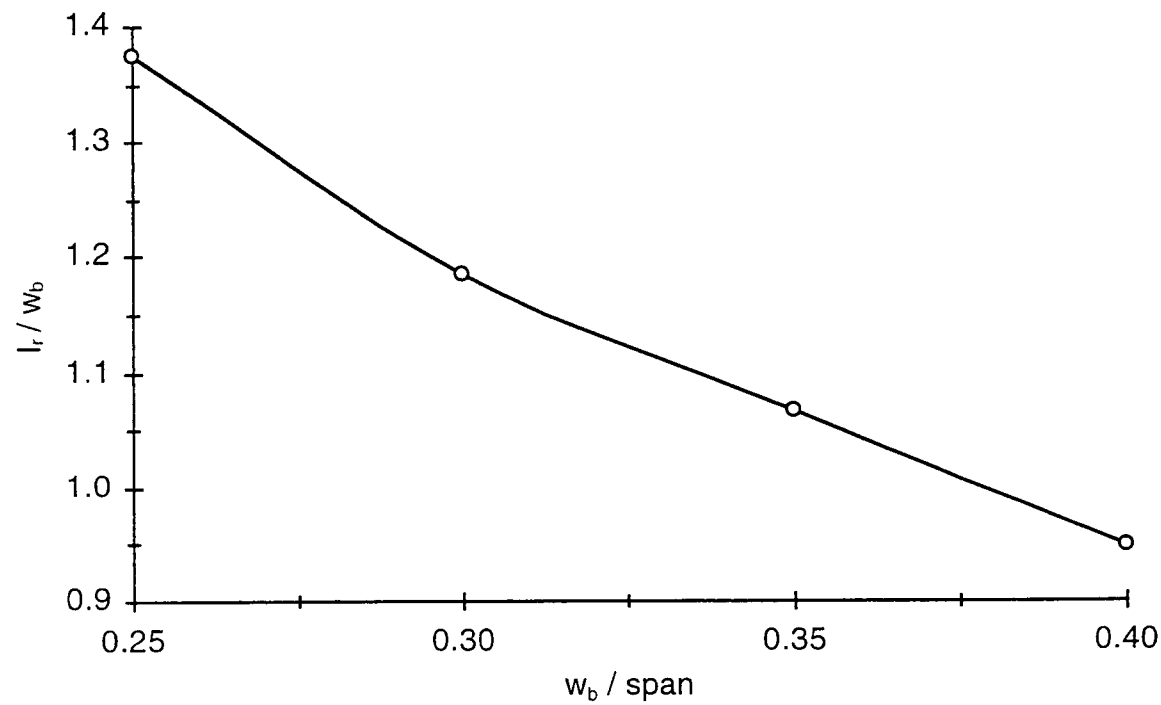


Figure 38. Blockage width non-dimensionalized reattachment length dependence on blockage size

the blockage width grows. Hence reattachment length does not increase as rapidly as blockage width, giving the graph a negative slope. It is important to remember, however, that all of these cases are for the same pressure drop, not the same flow. Although this choice of non-dimensionalization proved interesting, it was not selected because of the variability of the blockage widths. Since the gap height was held constant for all of the experiments, it was selected for use in non-dimensionalizing the reattachment length.

Before proceeding with an independent correlation, the reattachment length was plotted against average mid-gap velocity. As can be seen in Fig. 39, the reattachment length correlates well with average mid-gap velocity for the standard blockages as well as for the non-standard single blockages. This alleviates the need for the development of two independent correlations. Once a satisfactory correlation is developed for predicting the average mid-gap velocity, the reattachment length can then be estimated from a curve-fit of the data in Fig. 39. The data was curve-fit using an exponential function of the following form resulting in an R^2 of 0.98.

$$\frac{l_r}{gap} = a_6\left(1 - e^{-b_6\left(1-\frac{\bar{u}}{U_{max}}\right)}\right) \tag{6}$$

where,

$a_6 =$ 25.3920

$b_6 =$ 56.1300

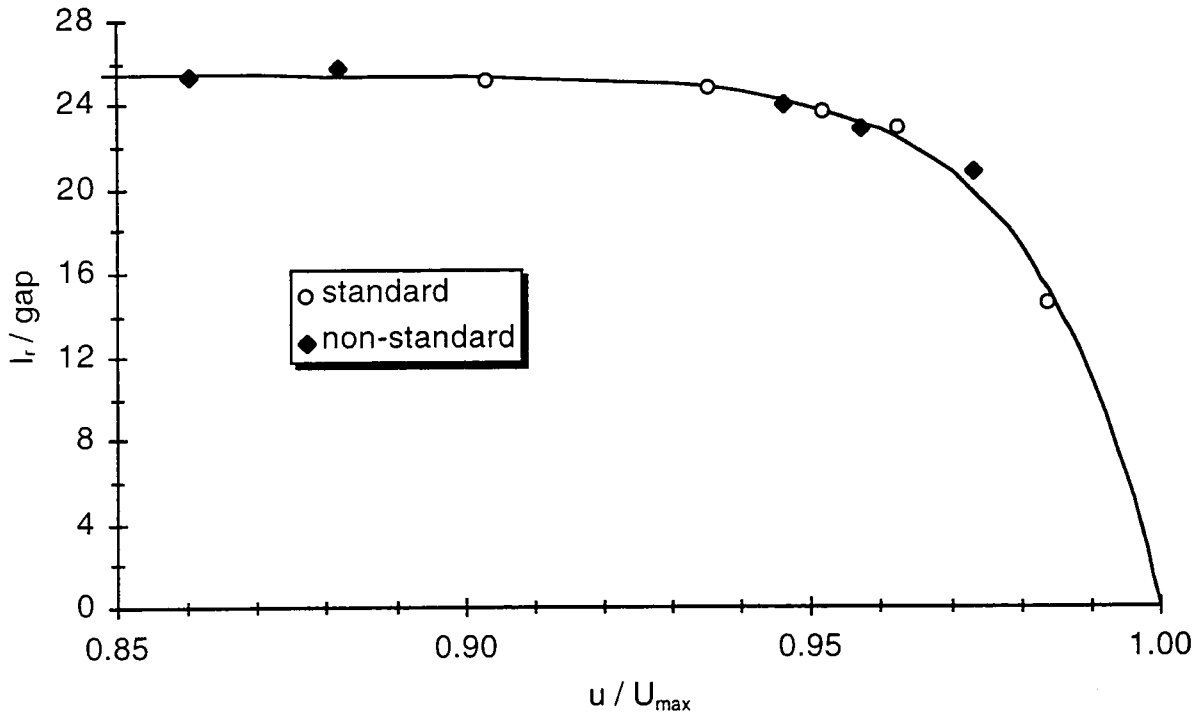


Figure 39. Exponential curve-fit of gapwise non-dimensionalized reattachment length dependence on average mid-gap velocity

This form of this function was selected so as to ensure satisfaction of the boundary condition of l_r/gap = 0 when $u/U_{max} = 1$.

Figures 40 and 41 show how the average mid-gap velocity varies with the width of the blockage. The average velocity is non-dimensionalized by the maximum unblocked velocity at the mid-gap. In Fig. 40, the blockage width is non-dimensionalized by the span of the channel and shows a logical trend of decreased average mid-gap velocity with wider blockages. The effective hydraulic diameter is computed by dividing the hydraulic diameter of the partially blocked channel by the hydraulic diameter of an unblocked channel. In Fig. 41, the average velocity is compared to the resulting effective hydraulic

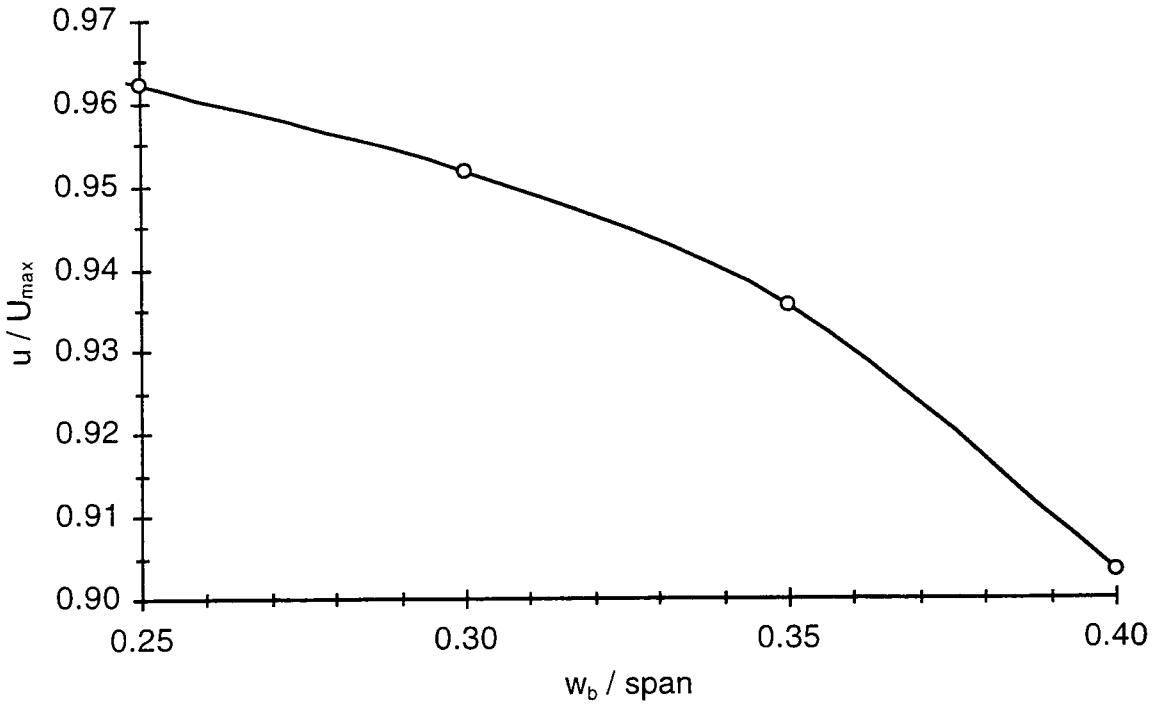


Figure 40. Unblocked velocity non-dimensionalized average velocity dependence on blockage size

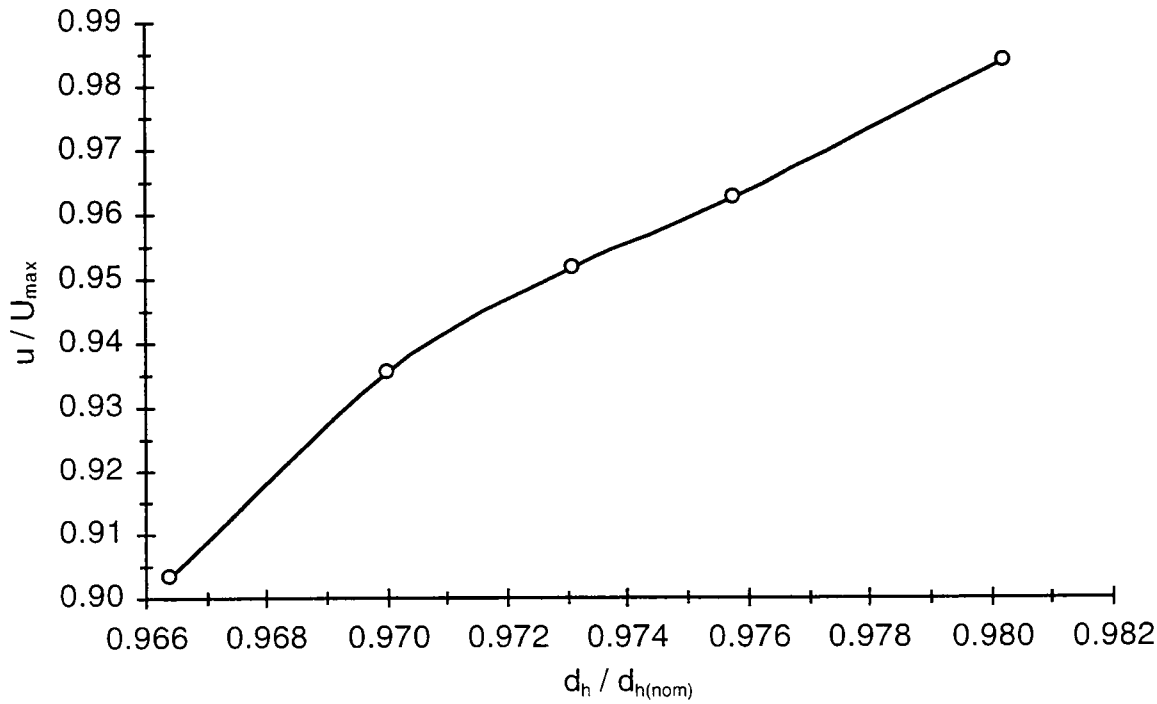


Figure 41. Unblocked velocity non-dimensionalized average velocity dependence on effective hydraulic diameter

diameters and shows quite a different trend. This is due to the fact that the effective hydraulic diameter decreases with increasing blockage width.

In the interest of casting the correlation in a form that could easily accommodate extension to other channel geometry, the effective hydraulic diameter dependence was selected. Initially a second-order polynomial was used to fit the data and resulted in an R^2 of 0.991 but did not lend itself to a very accurate extrapolation. The data was re-fit using the following exponential function and resulted in a slightly higher R^2 of 0.993.

$$\frac{\bar{u}}{U_{max}} = 1 - e^{-a_7\left(\frac{d_h}{d_{h(nom)}}\right)^{b_7}} \qquad (7)$$

where,

a_7 = 8.47882

b_7 = 37.6074

As can be seen by a comparison of the two curve fits in Fig. 42, the second-order polynomial (dashed line) would over-predict mid-gap velocities for small blockages. The exponential curve fit (solid line), however, provides a more accurate representation of the expected flow velocities in the extrapolated region.

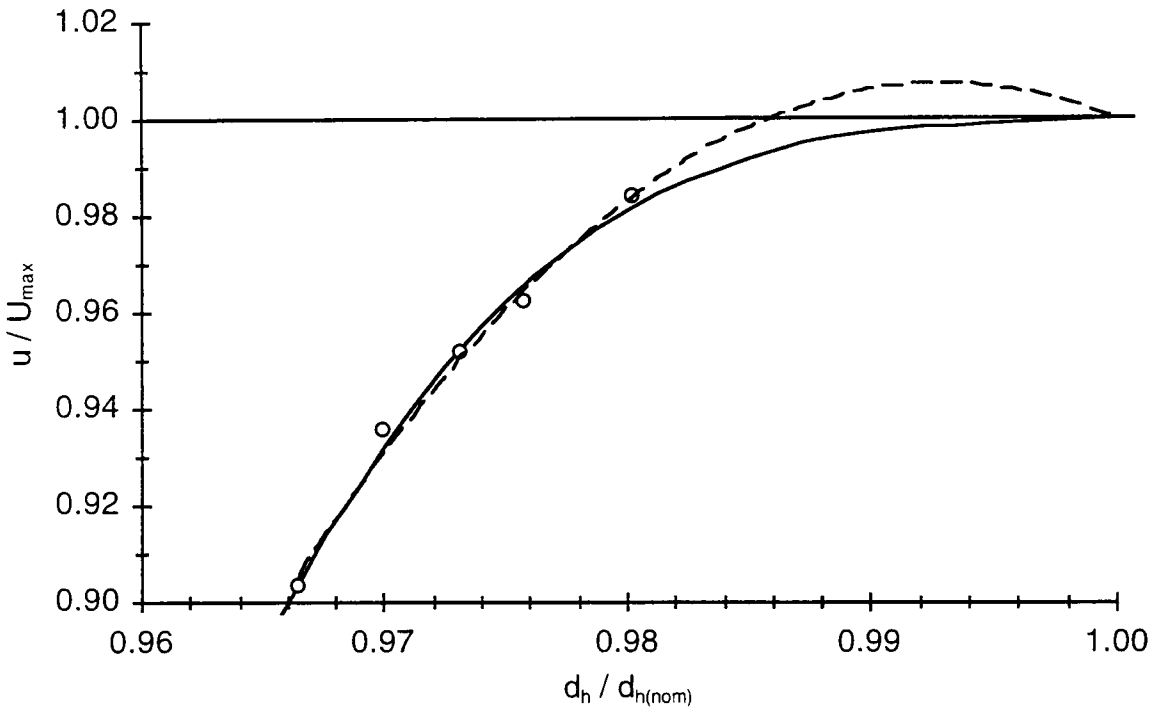


Figure 42. Curve-fit comparison for unblocked velocity non-dimensionalized average velocity dependence on effective hydraulic diameter

5.2 SHAPE ADJUSTMENT

Once a satisfactory correlation was in place for the standard blockages, a means of adjusting these predictions to reflect the effects of shape was required. The resulting correlation would be used to adjust the predicted average velocity to compensate for the effect of the angle of a sloped blockage.

As discussed in section 4.2, a series of blockages with various shapes were tested. These shapes were then compared to their equivalent square standard blockages to account for any impacts that shape may have on the

resulting flow. In the course of this work, it was discovered that the diverging orientation had a greater impact than the complementary converging orientation. It was also observed that these factors for the 20/40 trapezoid blockage were larger than for the 25% triangular blockage. If this impact is due in part to the resulting directional momentum from an angled blockage, one would logically expect it to depend directly on the local flow velocity beside the blockage, which is in turn directly proportional to the blockage size. Thus one can attempt to correlate the velocity adjustment to the size of the blockage.

For simplicity, a linear relationship as shown in Eq. (8) is applied to account for the effect of angle.

$$\left(\frac{\bar{u}}{U_{max}}\right)_{adjusted} = \left(\frac{\bar{u}}{U_{max}}\right)_{std} + \left[\frac{\delta\left(\frac{\bar{u}}{U_{max}}\right)}{\theta}\right]\theta \qquad (8)$$

where,

$\left(\frac{\bar{u}}{U_{max}}\right)_{std}$ = predicted average velocity for standard blockage

$\frac{\delta\left(\frac{\bar{u}}{U_{max}}\right)}{\theta}$ = adjustment in average velocity per angle

The slope of this line, however, has been fit to an exponential (Fig. 43) to account for a dependence upon local flow velocity in the jets on either side of

the blockage. The following exponential function is used to select the adjustment/angle slope for a given blockage size.

$$\frac{\delta\left(\frac{\bar{u}}{U_{max}}\right)}{\theta} = a_9\left(1 - e^{-b_9\left(\frac{w_b}{span}\right)}\right) \qquad (9)$$

where for converging,

a_9 = -5.40057E-05

b_9 = -6.73976

for diverging,

a_9 = 6.66297E-04

b_9 = -2.55473

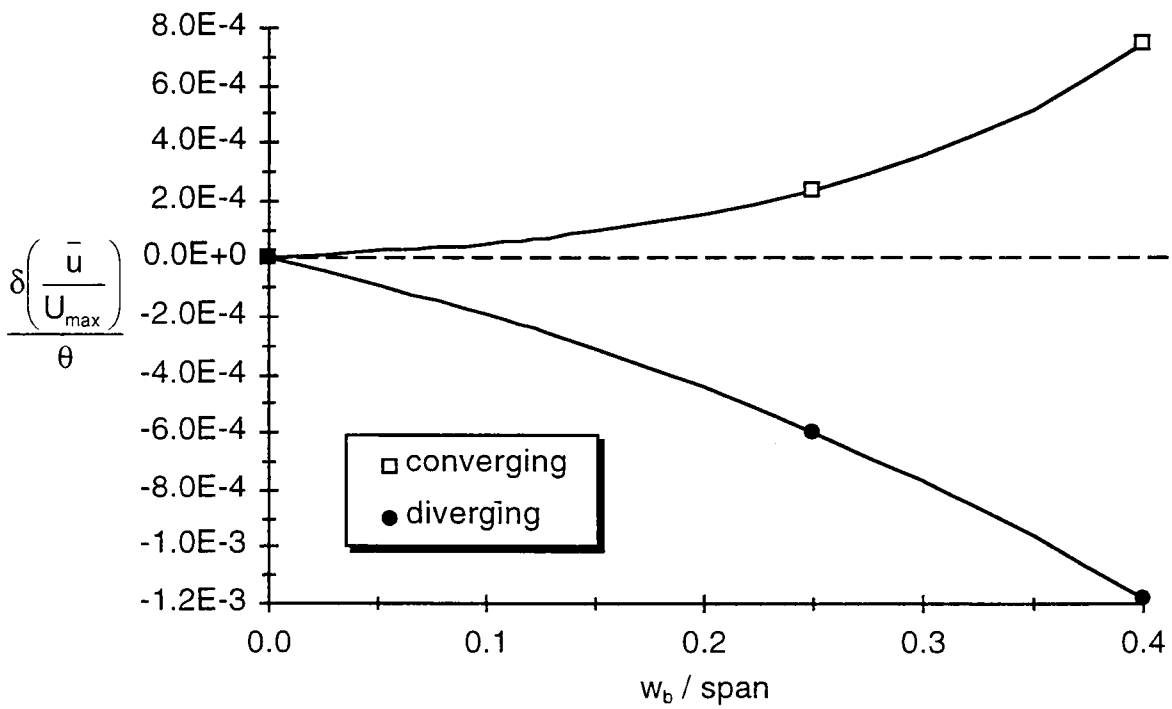


Figure 43. Curve-fits for the adjustment/angle slope as a function of blockage size

5.3 REYNOLDS NUMBER ADJUSTMENT

All of the previous correlations are based on experimental data taken for a 0.7 MPa pressure drop. Thus they are valid for only one unblocked Reynolds number. In previous work, data were taken for standard blockages over a range of pressure drops (Stovall et al., 1995). Based upon data taken for a 35% blockage at pressure drops of 0.33, 1.29, and 1.46 MPa, some dependence upon Reynolds number can be taken into account.

The square symbols in Fig. 44, are the average mid-gap velocities for a 35% blockage at 0.33, 1.29, and 1.46 MPa pressure drops. These pressure drops correspond to unblocked Reynolds numbers of 37,033, 73,230, and 77,540. One approach to account for the Reynolds number dependence is to simply shift the curve up or down to match the shift in the average velocity. The problem with this approach is that an upward shift would result in predictions of average velocities higher than the unblocked for small blockages while a shift downward would result in predictions of less than the unblocked velocity for totally unblocked channels. The approach taken, however, was fix the a_7 correlation coefficient while adjusting the b_7 correlation coefficient in Eq. (7) to alter the shape of the curve. As can be seen in Fig. 44, this maintains a very logical extrapolation to the smaller blockages.

Once this approach was adopted, yet another correlation was necessary (Fig. 45) to determine the correct b_7 correlation coefficient for a given unblocked Reynolds number (Re_{nom}).

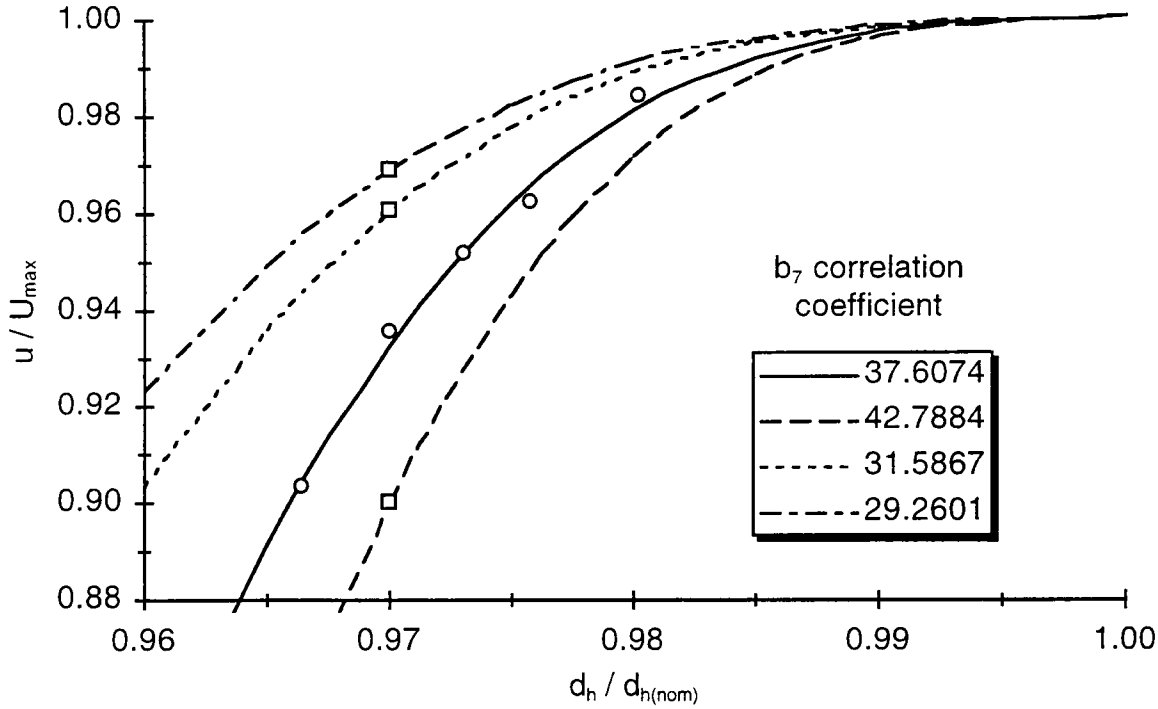


Figure 44. Unblocked velocity non-dimensionalized average velocity dependence on effective hydraulic diameter and Reynolds number

$$b_7 = c_{10}\,Re_{nom}^2 + d_{10} \qquad (10)$$

where,

c_{10} = -2.86151E-09

d_{10} = 46.6471

With this simple function in place, the average mid-gap velocity correlation can now be sensitized to Reynolds number variation by replacing the b_7 constant in Eq. (7) with the relationship found in Eq. (10).

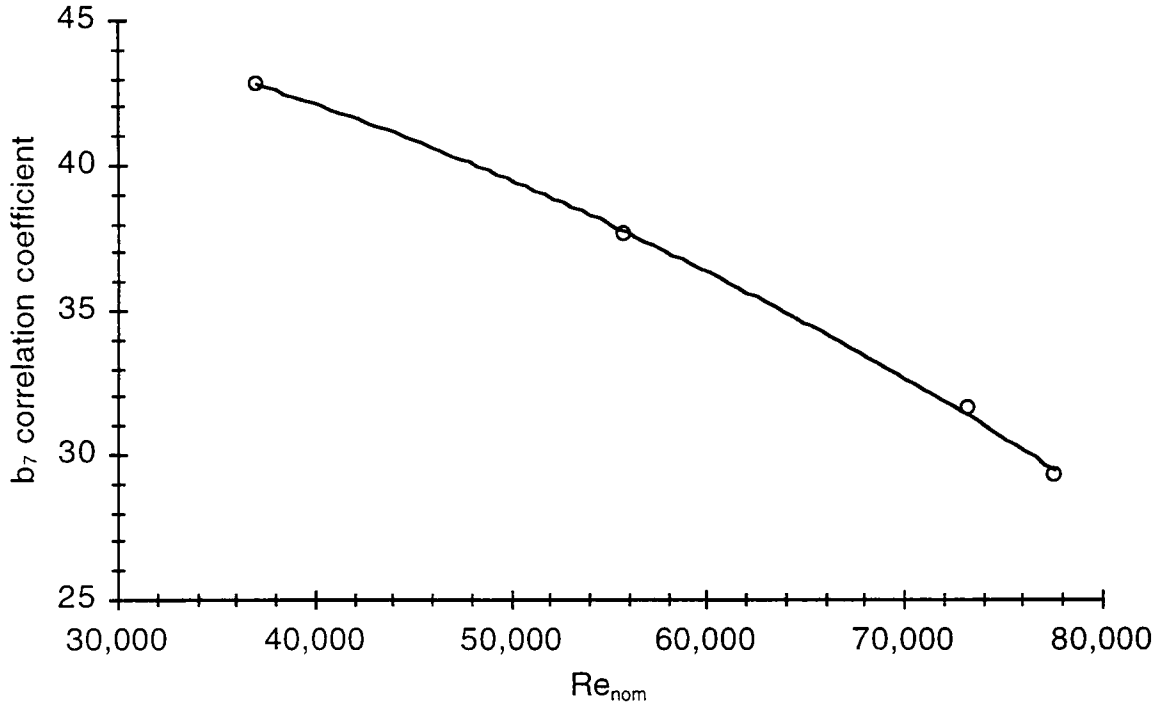


Figure 45. Required correlation coefficient to account for average mid-gap velocity dependence upon Reynolds number

With a Reynolds number dependence factored in for average velocity, the only remaining correlation requiring Reynolds number modification is the reattachment length as a function of average velocity. Over the range of Reynolds numbers for the 35% blockage, the reattachment length varied by only 7%. In Figs. 39 and 46, the reattachment length is plotted against the average velocity resulting from various different standard and non-standard blockages for 0.7 MPa (Re_{nom} = 55,680). As can be seen in these figures, the reattachment length becomes rather insensitive to blockage size for the lower average velocities resulting from larger blockages. This near insensitivity to blockage size was also observed by Sparrow and Cur (1983), who noted that

the sensitivity diminished with Reynolds number. It is important to note, however, that the blockages analyzed by Sparrow and Cur were limited to 25% and 50%. Since the reattachment length must be 0 for $u/U_{max} = 1$ and can not undergo a step change from 0 to a length where it is relatively insensitive to blockage size, there must be some range in which blockage size does indeed influence the length of reattachment. This region where the reattachment length grows quickly with blockage size, however, is probably compressed with increasing Reynolds number. This increases the range of blockage sizes over which the reattachment length appears relatively insensitive. In light of this, the most appropriate adjustment to the reattachment length correlation would be in expanding this region for lower Reynolds numbers and compressing it for higher ones.

The triangular symbols in Fig. 46, are the reattachment lengths for a 35% blockage at 0.33, 1.29, and 1.46 MPa pressure drops. These pressure drops correspond to Reynolds numbers of 37,033, 73,230, and 77,540. A similar approach to that of the average velocity correction was used to account for Reynolds number dependence. While holding the a_6 coefficient constant, the b_6 correlation coefficient in Eq. (6) was adjusted to alter the shape of the curve so as to expand or compress the region where the reattachment length grows quickly with blockage size.

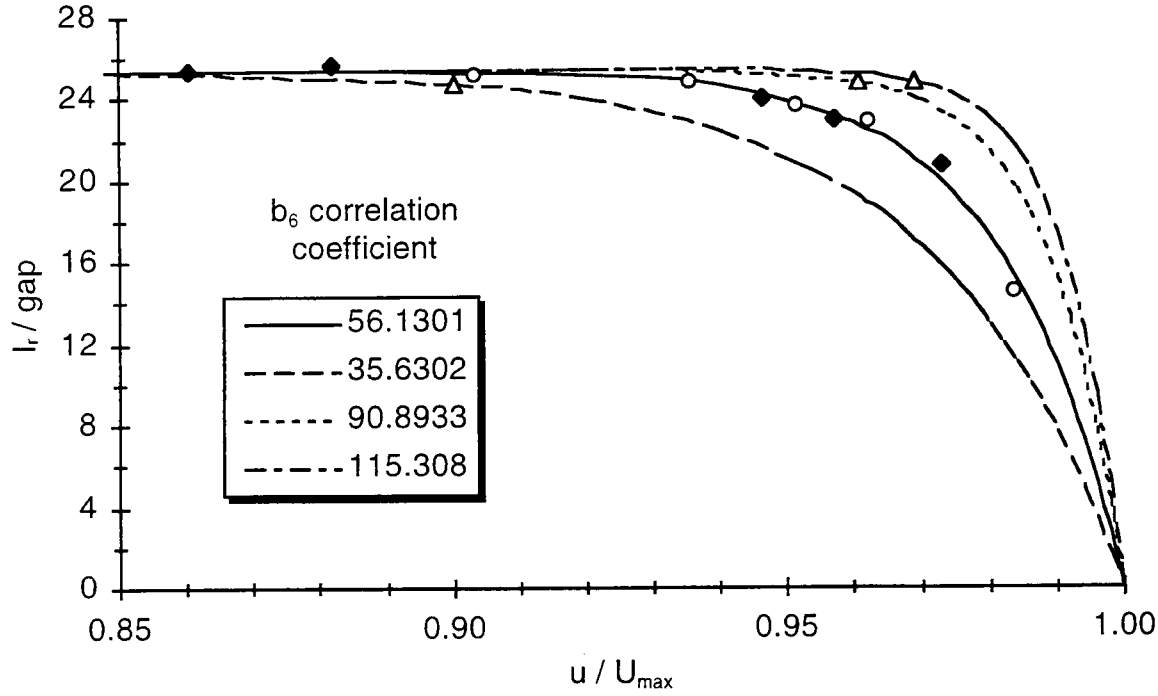


Figure 46. Gapwise non-dimensionalized reattachment length dependence on average mid-gap velocity and Reynolds number

As before in the average velocity correction, another correlation is necessary (Fig. 47) to determine the correct b_6 correlation coefficient for a given unblocked Reynolds number.

$$b_6 = c_{11} + d_{11} Re_{nom}^{e_{11}} \qquad (11)$$

where,

c_{11} = 33.4855

d_{11} = 2.10563E-19

e_{11} = 4.20770

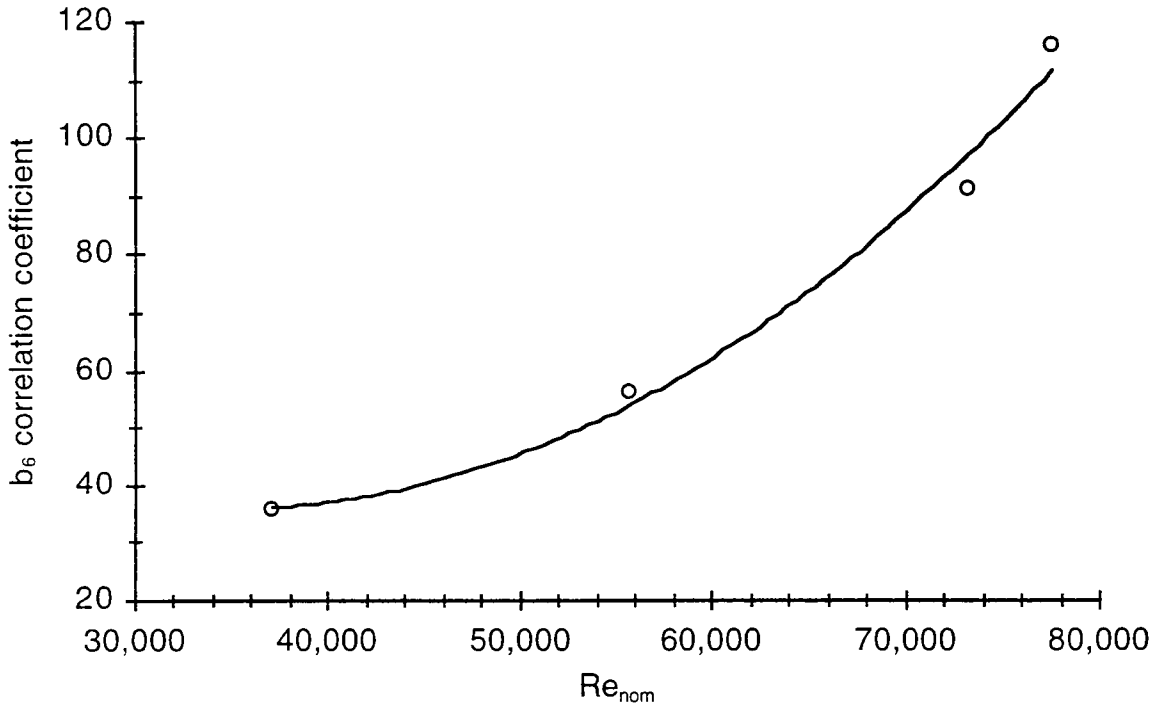


Figure 47. Required correlation coefficient to account for reattachment length dependence upon Reynolds number

With this simple function in place, the reattachment length correlation can now be sensitized to Reynolds number variation by replacing the b_6 constant in Eq. (6) with the relationship found in Eq. (11).

With these correlations in place, it is important to note that although they are cast in a form that can be easily applied to other channel geometries, this is not recommended. The correlations are primarily meant for use in interpolating between the measured data and for extrapolation down to smaller blockages. They are a purely empirical means for interpreting the data, and there is no basis for their use in extrapolating to larger blockages. Such correlations,

however, can be useful in the Probabilistic Risk Assessment (PRA) and Safety Analysis Reports (SAR) for plate-fuel type reactors.

6. CFD MODELING ISSUES

When modeling any fluid dynamics problem, there are several issues that one must address that directly impact the quality of the solution obtained. An adequate grid is mandatory for any CFD model, but this requirement must be carefully balanced with other factors including CPU resources and the accuracy desired. As compared to laminar flow, turbulent flow simulations are more susceptible to grid quality. In wall-bounded flows, this problem is further complicated by the selection of a near-wall treatment which will govern the mesh required in this region.

The CFD code used for this work is *Fluent*, which is based on a control-volume finite volume method. The governing equations, mathematical formulations of turbulence models, and numerical algorithms for the *Fluent* code are detailed in the User's guide (Fluent, Inc., 1996). There are three turbulence models available in the code: k-ε, RNG k-ε, and the Reynolds Stress Model (RSM). The k-ε model was proposed by Jones and Launder (1972) and has been widely used for more than 20 years. Both k-ε and RNG k-ε are two-equation turbulence models based on an isotropic eddy-viscosity concept. There are, however, some major differences between the two models. The RNG model was derived using a more rigorous statistical technique and its constants are derived by theory as opposed to empiricism (Fluent, Inc., 1993).

RSM, on the other hand, is not based on an isotropic eddy-viscosity concept but rather involves the calculation of the individual Reynolds stresses through the solution of the transport equations.

Since these models are primarily valid for the turbulent core, near-wall treatments are required to determine the flow adequately in the viscous sublayer and buffer layer. One such treatment is the use of semi-empirical formulas, or wall functions, to "bridge" the viscosity-affected region between the wall and the fully-turbulent core. Standard and nonequilibrium are the two wall function options offered by the *Fluent* CFD code. Since nonequilibrium wall functions are sensitized to pressure gradient effects, they are recommended for use in flows involving separation and reattachment. Another more complicated method involves the resolution of the near-wall region all the way to the wall. While the wall-function approach is more computationally economic and reasonably accurate, there are some known limitations such as modeling flow through a small gap.

All of these CFD modeling issues were closely examined by developing a series of CFD simulations depicting flow downstream of a square 30% standard blockage. In these CFD models, the boundary conditions, physical properties, pressure-velocity coupling methods, and convergence criteria are consistent. The inlet boundary condition used is the average bulk fluid velocity determined by the LDV measurements and flow meter. Due to the large local gradients in pressure, cell pressures are interpolated using PRESTO (PREssure

Staggering Option). The SIMPLE (Semi-Implicit Method for Pressure-Linked Equations) algorithm is used to enforce mass conservation and obtain the pressure field. The criterion used for convergence was the reduction of the scaled residuals to some value less than 0.001. Since the blockage configuration examined in these simulations is located at the center of the channel, two planes of symmetry were used in the mesh generation and are depicted in Fig. 48.

These CFD simulations can be classified by the near-wall treatment used: wall functions or boundary layer resolution. In each section, the issues of grid, turbulence model and discretization are discussed.

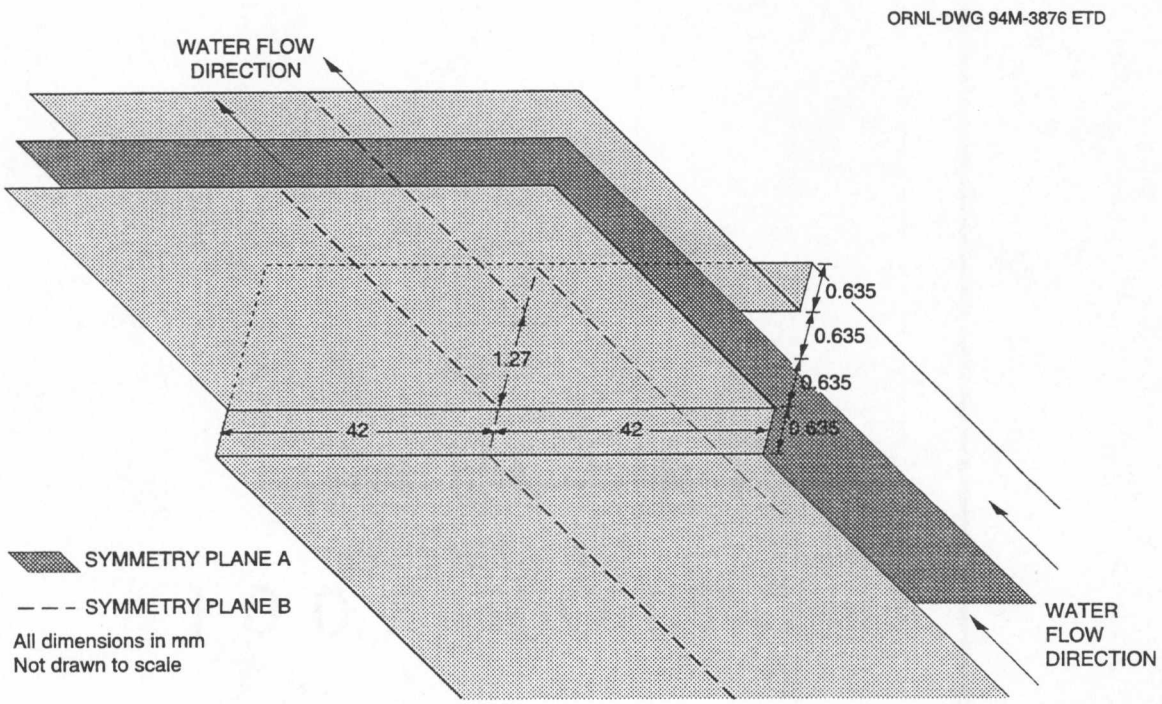


Figure 48. CFD model geometry at channel inlet

6.1 WALL FUNCTIONS

The first mesh generated includes the inlet plenum as well as the channel and is comprised of 129 cells along the axial direction, 22 cells across half the span, and 3 cells across half the gap. The mesh in the gap direction has a uniform distribution.

Using this mesh, two cases were executed using the k-ε model - one with standard wall functions and another with nonequilibrium. Both cases were brought to convergence and then compared. The resulting wake downstream

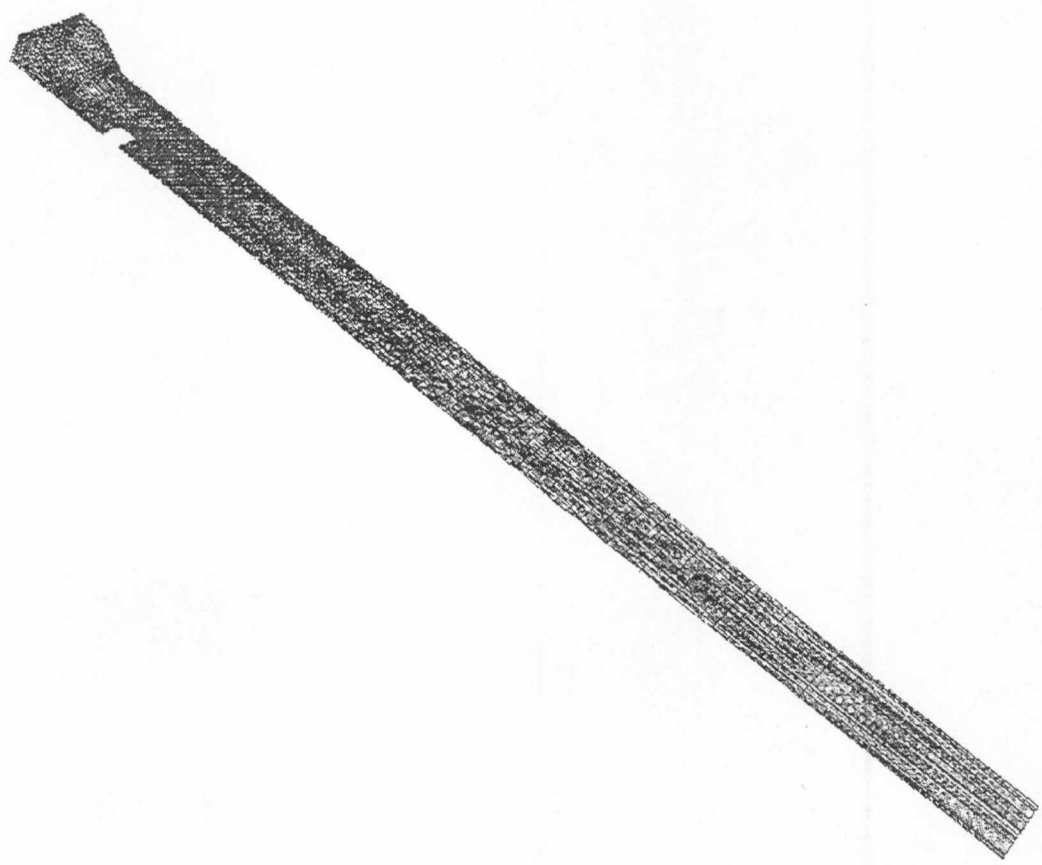


Figure 49. Inlet plenum and channel mesh

of the 30% blockage as well as the high-speed jet along the side can be easily seen in both the velocity contours plot in Fig. 50 and the pathlines in Fig. 51. The flow in these figures is from top to bottom and has been plotted along the plane of symmetry. Reattachment for the standard wall function case was predicted to occur at 37.2 mm downstream from the trailing edge of the blockage.

As can be seen by the pressure contours in Fig. 52, a large pressure drop occurs at the channel entrance, which is defined by an abrupt symmetric change in the channel gap from 2.54 to 1.27 mm. An area of low pressure is

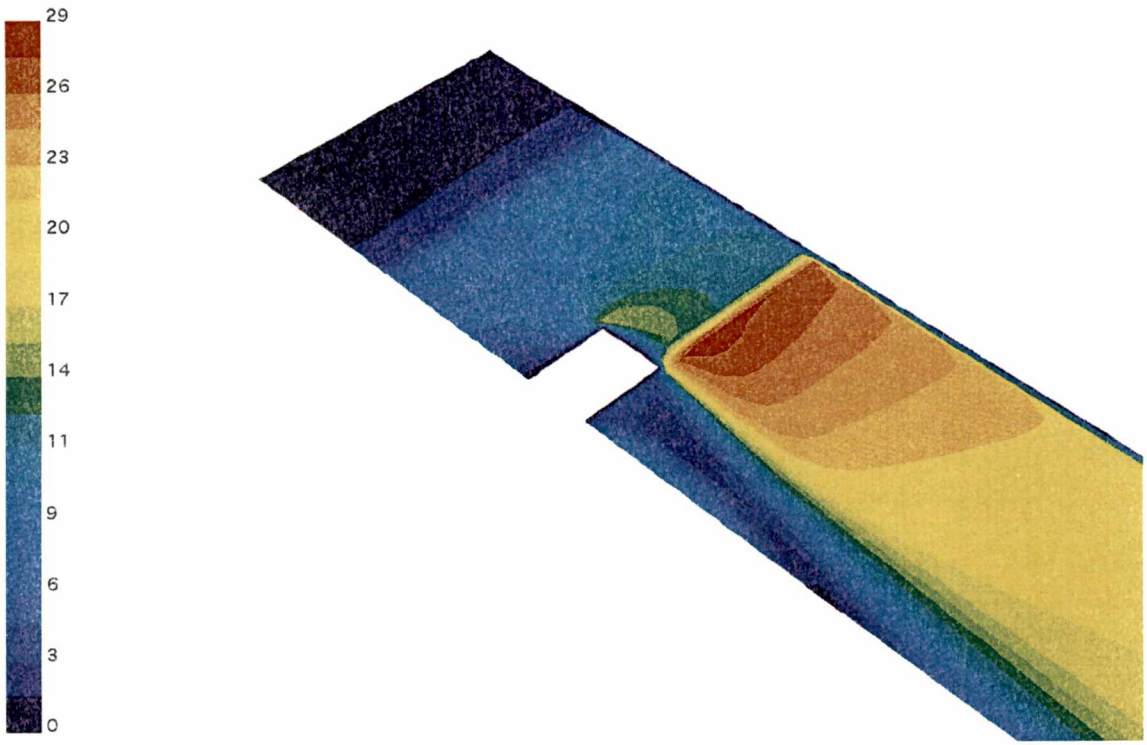


Figure 50. Contours of velocity magnitude for standard k-ε case (m/s)

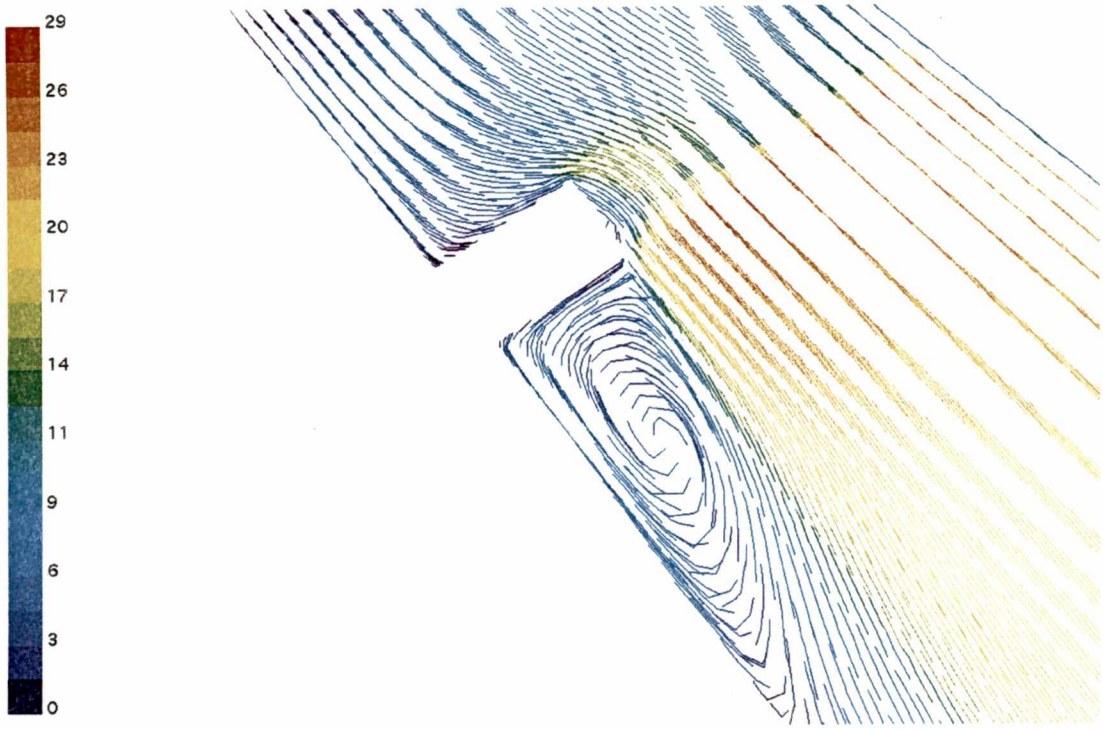


Figure 51. Path lines colored by velocity magnitude for standard k-ε case (m/s)

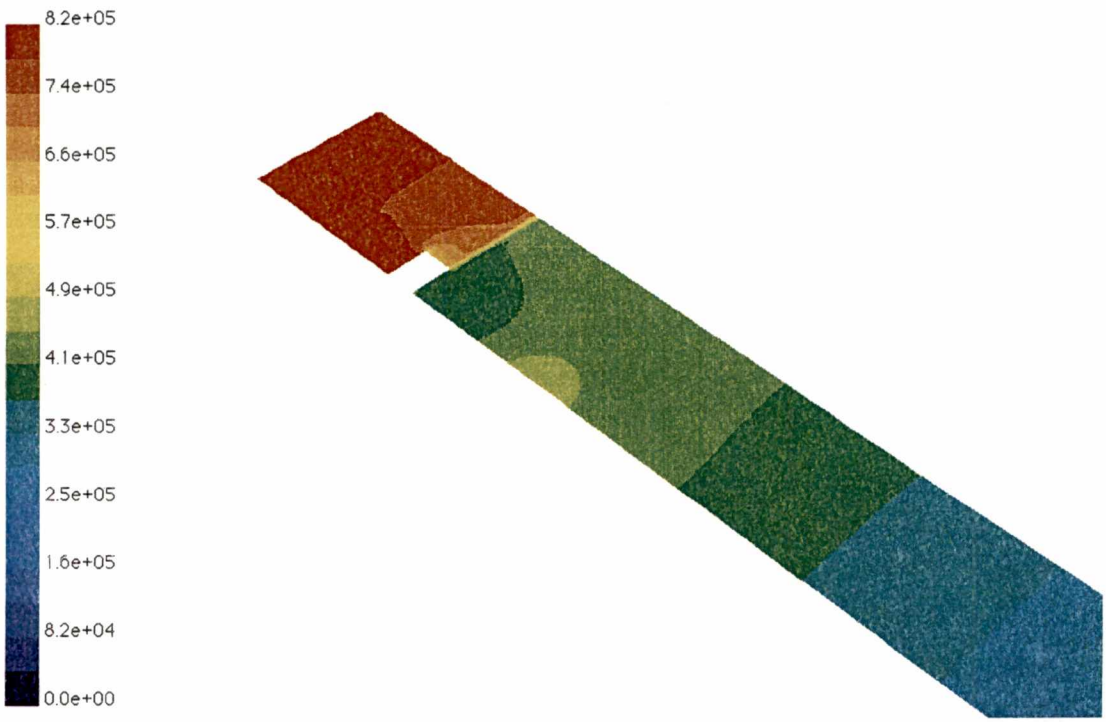


Figure 52. Contours of static pressure for standard k-ε case (Pascal)

also evident directly downstream of the blockage, but the pressure quickly rises and then a normal linear pressure drop resumes as the flow redevelops. This can be more easily seen in Fig. 53 where it is also evident that the pressure minimum does not occur precisely at the downstream face of the blockage but is actually a short distance downstream. The predicted pressure drop for standard wall function case is 0.82 MPa.

As can be seen in Fig. 54, the peak turbulence is positioned along the edge of the recirculation region. The position relative to boundary layer thickness or y^+ is an indication of the adequacy or inadequacy of the near-wall

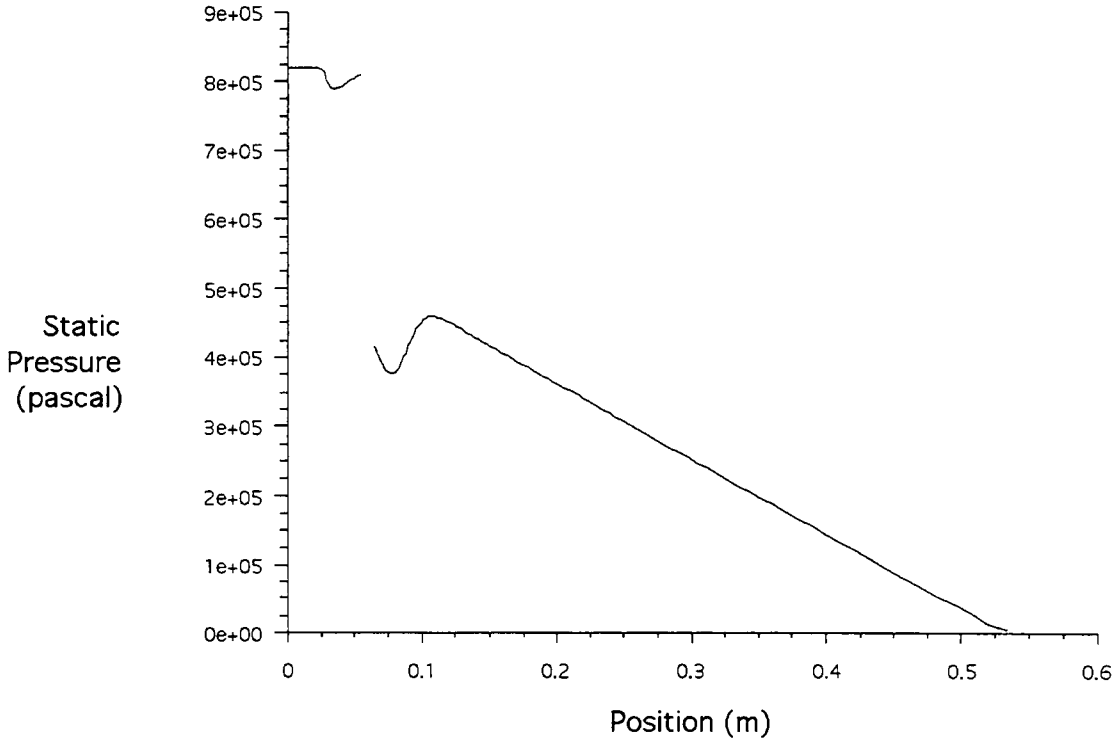


Figure 53. Axial pressure distribution along the centerline on the plane of symmetry for standard k-ε case

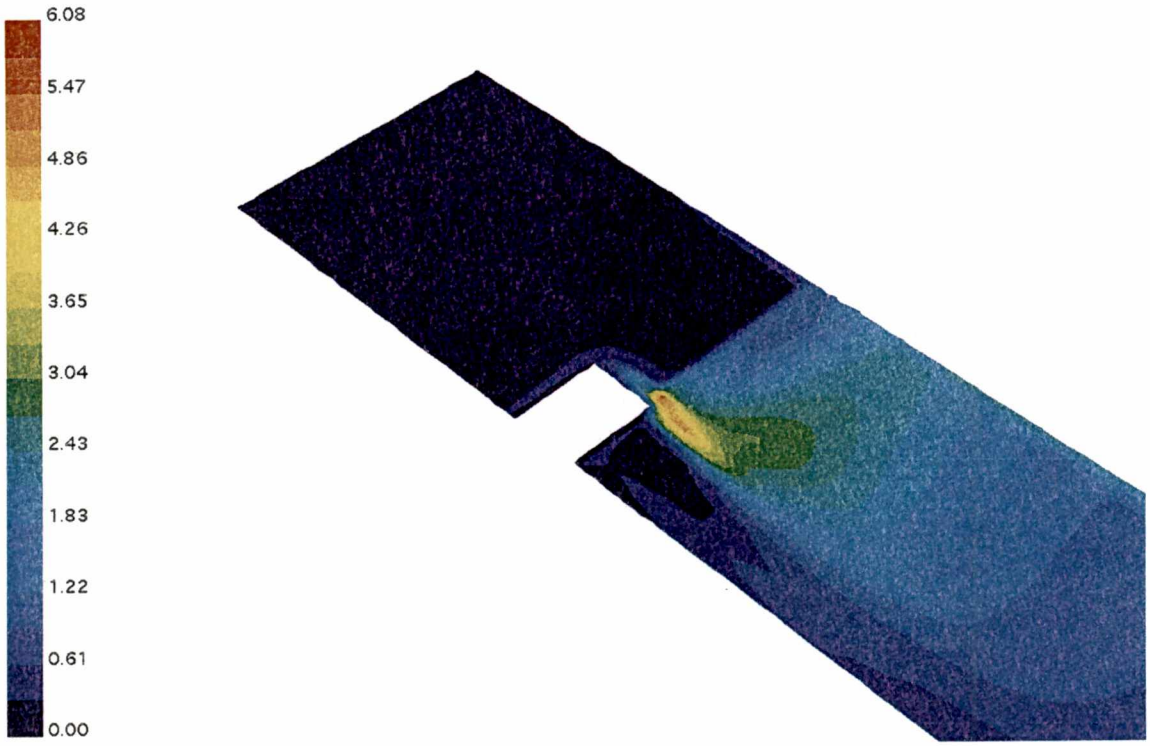


Figure 54. Contours of turbulent kinetic energy for standard k-ε case (m^2/s^2)

mesh. Wall functions are only valid in the log-law region which corresponds to a $y^+ > 30 \sim 60$. Excessively fine meshes near the wall should be avoided as well, since the wall functions are not valid in the viscous sublayer ($y^+ < 11.225$). The average y^+ for the standard wall function case is 125. The contours of surface y^+ in Fig. 55 show an area of high values in the range of 150 that would imply the near-wall mesh in this region is too coarse. In the wake region, however, there are areas where y^+ is less than 30 which would imply that these regions are excessively refined. This is a common problem when using wall functions. Prakash and Zerkle (1995) encountered similar problems in their CFD modeling of a ribbed rectangular duct. They found that even a modest

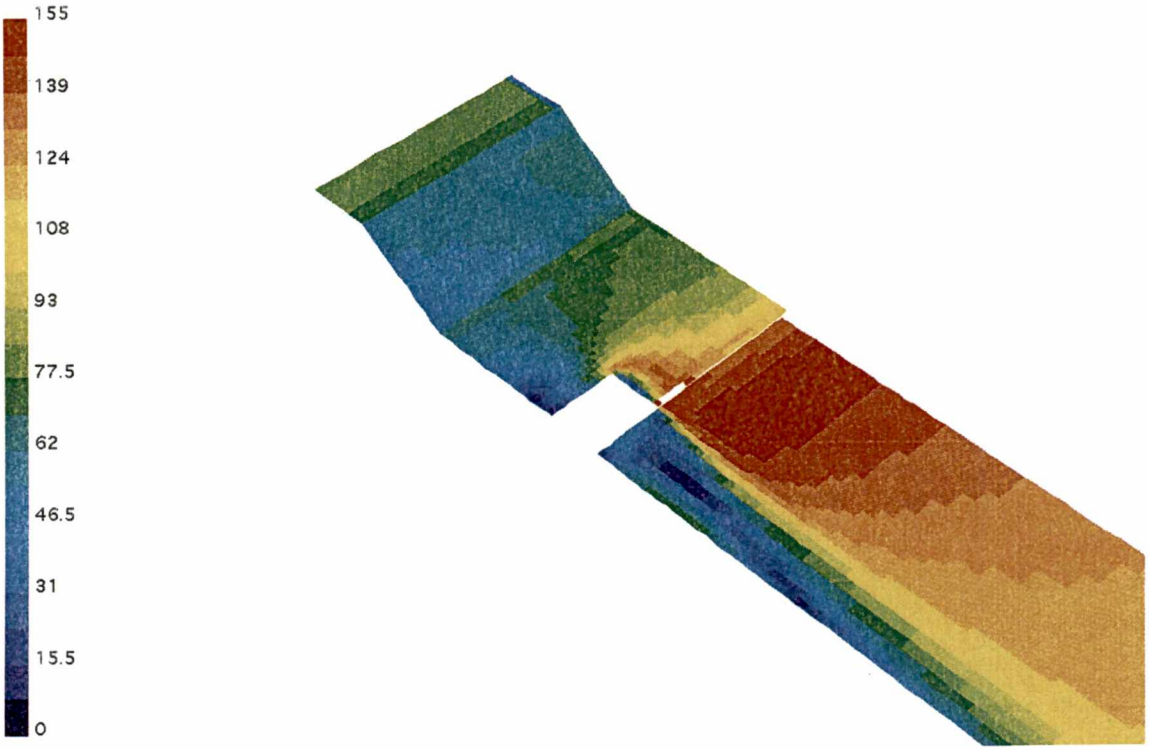


Figure 55. Contours of surface y^+ for standard k-ε case

computational grid lead to nodes being too close to the wall for accurate wall function application.

The nonequilibrium wall function case was also analyzed, but there were no graphically obvious differences in the velocity, pressure, or turbulence fields. The wake for this case was slightly longer, with reattachment predicted to occur 39.1 mm downstream from the blockage. The predicted pressure drop was slightly less at 0.80 MPa. The lower pressure drop and the longer reattachment length are consistent with a lower average effective viscosity.

An additional case was also executed on the same mesh utilizing the RNG k-ε turbulence model with nonequilibrium wall functions. The RNG k-ε

model is known to have less numerical diffusion, which should result in a lower effective viscosity. As expected, this lower numerical diffusion resulted in a longer predicted wake length of 40.7 mm and a corresponding decrease in pressure drop to 0.79 MPa. This shift in the solution, however, was not as pronounced as that observed in comparing the standard and nonequilibrium wall functions. Some observations regarding these cases are summarized in Table 2.

Table 2. CFD cases using wall functions as near-wall treatment on a uniform gapwise grid distribution

Turbulence Model	wall function	reattachment length (mm)	average y+	pressure drop (MPa)
k-ε	standard	37.2	125	0.82
k-ε	nonequilibrium	39.1	130	0.79
RNG k-ε	nonequilibrium	40.7	129	0.79

A second mesh generated includes the inlet plenum as well as the channel and is comprised of 186 cells along the axial direction, 38 cells across half the span, and 3 cells across half the gap. The mesh in the gap direction has a linear distribution weighted toward the walls. This shift in the gapwise mesh was to improve the applicability of the wall functions. Using this mesh, three cases were executed using k-ε, RNG k-ε, and RSM turbulence models all with nonequilibrium wall functions. All three cases were brought to

convergence and then analyzed. There were no graphically obvious differences in the velocity, pressure, or turbulence fields, however, the flow field and the individual stresses for the RSM case were plotted. Some observations regarding these cases are summarized in Table 3.

Table 3. CFD cases using wall functions as near-wall treatment on a mesh with gapwise distribution weighted toward the wall

Turbulence Model	discretization	reattachment length (mm)	average y+	pressure drop (MPa)
k-ε	first-order	37.5	84	0.82
RNG k-ε	first-order	42	86	0.82
RSM	first-order	40	87	0.84

If one looks carefully at the pathlines in Fig. 56, a small recirculation region can be seen along the side of the blockage. The earlier solution depicted in Fig. 51 with a coarser grid and standard k-ε turbulence model failed to capture this small recirculation zone. One point of interest when looking at these nonuniform mesh cases is the relative magnitude of the individual Reynolds stresses as compared to the isotropic turbulence treatment used in the k-ε and RNG k-ε models. From Figs. 57 and 58, it appears that the VV and WW components are comparable. The UU component in Fig. 59, however, is about twice the magnitude of the either components.

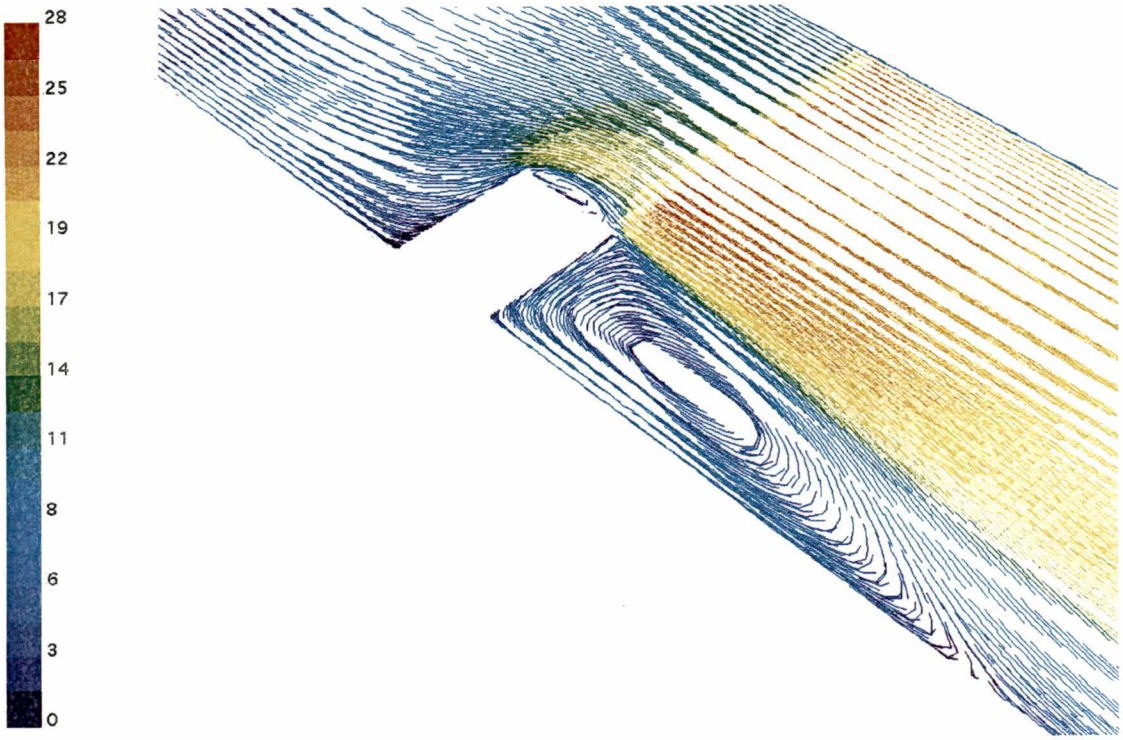


Figure 56. Path lines colored by velocity magnitude for RSM case (m/s)

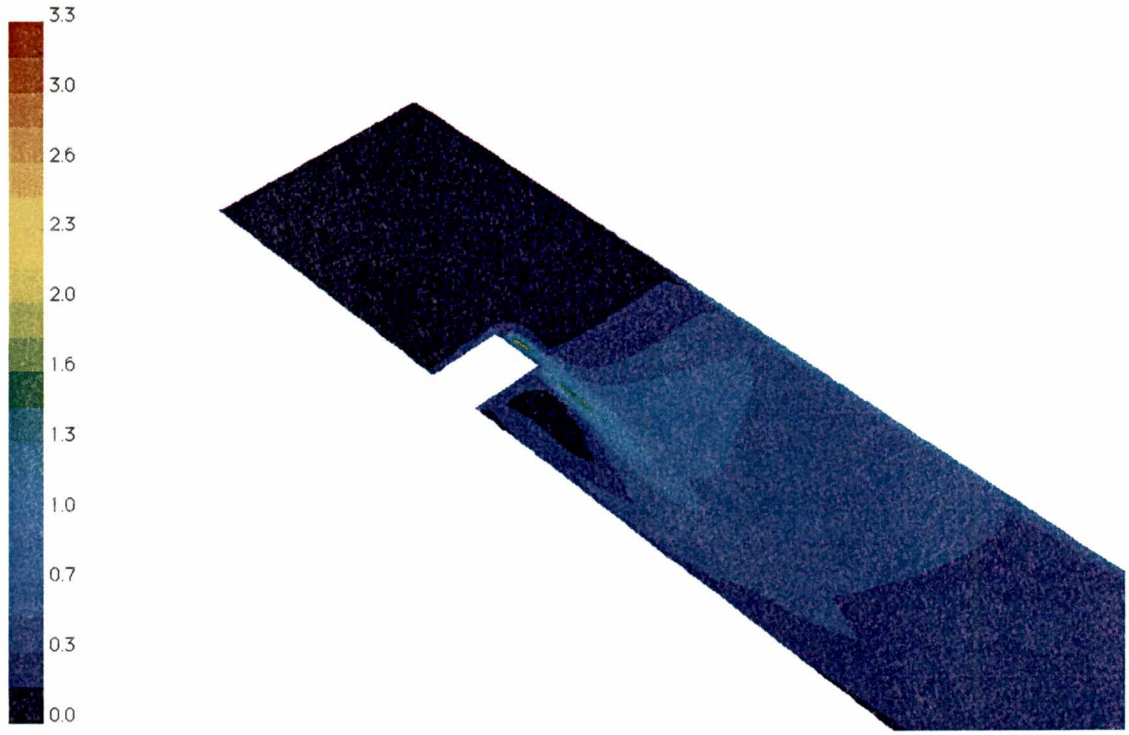


Figure 57. Contours of VV Reynolds stress for RSM case (m^2/s^2)

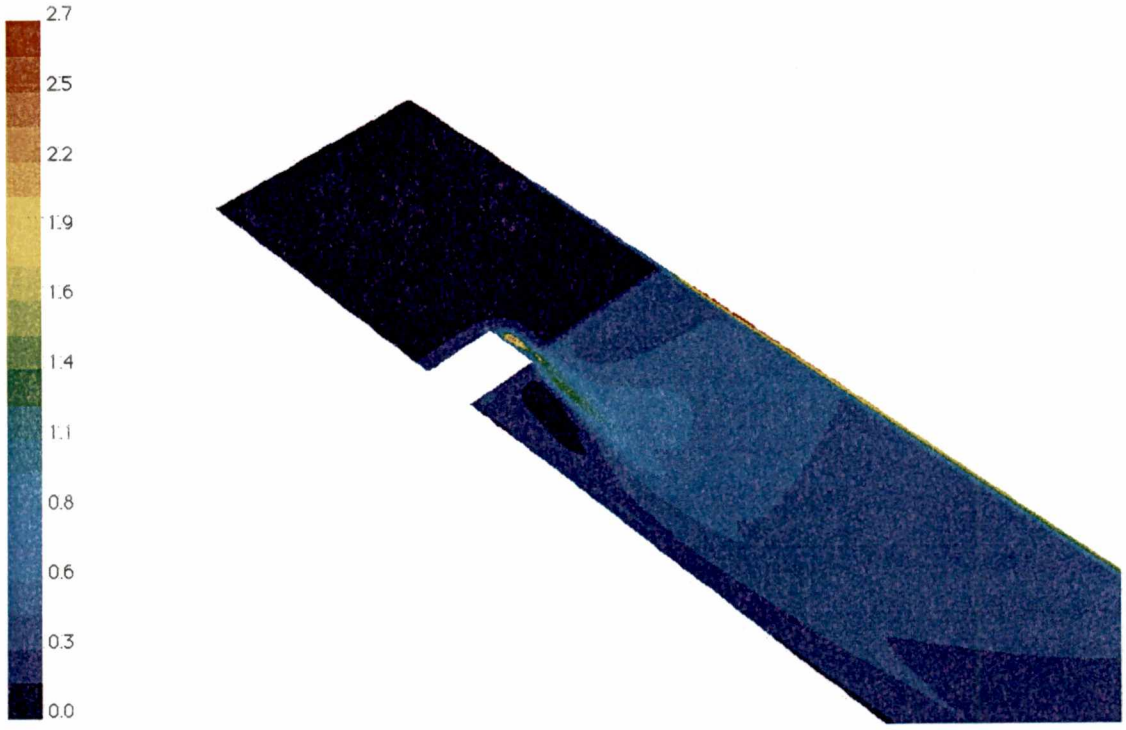


Figure 58. Contours of WW Reynolds stress for RSM case (m^2/s^2)

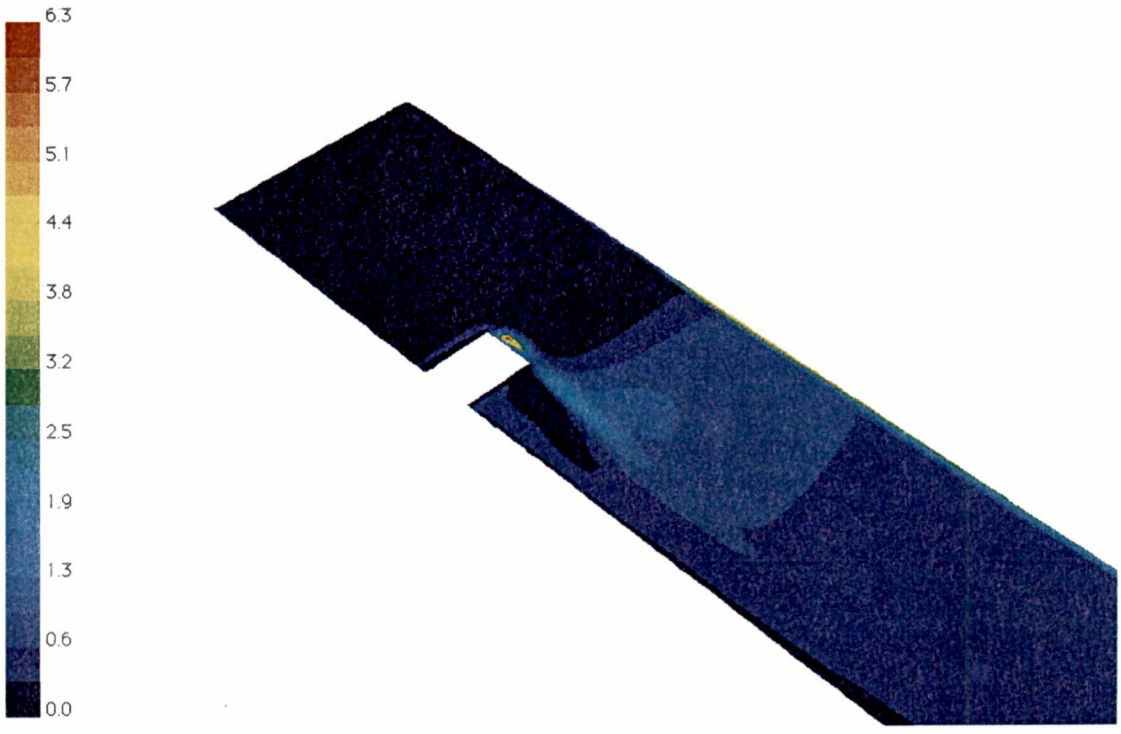


Figure 59. Contours of UU Reynolds stress for RSM case (m^2/s^2)

6.2 BOUNDARY LAYER RESOLUTION

The first mesh generated for the two layer zonal model includes the inlet plenum as well as a shortened channel and is comprised of 140 cells along the axial direction, 52 cells across half the span, and 9 cells across half the gap. The mesh was shortened in the axial dimension so as to allow for refinement in the gapwise dimension. The mesh in the gap direction has a linear distribution weighted toward the wall.

Using this mesh, a case was executed using the k-ε model with nonequilibrium wall functions. Reattachment was predicted to occur at 39.1 mm

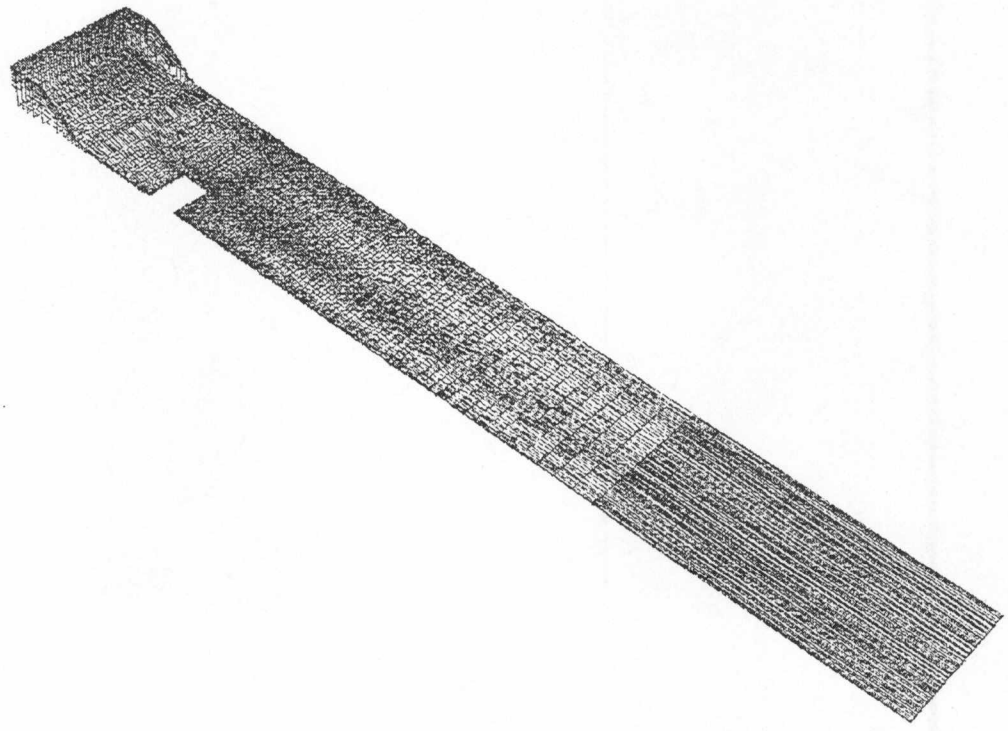


Figure 60. Inlet plenum and shortened channel mesh

downstream of the blockage. The pressure drop for this shortened channel was predicted to be 0.54 MPa.

Upon close observation of the contours of turbulent kinetic energy in Fig. 61 and a comparison to the corresponding contours in Fig. 54, it appears that the resulting turbulence field is quite different. This is due to the inadequacy of the near-wall grid that governs which turbulence equations are being used in the two-layer zonal model. In the two-layer zonal model, the entire domain is subdivided into a viscosity-affected region and a fully-turbulent region. The model uses the wall-distance based turbulent Reynolds number (Re_y) to establish the two regions. Ideally one must have at least 10 cells within the

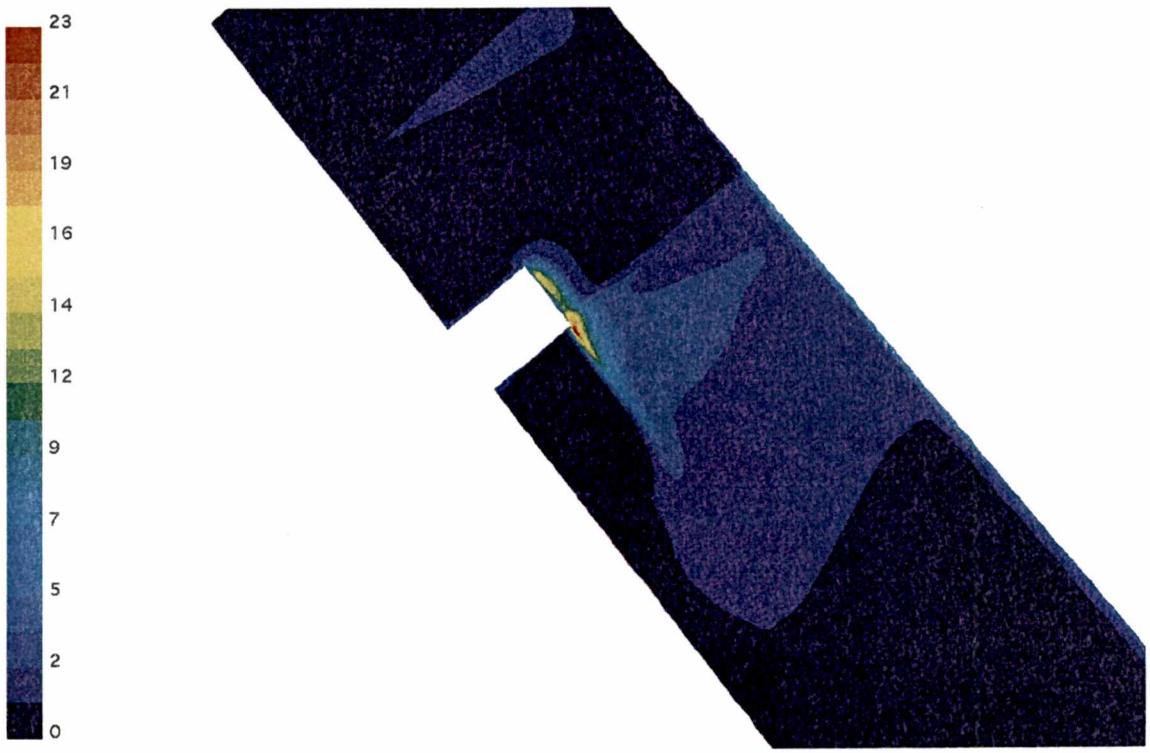


Figure 61. Contours of turbulent kinetic energy for 9 gap cells (m^2/s^2)

viscosity-affected near-wall region (Re_y < 200) to adequately resolve the boundary layer. Another parameter to check is the surface y^+ which should be less than 5. As can be seen in Fig. 62, with this mesh only three cells lie within this region. The average surface y^+ was 9.5.

This mesh was further refined in the gap-wise dimension to 14 cells and re-executed using the same solver configuration. Reattachment was predicted to occur at 41.5 mm downstream of the blockage. The pressure drop for this shortened channel was predicted to be 0.55 MPa. The resulting turbulence field in Fig. 63 still appears quite strange. As can be seen in Fig. 64, with this

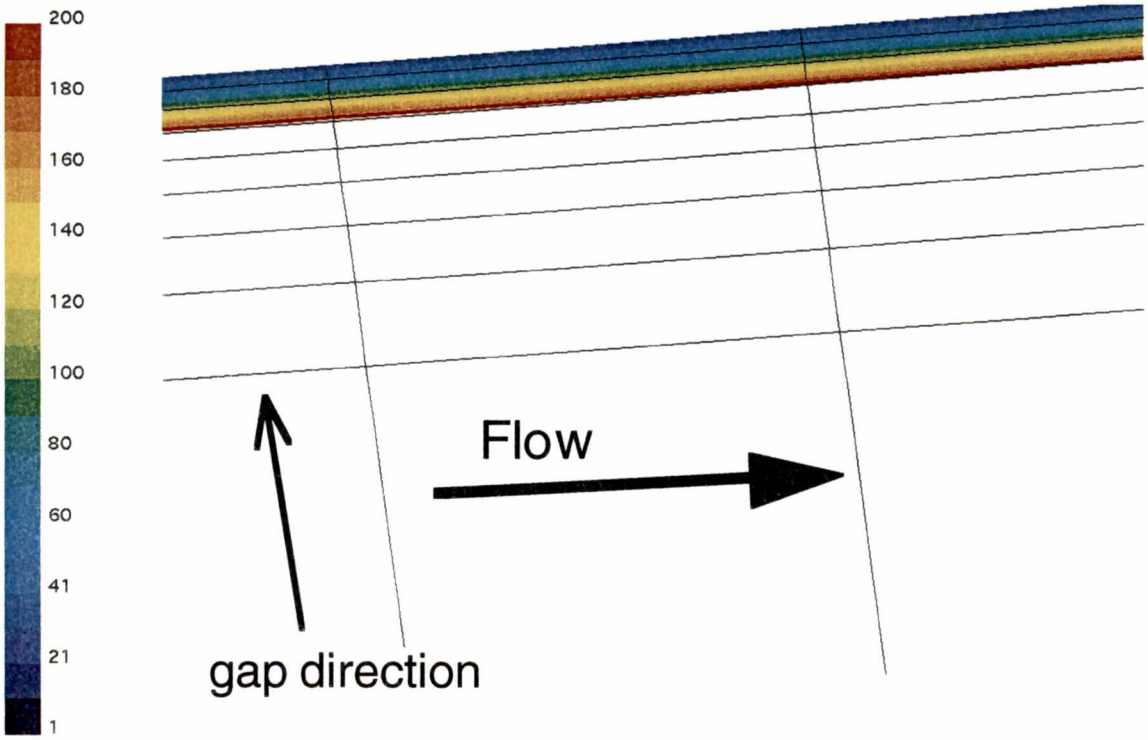


Figure 62. Contours of turbulent Reynolds number for 9 gap cells (Re_y)

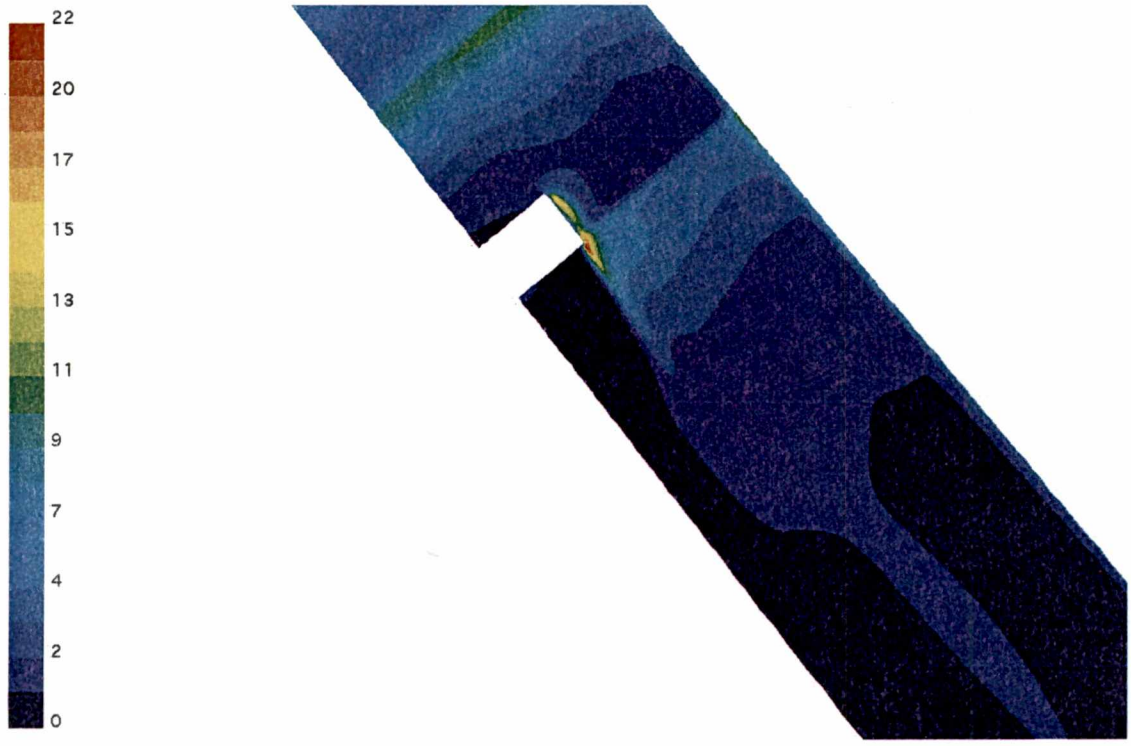


Figure 63. Contours of turbulent kinetic energy for 14 gap cells (m^2/s^2)

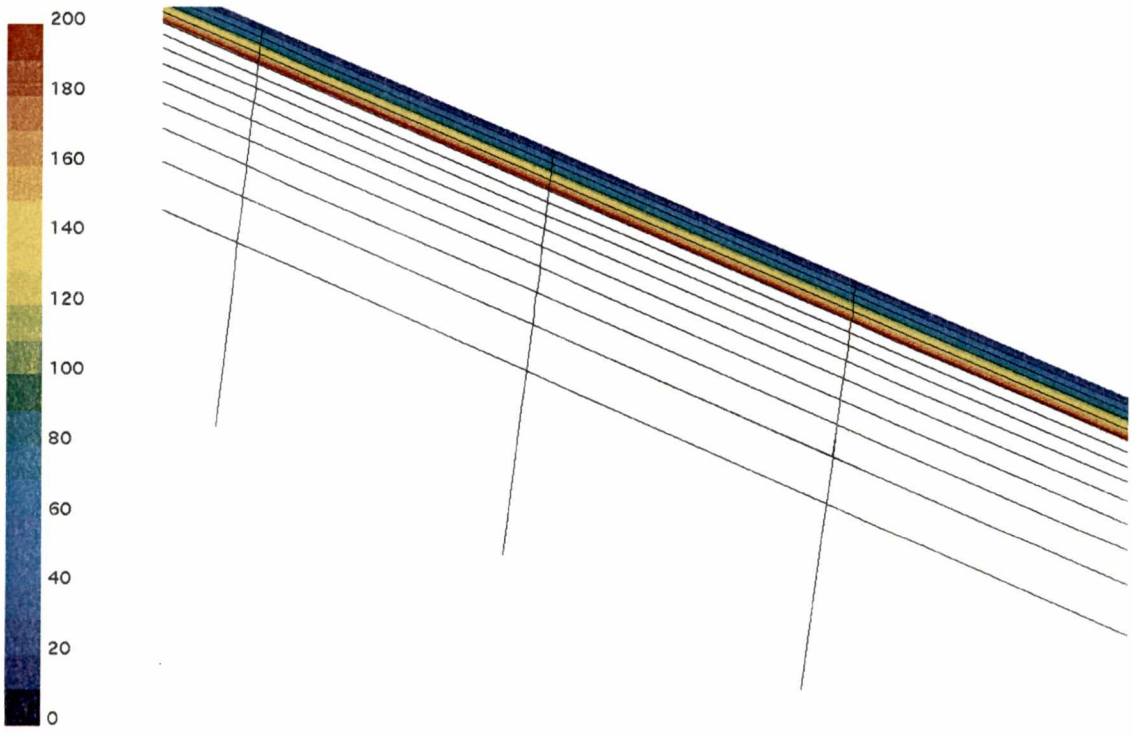


Figure 64. Contours of turbulent Reynolds number for 14 gap cells (Re_y)

refined mesh only five cells lie within the viscosity-affected region. The average surface y^+ was 7.2.

Before refining the mesh again, the inlet plenum was removed to allow for a more efficient use of the computational grid. The velocity and turbulence profiles from the channel entrance were saved and patched into the new shorter grid with the gap-wise dimension refined to 17 cells. This new refined mesh was executed using the same solver configuration. Reattachment was predicted to occur at 30.7 mm downstream of the blockage. The pressure drop for the channel only was predicted to be 0.21 MPa. The resulting turbulence field in Fig. 65 appears comparable to that in Fig. 54. With this refined mesh, 13 cells lie within the viscosity-affected region (Fig. 66), and the average surface y^+ is 4.1.

Once an acceptable turbulence field was obtained and the grid was sufficiently refined, this mesh was re-executed using RNG k-ε for both a first and second-order discretization. For the first-order case, reattachment was predicted to occur at 32.2 mm downstream of the blockage. The pressure drop for the channel only was predicted to be 0.15 MPa. For the second-order case, reattachment was predicted to occur at 36.2 mm downstream of the blockage. The pressure drop for the channel only was predicted to be 0.15 MPa. A summary for the boundary layer resolution cases can be found in Table 4.

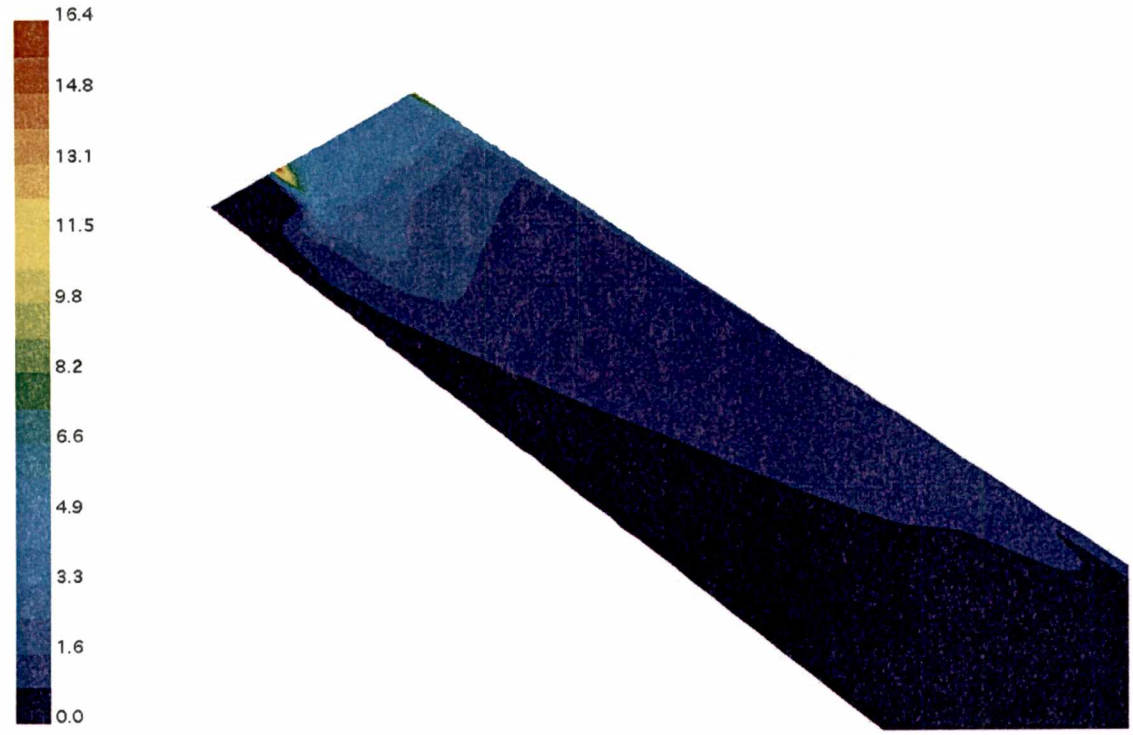


Figure 65. Contours of turbulent kinetic energy for 17 gap cells (m^2/s^2)

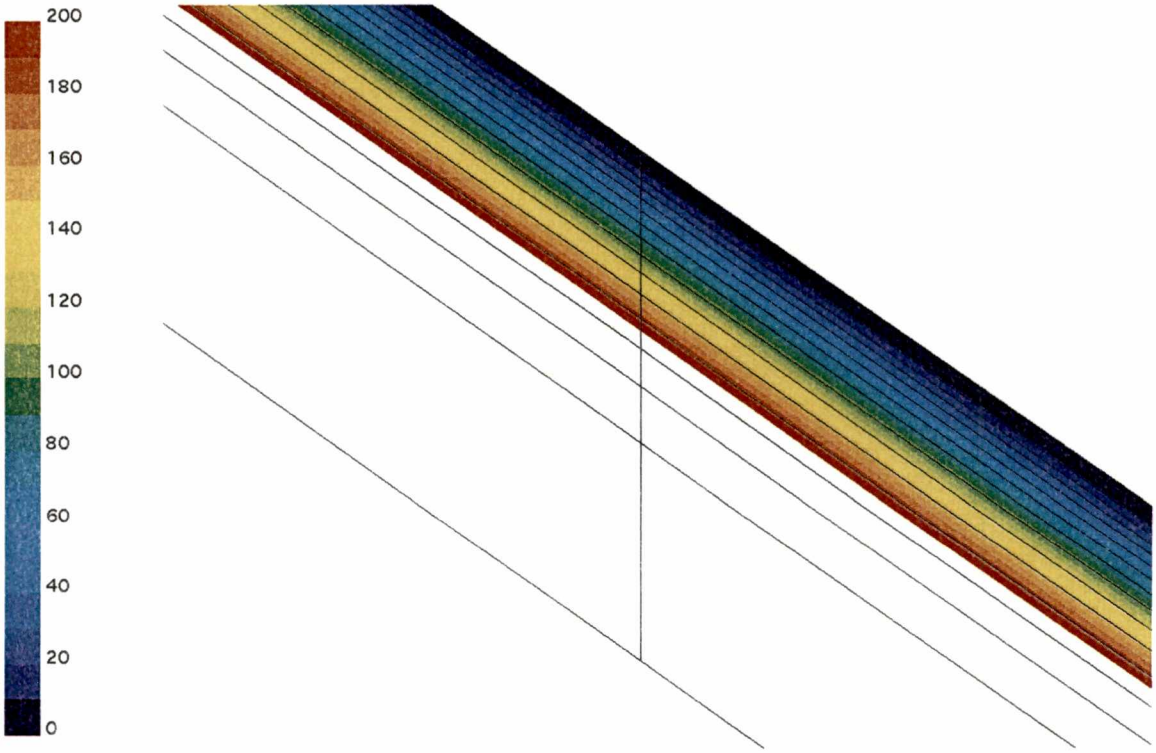


Figure 66. Contours of turbulent Reynolds number for 17 gap cells (Re_y)

Table 4. CFD cases using boundary layer resolution as near-wall treatment

Turbulence Model	gapwise grid	discretization	reattachment length (mm)	average y+
k-ε	9	first-order	39.1	9.5
k-ε	14	first-order	41.5	7.2
k-ε	17	first-order	30.7	4.1
RNG k-ε	17	first-order	32.2	4.0
RNG k-ε	17	second-order	36.2	4.0

6.3 LDV COMPARISONS

Once an accurate solution had been obtained for both the wall function and boundary layer resolution approaches, three of the cases were then compared to the actual LDV measurements for the same blockage configuration. The RSM case from the wall function approach was selected as well as the first-order k-ε and the second-order RNG k-ε from the boundary layer resolution approach. While the RSM and RNG k-ε cases were selected due to their accuracy, the first-order k-ε case was selected because its solution yielded the best agreement with the LDV measured velocity profiles and reattachment length.

The most highly accurate solution utilizing the wall function approach for the near wall treatment was the RSM case. Unlike standard k-ε and RNG k-ε turbulence models, which assume the turbulence is isotropic, RSM involves

calculation of the individual Reynolds stresses. The predicted reattachment length was 40 mm, as compared to 31 mm determined from a curve fit of the minimum velocities at each measurement location. The axial velocity profiles for the first and last measurement windows can be found in Fig. 67. The error bars on the LDV data for the first measurement location at 10.8 d_h are the LDV measured standard deviation. The magnitudes of these error bars are consistent with turbulent intensity measured at the same location. As can be seen in Fig. 67, the standard deviations are larger in the recirculation region and can be partially attributed to inherent flow unsteadiness and the possibility of localized vortex shedding. Although the predicted reattachment length is 29% longer than that determined from the LDV data, it is important to note that the experimental reattachment length was not measured directly and is highly dependent upon the magnitude of the negative velocity at the first measurement location. As can be seen by the error bars, this region is highly turbulent and thus prone to large velocity fluctuations. A single comparison of the reattachment lengths (Tables 3 and 4) without looking at the entire flow field would lead one to believe that the CFD calculations and LDV data would not compare well. This, however, is not true as evidenced by the fair agreement seen in Fig. 67. The velocity profile at the fifth measurement window is also in good agreement with the LDV data, the primary difference being the more pronounced velocity minimum in the CFD calculations. This distinct velocity minimum is consistent with a conservative estimate of the flow recovery.

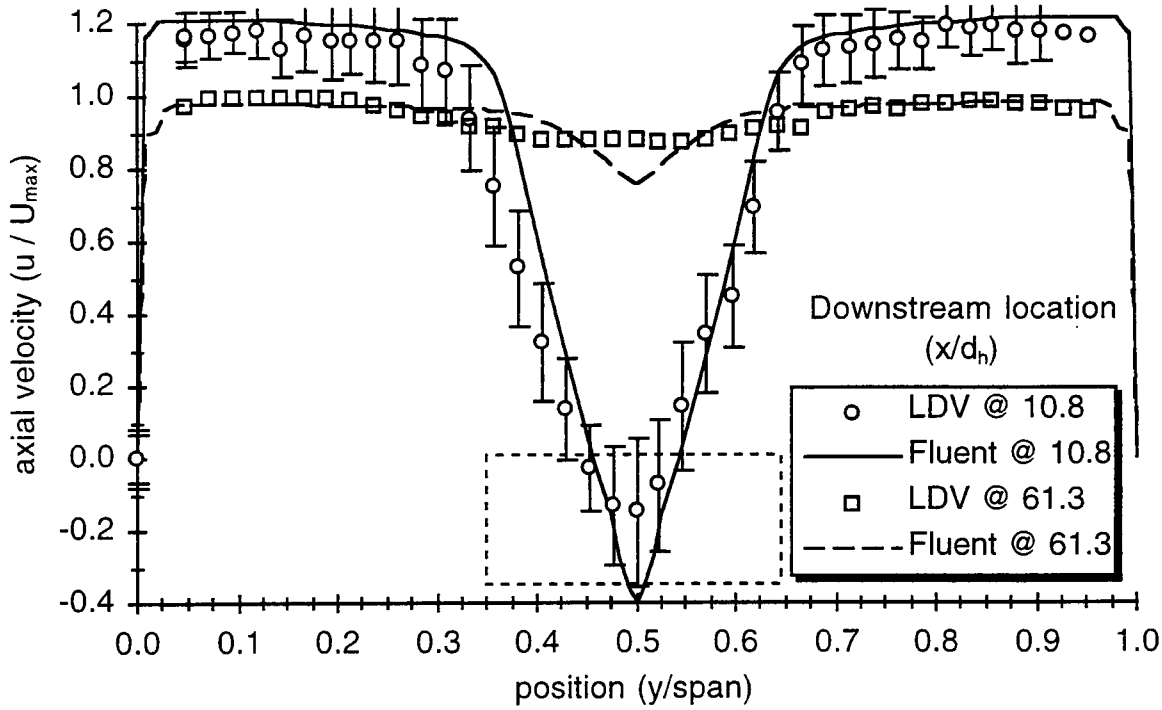


Figure 67. Comparison of measured axial velocity profiles to CFD calculations using the RSM turbulence model

The spanwise velocity profiles in Fig. 68 also show surprising agreement. The spanwise velocity measurements at 10.8 d_h have a distinct profile of positive and negative velocities consistent with a recirculation region. The agreement between the measured and calculated values is excellent with the primary disagreement being the asymmetry of the LDV data. The error bars, as before, reflect a high turbulent intensity in the recirculation region. By the fifth measurement location, the velocity profiles for both LDV and CFD are essentially flat.

Boundary layer resolution was another approach used for the near wall treatment for a series of cases. In this approach, wall functions were

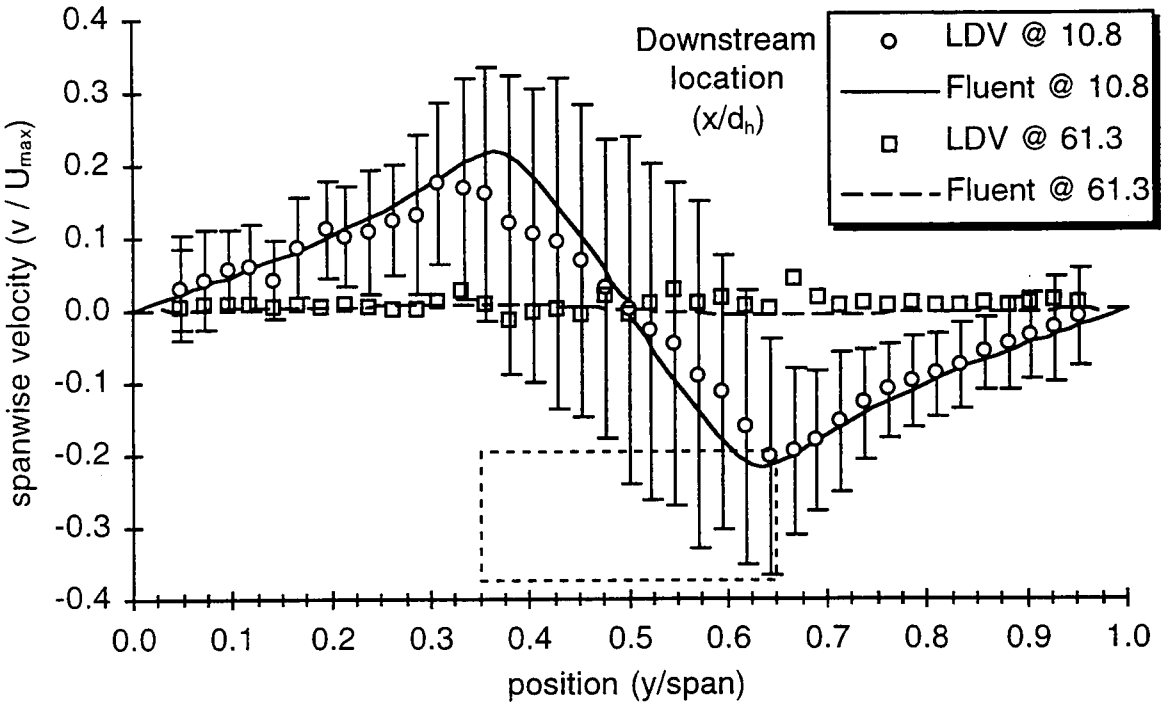


Figure 68. Comparison of measured spanwise velocity profiles to CFD calculations using the RSM turbulence model

abandoned and the near-wall region was resolved all the way to the wall. The following two cases utilize this approach on the finest grid but with different turbulence models.

One of the cases utilizing the boundary layer resolution for the near wall treatment was the standard k-ε with first-order discretization. The primary reason for selecting this case for LDV comparison was its predicted reattachment length of 30.7 mm. This compares very well with the 31.3 mm determined from a curve fit of the minimum velocities at each measurement location. The axial velocity profiles for the first and last measurement window can be found in Fig. 69. Unlike the previous case, the CFD calculated velocity

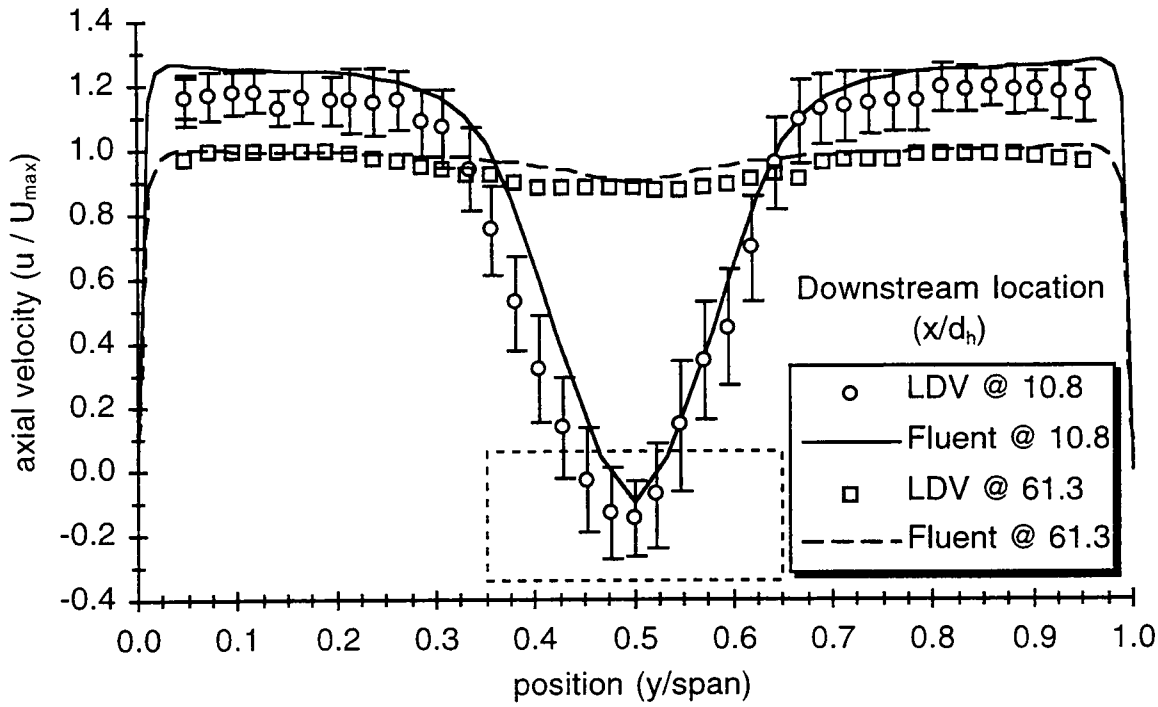


Figure 69. Comparison of measured axial velocity profiles to CFD calculations using the k-ε turbulence model with boundary layer resolution

profile for the first measurement location at 10.8 d_h reflects a slightly higher velocity than measured by the LDV. This is consistent with the shorter predicted reattachment length. The velocity profile at the fifth measurement window is also in good agreement with the LDV data. Unlike the previous wall function case, the velocity minimum in this case is far less pronounced.

The agreement between the measured and calculated values in Fig. 70 is fair. The CFD predicted peak spanwise velocities in the recirculation region are higher and the peaks are located nearer the center. By the fifth measurement location, the velocity profiles for both LDV and CFD are

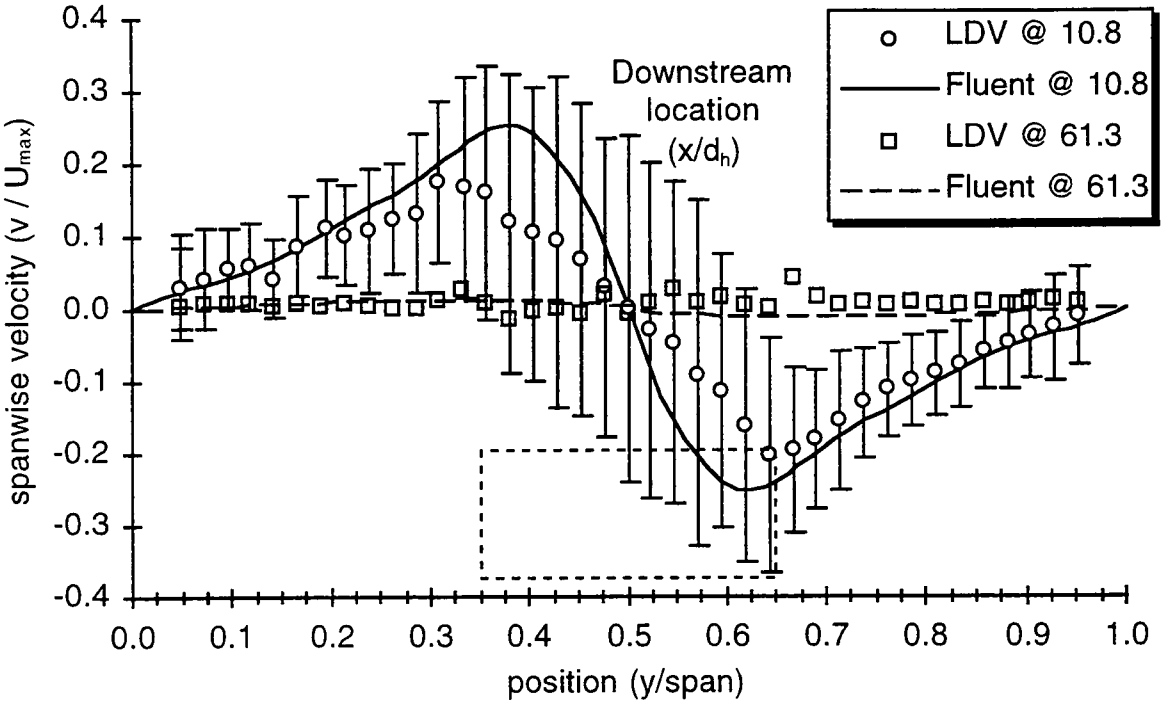


Figure 70. Comparison of measured spanwise velocity profiles to CFD calculations using the k-ε turbulence model with boundary layer resolution

essentially flat. Although this CFD case resulted in the closest predicted reattachment length, it is important to note that this length, as well as the axial velocity profiles, are non-conservative.

Another case utilizing the boundary layer resolution for the near wall treatment was the RNG k-ε with second-order discretization. The primary reason for selecting this case for LDV comparison was its accuracy. The predicted reattachment length was 36 mm as compared to 31 mm determined from a curve fit of the minimum velocities at each measurement location. The axial velocity profiles for the first and last measurement window can be found in

Fig. 71. Much like the RSM case, the CFD-calculated velocity profile for the first measurement location at 10.8 d_h reflects a slightly lower velocity than measured by the LDV. The velocity profile at the fifth measurement window is also in good agreement with the LDV data, the primary difference being the more pronounced velocity minimum in the CFD calculations. This velocity minimum is more distinct than in the standard k-ε case, but not as pronounced as in the RSM case.

The agreement between the measured and calculated values in Fig. 72 is fair. The CFD predicted peak spanwise velocities in the recirculation region

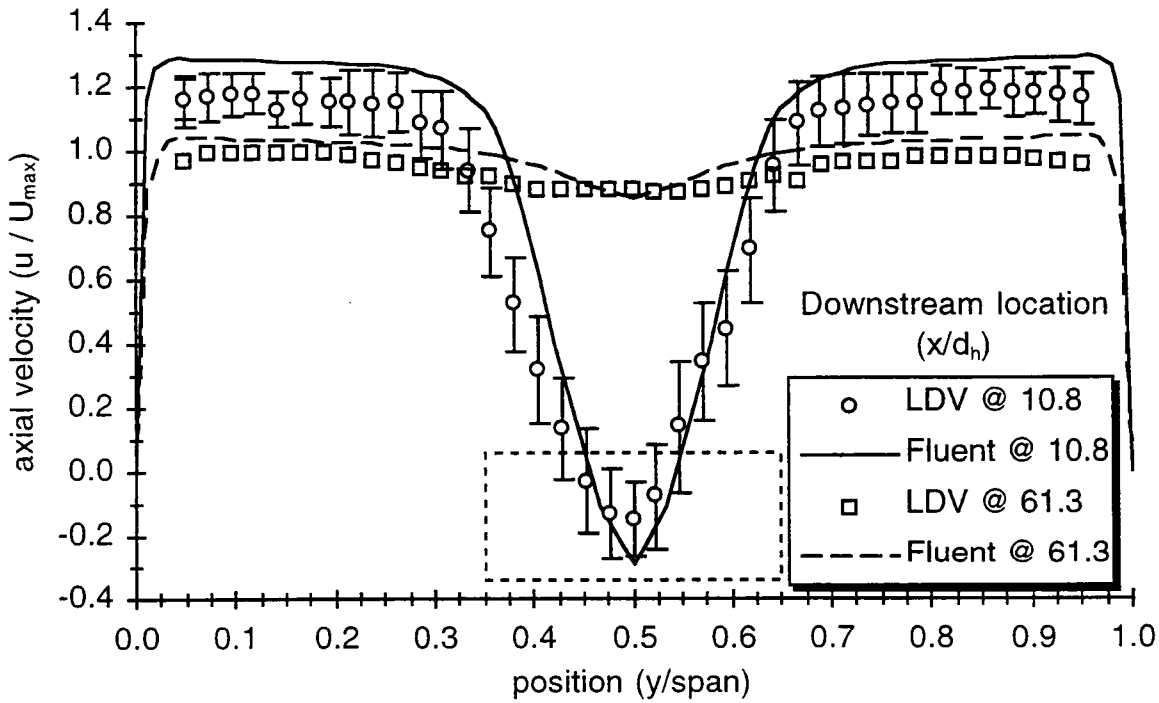


Figure 71. Comparison of measured axial velocity profiles to CFD calculations using the RNG k-ε turbulence model with boundary layer resolution

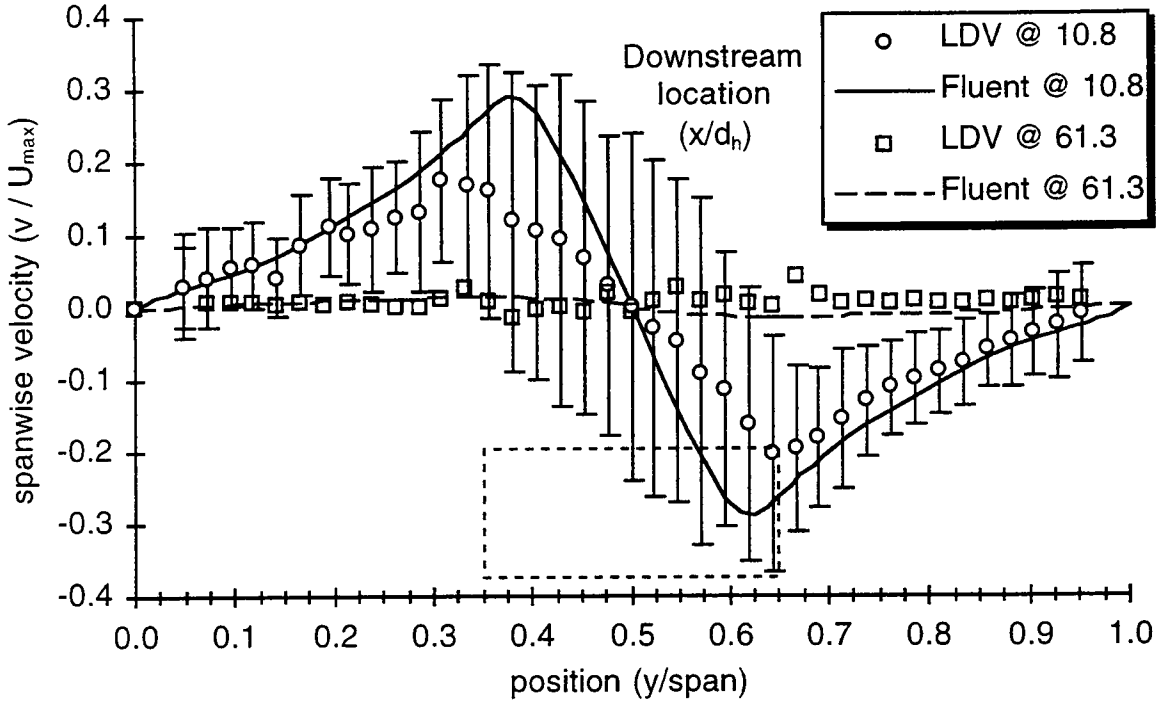


Figure 72. Comparison of measured spanwise velocity profiles to CFD calculations using the RNG k-ε turbulence model with boundary layer resolution

are higher and the peaks are located nearer the center. These peaks also appear sharper than those for the standard k-ε case. By the fifth measurement location, the velocity profiles for both LDV and CFD are essentially flat.

In summary, all of the selected CFD cases compare well to the LDV measured flow fields. While the first-order k-ε case with boundary layer resolution gave the best agreement for the axial velocity profiles and reattachment, the solution was non-conservative. While the RSM case with wall functions gave the relatively poorest agreement for the axial velocity, the solution had excellent agreement for the spanwise velocity profiles. The RNG k-

ε case with boundary layer resolution provided the best mix of accuracy and conservatism. This model, however, was the most computational expensive due to the massive grid required to adequately refine the boundary layer. Although the RSM case with wall functions gave the poorest agreement for the axial velocity, its predictions were conservative and required the least computationally intensive grid. For this reason, the RSM case with wall functions would be recommended for use in these applications.

7. CONCLUSIONS

One of the initial areas of inquiry for this thesis was the question of whether or not shape would have an impact on the fluid flow behavior downstream of the blockage. From this work, it is evident that shape indeed has an impact not only on the resulting average velocity, but also the reattachment length. It was found that rounded and streamlined blockages resulted in shorter reattachment lengths as well as higher average velocities. The triangular and trapezoidal blockages were then reversed so that they were in a diverging arrangement. A comparison of the resulting average velocities and reattachment lengths revealed that the impact of the diverging orientation was apparently greater than the impact of the converging orientation. Another area of inquiry required the study of the effect of position on downstream fluid flow behavior. Starting with a centrally located 15% blockage, several off-center positions were examined. Although it is well established that edge blockages result in longer wakes than do their centrally positioned equivalents, velocity profiles downstream of a blockage positioned 1.27 mm from the wall show a slightly longer wake than compared to the edge position. A similar trend was found by examining velocity profiles downstream of a dual 15% blockage. Prior to this thesis, it was assumed that replacing a centrally positioned 30% blockage with a pair of 15% blockages positioned some distance apart would result in a shorter wake or wakes. This was found to be true only when the blockages were placed some critical distance apart. For blockage

configurations in which the separation distance is less than some critical distance, the replacement of a 30% with two 15% blockages actually lengthens the resulting wake. For a pair of 15% blockages positioned 5 mm apart, the resulting wake was actually longer than that measured for a 40% blockage. CFD models of a 30% center blockage were constructed and executed. The effects of grid refinement, turbulence models, and near-wall treatment were all evaluated. Although there were noticeable variations in the solution, all of the cases resulted in good agreement with the LDV measured axial and spanwise velocity profiles.

It is important to note that for the blockage configurations tested, these LDV measurements were made for the same pressure drop as opposed to the same flow. This was necessary in order to adequately determine the effect of blockage size, shape, and position on the flow in a partially blocked channel in a reactor with a nearly infinite by-pass ratio. For this reason, the measurements and flow observations made are highly relevant to plate fueled reactor safety. The correlations for average mid-gap velocity and reattachment length can be useful in the Probabilistic Risk Assessment (PRA) and Safety Analysis Reports (SAR) for such reactors. Such information could also be helpful in the design of future reactors.

REFERENCES

REFERENCES

Bertini, H. W., *Descriptions of Selected Accidents that Have Occurred at Nuclear Reactor Facilities*, ORNL/NSIC-176, Martin Marietta Energy Systems, Inc., Oak Ridge National Laboratory, Oak Ridge, TN, April 1980.

Burden, Richard L., Faires, J. Douglas, *Numerical Analysis*, 5th ed., PWS Publishing Company, Boston, 1993

Cur, N., "Local Turbulent Heat Transfer Coefficients in a Symmetrically or Asymmetrically Heated Flat Rectangular Duct with Either Uniform or Nonuniform Inlet Velocity," Ph.D. thesis, Department of Mechanical Engineering, University of Minnesota, Minneapolis, MN, 1982.

Fluent, Inc., *Introduction to the Renormalized Group Method and Turbulence Modeling*, TM-107, Lebanon, NH, January, 1993.

Fluent, Inc., *FLUENT/UNS User's Guide*, Release 4.0, Lebanon, NH, April, 1996.

Fontana, M. H., Kress, T. S., Parsly, T. S., Thomas, D. G., and Wantland, J. L., *Effect of Partial Blockages in Simulated LMFBR Fuel Assemblies*, ORNL-TM-4324, Oak Ridge National Laboratory, Oak Ridge, TN, December 1973.

Kirsch, D. and Schleisiek, K., "Flow and Temperature Distributions Around Local Coolant Blockages in Sodium-Cooled Fuel Subassemblies," *Progress in Heat and Mass Transfer*, pp. 239-249, V. 7, 1973.

Koram, K. K. and Sparrow, E. M., "Turbulent Heat Transfer Downstream of an Unsymmetric Blockage in a Tube," *Journal of Heat Transfer*, pp. 588-594, V. 100, November 1978.

Martinuzzi, R. and Tropea, C., "The Flow Around Surface-Mounted, Prismatic Obstacles Placed in a Fully Developed Channel Flow," *Journal of Fluids Engineering*, pp. 85-92, V. 115, March 1993.

Meyer, J. E., Kwak, S. M., and Shubert, T. D., *Narrow Channel Turbulence Modeling Project Final Report*, MITNE-299, Massachusetts Institute of Technology, March 1992.

Patrick, W. P., "Error Analysis for Benchmark Fluid Dynamics Experiments, Part I: Error Analysis Methodology and the Quantification of Laser

Velocimeter Error Sources, R85-151772, United Technologies Research Center, East Hartford, CT, 1985.

Popiel, C. O. and Turner, J. T., "Visualization of High Blockage Flow Behind a Flat Plate in a Rectangular Channel," *Journal of Fluids Engineering*, pp. 143-146, V. 113, March 1991.

Prakash, C. and Zerkle, R., "Prediction of Turbulent Flow and Heat Transfer in a Ribbed Rectangular Duct With and Without Rotation," *Journal of Turbomachinery*, pp. 255-264, V. 117, April 1995.

Roeller, P. T. and Webb, B. W., "A Composite Correlation for Heat Transfer from Isolated Two- and Three-dimensional Protrusions in Channels," *International Journal of Heat and Mass Transfer*, pp. 987-990, V. 35, 1992.

Sparrow, E. M. and Wachtler, K. P., "Transfer Coefficients on the Surfaces of a Transverse Plate Situated in a Duct Flow," *International Journal of Heat and Mass Transfer*, pp.761-767, V. 21, 1978.

Sparrow, E. M., Koram, K. K., and Charmchi, M., "Heat Transfer and Pressure Drop Characteristics Induced by a Slat Blockage in a Circular Tube," *Journal of Heat Transfer*, pp. 64-70, V. 102, February 1980.

Sparrow, E. M., Molki, M., and Chastain, S. R., "Turbulent Heat Transfer Coefficients and Fluid Flow Patterns on the Faces of a Centrally Positioned Blockage in a Duct," *International Journal of Heat and Mass Transfer*, pp.507-519, V. 24, 1981.

Sparrow, E. M. and Cur, N., "Maldistributed Inlet Flow Effects on Turbulent Heat Transfer and Pressure Drop in a Flat Rectangular Duct," *Journal of Heat Transfer*, pp. 527-535, V. 105, August 1983.

Stovall, T. K., Crabtree, J. A., Felde, D. K., and Park, J. E., *Flow Blockage Analysis of the Advanced Neutron Source Reactor*, ORNL/TM-6860, Oak Ridge National Laboratory, Oak Ridge, TN, August 1995.

Thompson, T. J. and Beckenley, J. G., eds., The Technology of Nuclear Reactor Safety, MIT Press, Cambridge, MA, 1964.

TSI, Inc., Flow Information Display (FIND) Software, Version 4.0, St. Paul, MN, March 1993.

White, Frank M., *Fluid Machanics*, 2nd ed., McGraw Hill, New York, 1986.

VITA

Allen Crabtree was born in Huntsville, Alabama on January 24, 1970. He attended schools in the public system of Lincoln County, Tennessee, where he graduated from Lincoln County High School in June of 1988. In the fall of 1988, he enrolled at The University of Tennessee. The following summer, he began part-time work in the Engineering Technology Division of the Oak Ridge National Laboratory. In May of 1992 he received the Bachelor of Science degree in Nuclear Engineering, Cum Laude. In August of 1993, he returned to The University of Tennessee to pursue a Master's degree in Engineering Science. The Master's degree was received in August of 1997.

He is presently employed by Lockheed Martin Energy Research at the Oak Ridge National Laboratory as a development staff member in Oak Ridge, Tennessee.